# ULTRASONIC STUDY OF THE CRITICAL BEHAVIOR OF THE ANTIFERROMAGNET $CsNiCl_3$

XUEMEI HAN


CENTRE FOR NFLD. STUDIES
MEMORIAL UNIVERSITY
OF NEWFOUNDLAND

# Ultrasonic Study of the Critical Behavior of the Antiferromagnet $CsNiCl_3$

by

© Xuemei Han
M.Sc. (Jilin University, Changchun, China) 2004
B.Sc. (Jilin University, Changchun, China) 2001

A thesis submitted to the
School of Graduate Studies
in partial fulfillment of the
requirements for the degree of
Doctor of Philosophy.

Department of Physics and Physical Oceanography
Memorial University of Newfoundland

August 24, 2010

St. John's Newfoundland

# Contents

# Abstract

To study the critical behavior of the quasi-one-dimensional antiferromagnet $CsNiCl_3$ near the phase transitions, its elastic constants are investigated using high-resolution ultrasonic velocity measurements as function of temperature and magnetic field applied along the c-direction. The experimental data we present with respect to the longitudinal mode, $\frac{\Delta C_{33}}{C_{33}}$, and the transverse modes, $\frac{\Delta C_{44}}{C_{44}}$ and $\frac{\Delta C_{66}}{C_{66}}$, generate a phase diagram in good agreement with published results by showing two zero-field transitions at $T_{N1} \approx 4.75$ K, $T_{N2} \approx 4.35$ K, and multicritical point at ($T_m \approx 4.50$ K, $H_m \approx 2.29$ T). Moreover, the critical exponent $\beta$ extrapolated from the temperature dependence of $\frac{\Delta C_{66}}{C_{66}}$ shows $XY$ criticality with a constant value $0.35 \pm 0.02$ for $H < H_m$. However, field dependent behavior is observed for $H > H_m$. This is the first experimental evidence that the high-field phase transition associated with the $120^{\circ}$ spin configuration is weakly first-order and experimentally resolves the controversy about the true criticality of the high-field phase boundary. This result is also strengthened by the step-like variation demonstrated by temperature dependence of $\frac{\Delta C_{44}}{C_{44}}$ at fields higher than the multicritical field ($H_m \approx 2.29$ T) and hysteresis phenomena observed in field dependence of $\frac{\Delta C_{44}}{C_{44}}$ at $T = 5.00$ K. Numerical predictions are made based on the Landau model. The elastic constants of $CsNiCl_3$ in different phases are calculated using the total free energy, which is derived according to the Landau free-energy, the elastic energy, and the magnetoelastic coupling terms

invariant under the symmetry operation of the hexagonal group $P6_3/mmc$. Meanwhile, the non-mean-field order parameter and quadratic-quadratic (q-q) couplings are considered to optimize the numerical prediction and achieve a good reproduction of the experimental data. Furthermore, by studying the numerical predicted elastic constants and strains, a decrease of the spin structure symmetry, from hexagonal to orthorhombic, is proved in the elliptical phase.

# Acknowledgements

I owe my sincere gratitude to Dr. Guy Quirion, my supervisor, for his constant guidance from initial to final level through all the stages of my Ph.D pursuing life. This thesis would not have been possible without his patient encouragement and support.

It is a pleasure to thank Dr. Martin Plumer and Dr. Kris Poduska, the members in my Ph.D committee, for their instructive advice on my research work and daily life.

It is an honor for me to thank Dr. Brad de Young, Dr. Mike Morrow and Dr. Todd Andrews, for their great help and understanding during my thesis writing.

I also would like to thank all the people working around me for building me a pleasant study and work surroundings in physics department.

Finally, I am forever indebted to my parents, my friends and Hui for their understanding, endless patience and encouragement when it was most needed.

# List of Tables

# List of Figures

# Chapter 1

# Introduction

In the past forty years, the class of antiferromagnetic materials with the $ABX_3$ composition have been widely investigated due to their particular magnetic properties[1]. In this chemical formula, A is an alkali metal such as Cs or Rb while B stands for a transition metal such as Ni, Cu, Co, Fe[2] or Mn[3] which acts as magnetic ion, and X represents a halogen element. Published research works[4]–[11] have revealed that the unusual behavior of these quasi-one-dimensional hexagonal antiferromagnetic systems is due to the geometric frustration caused by the triangular lattice structure.

To form the lowest energy state, every magnetic moment attempts to align antiparallel with its nearest neighbors. However, on a triangular lattice, as shown in Fig. 1.1(a), the spin on lattice 3 cannot be simultaneously antiparallel with spins 1 and 2. In order to lift this magnetic frustration, the three magnetic moments adopt a $120^{\circ}$ configuration as shown in Fig. 1.1(b) and Fig. 1.1(c). According to the special $120^{\circ}$ spin structure, left-handed (Fig. 1.1(b)) and right-handed (Fig. 1.1(c)) domains are possible. The existence of these two chiral domains leads to an extra degeneracy which makes these systems particularly interesting.

As commented upon by Roderich Moessner and Arthur P. Ramirez[12], people's

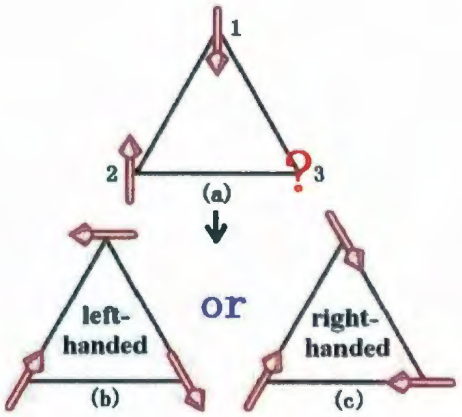


Figure 1.1: Schematic of the two degenerate chiral states of the 120° spin structure.(a) shows that the spin on lattice 3 cannot be arranged antiparallel with spins on lattice 1 and 2. Thus the three spins form a 120° configuration with the possibility of (b) left-handed and (c) right-handed chiral domains.

aroused interest in the instabilities exhibited by frustrated magnets leads to an exploration of both the real nature of different materials and the principles that can explain the observed variety of behaviors. Twenty years ago, based on symmetry arguments and Monte Carlo simulations, Kawamura[13]–[16] claimed that frustrated stacked-triangular antiferromagnets (STA) belong to a new universality class. In Table 1.1, we present a series of critical exponents associated with these new universality classes obtained by Monte Carlo calculations[17] for both $XY$ and Heisenberg STA. Here $n$ refers to the number of dimensions of the model, while $\alpha$, $\beta$, $\gamma$, and $\nu$ are critical exponents with respect to specific heat, order parameter, susceptibility, and correlation length, respectively. Corresponding exponents for the non-frustrated systems[18] are also listed in Table 1.1 for comparison. The difference between both sets of critical exponents illustrates the notion proposed by Kawamura. Thus, based on Kawamura's argument, the occurrence of a second-order transition associated with

| Model | $\alpha$ | $\beta$ | $\gamma$ | $\nu$ |
|---|---|---|---|---|
| ($n = 2$ Chiral) Chiral $XY$ | $0.34_{\pm 0.06}$ | $0.25_{\pm 0.01}$ | $1.13_{\pm 0.05}$ | $0.54_{\pm 0.02}$ |
| ($n = 3$ Chiral) Chiral Heisenberg | $0.24_{\pm 0.08}$ | $0.30_{\pm 0.02}$ | $1.17_{\pm 0.07}$ | $0.59_{\pm 0.02}$ |
| ($n = 1$) Ising | $0.110_{\pm 0.003}$ | $0.325_{\pm 0.001}$ | $1.240_{\pm 0.001}$ | $0.630_{\pm 0.001}$ |
| ($n = 2$) $XY$ | $-0.008_{\pm 0.003}$ | $0.346_{\pm 0.001}$ | $1.316_{\pm 0.001}$ | $0.669_{\pm 0.001}$ |
| ($n = 3$) Heisenberg | $-0.116_{\pm 0.004}$ | $0.365_{\pm 0.001}$ | $1.387_{\pm 0.001}$ | $0.705_{\pm 0.001}$ |

Table 1.1: Critical exponents for various universality classes from Monte Carlo simulations[17].

a 120° spin configuration is expected. However, an alternative theoretical analysis by Azaria et al.[19] appeared around 1990 questioning the existence of the new universality class. According to this analysis, Azaria predicts that the 120° phase transition line should rather be characterized by a weakly first-order type. In the past ten years, further theoretical studies and numerical simulations[20]–[26] have been done to support this statement. Although thermal expansion data on the helimagnet Ho[27] can be employed to support the idea of a weakly first-order transition, no experimental results on systems with the 120° structure have been found to be first-order.

The debate about the true nature of the phase transition of geometric frustrated systems is still ongoing. More recently, Kawamura et al.[16] predicted, based on a scaling theory and renormalization-group analysis, that the phase transition from the paramagnetic phase to the 120° phase is second-order and that the criticality should correspond to the new $n = 2$ chiral universality class. However, results obtained by Delamotte et al.[23] and Ngo et al.[26] show a nonuniversal scaling behavior or a weakly first-order character. Thus, these new numerical works suggest that the 120° phase

transition of the frustrated systems is "most probably of very weak first-order"[23]. Therefore, to solve this controversy, more experimental investigation of the 120° phase transition of $ABX_3$ systems are needed.

Depending on the type of magnetic anisotropy, the magnetic ordering of $ABX_3$ compounds may be classified into two categories, easy-plane anisotropy such as $CsMnBr_3$[28], and easy-axis anisotropy such as $CsNiCl_3$[29]. Schematics of the phase diagrams of these two hexagonal compounds, for a magnetic field oriented along the c-direction, are shown in Fig. 1.2. For the typical easy-plane anisotropy compound $CsMnBr_3$[30],

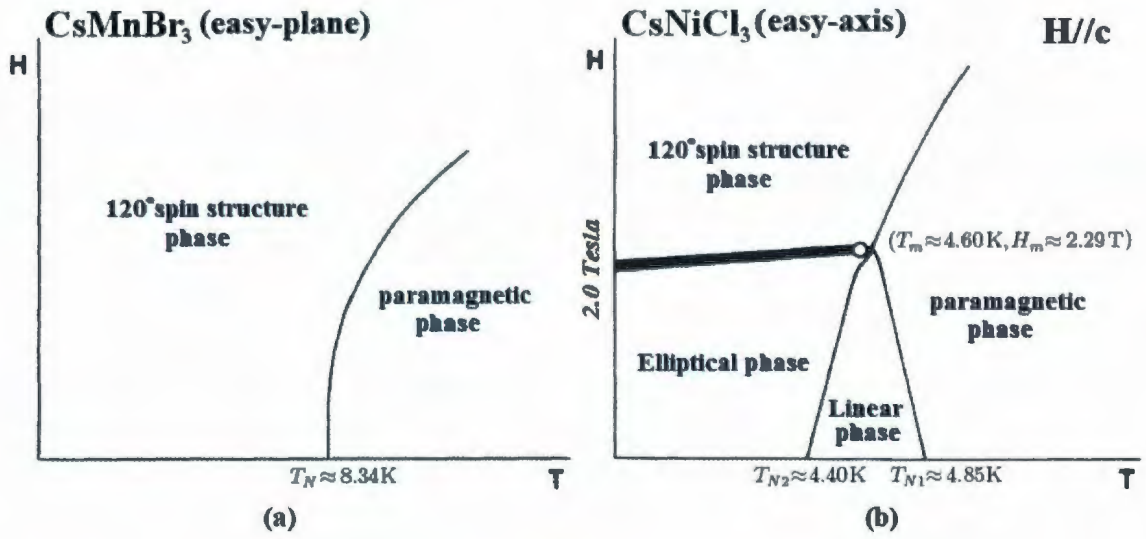


Figure 1.2: Magnetic phase diagram of (a) the easy-plane anisotropy compound $CsMnBr_3$ and (b) the easy-axis anisotropy compound $CsNiCl_3$ for magnetic field applied along the c-direction.

only one ordered phase exists. The 120° phase is separated from paramagnetic phase by a phase boundary as shown in Fig. 1.2(a). For the easy-axis anisotropy system, we take one of the most famous $ABX_3$ compounds $CsNiCl_3$ as an example, which is shown

in Fig. 1.2(b)[16]. Compared with easy-plane type compounds, $CsNiCl_3$ has demonstrated more novel magnetic properties. At zero field, two ordered phases, the linear phase and the elliptical phase are observed below $T_{N1} \approx 4.85$ K and $T_{N2} \approx 4.40$ K, respectively. A field induced spin-flop phase transition from elliptical to the particular $120^{\circ}$ phase is also observed at $H \approx 2.00$ T. A multicritical point, which is of $n = 3$ criticality[16], is observed at ($T_m \approx 4.60$ K, $H_m \approx 2.29$ T). Although both of these systems show a $120^{\circ}$ phase transition, in our work we choose to investigate $CsNiCl_3$ because of its richer phase diagram.

High-resolution ultrasonic velocity measurements have been used to determine the phase diagram of $ABX_3$ compounds[4],[31]–[33]. Other magnetic properties of $CsNiCl_3$, such as the spin-fluctuation under external magnetic field[34] and the crossover behavior near the multicritical point[35] have also bee detected using this method. However, detailed analysis of the observed critical behavior still needs to be developed. Thus, our work is aimed at obtaining sufficient experimental evidence in order to determine the true nature of the phase transition between the paramagnetic phase and the $120^{\circ}$ phase of $CsNiCl_3$. For that purpose, the critical behavior close to phase boundaries under magnetic fields up to 10 Tesla have been investigated. In particular, different acoustic modes, propagating along different crystallographic directions, have been used to investigate the critical behavior of the elastic constants.

The elastic properties of $CsNiCl_3$ are also analyzed using a Landau approach, which adequately describes the variation of the elastic properties in terms of an order parameter. This model takes into account the symmetry changes at the phase transitions and the behavior of thermodynamic potential in the vicinity of the critical points[36]. Based on a Landau model derived by Plumer et al.[11], the nature of the magnetic ordering of $CsNiCl_3$ for different phases are explained. This model is then expanded in order to account for the temperature and magnetic field dependence

of the elastic properties of $CsNiCl_3$. Most coefficients in the model are adjusted by fitting the magnetic phase diagram and thermal expansion data. Non-mean-field temperature dependent order parameters are also employed to optimize the agreement with the experimental data.

The remainder of this thesis is organized as follows. Some fundamental terms of magnetism are briefly introduced in Chapter 2. The crystal structure and low-temperature magnetic properties of $CsNiCl_3$ are presented in Chapter 3. The high-resolution ultrasonic velocity measurements are described in Chapter 4 followed by the introduction of some important concepts for crystalline elasticity in Chapter 5. After presenting the experimental results obtained by ultrasonic measurements in Chapter 6, in Chapters 7, 8, and 9, we derive the model for $CsNiCl_3$ for the case of magnetic field applied along the c-direction based on Landau theory. In Chapter 7 the basic ideas of Landau theory for phase transition are briefly introduced. In Chapter 8 the Landau free-energy for $CsNiCl_3$ is presented for convenience and in Chapter 9 the total free energy, which includes Landau free-energy, elastic energy and magnetoelastic coupling terms is derived. Based on the model, the theoretical elastic constants are calculated in Chapter 10 together with the discussion of the symmetry breaking phenomenon. In Chapter 11, according to the experimental data, the critical behavior of $CsNiCl_3$ near the phase transitions is discussed and the nature of the phase transition between the paramagnetic phase and the $120^{\circ}$ phase is verified. The numerical prediction of the temperature and magnetic field dependence of the relative variation of elastic constants $C_{33}$ and $C_{66}$ are presented in Chapter 12 to show the agreement between our theoretical and experimental results. Chapter 13 contains a summary and conclusions.

# Chapter 2

# Magnetism

In this chapter, some fundamental terms of magnetism, such as magnetic moment, magnetization, and magnetic susceptibility are summarized[37]–[40]. The classification of magnetic material is also presented relative to the temperature dependence of their magnetic susceptibility. Based on this classification, the various types of magnetic ordering and exchange interaction between magnetic moments are briefly described to show the characteristic features of antiferromagnetic systems. Simplest cases of antiferromagnetic spin configuration, due to the geometrical frustration, are also presented. The last part of this chapter is a brief description of the techniques used to measure the magnetic ordering in solids.

## 2.1 Magnetic moment and magnetization

According to the classical electromagnetism, a current $I$ circulating around an infinitesimal area $d\mathbf{A}$ can generate a magnetic moment corresponding to

$$d\boldsymbol{\mu} = I d\mathbf{A}. \tag{2.1}$$

where $d\boldsymbol{\mu}$ is perpendicular to the current loop in a right-hand-rule direction. Under an external magnetic field $\mathbf{H}$, the energy of a magnetic moment is

$$E = -\mu_0 \boldsymbol{\mu} \cdot \mathbf{H} = -\mu_0 \mu H \cos\theta, \tag{2.2}$$

where $\mu_0$ is the permeability of free space and $\theta$ is the angle between $\boldsymbol{\mu}$ and $\mathbf{H}$. According to Eq. 2.2, the lowest energy configuration of the magnetic moment is to align itself with $\mathbf{H}$. In fact, magnetic moment is also associated with the orbital motion of the charges in the current loops. Therefore, rather than pointing towards $\mathbf{H}$, the direction of $\boldsymbol{\mu}$ is precessing around $\mathbf{H}$.

The magnetization, $\mathbf{M}$, is defined as the quantity of magnetic moment per unit volume as

$$\mathbf{M} = \boldsymbol{\mu} \frac{N}{V}, \tag{2.3}$$

where $N$ is the number of the magnetic moment in the sample of volumn $V$. To describe the response of a system as a function of an external magnetic field $\mathbf{H}$, the magnetic induction $\mathbf{B}$ in a solid is defined as

$$\mathbf{B} = \mu_0(\mathbf{H} + \mathbf{M}), \tag{2.4}$$

while in free space there is no magnetization and $\mathbf{B}$ is related to $\mathbf{H}$ as

$$\mathbf{B} = \mu_0 \mathbf{H}. \tag{2.5}$$

## 2.2 Weak magnetism in solids

In magnetic materials, the principal sources of the magnetization are: the electron's intrinsic magnetic moment (spin), the electron's orbital angular momentum about the nucleus, and the change in the orbital moment induced by an external magnetic

field. The paramagnetic contribution to the magnetization comes from the first two sources, while the diamagnetic contribution originates from the third effect.

The relation between the magnetization **M** and the external magnetic field **H** can be written as

$$\mathbf{M} = \chi \mathbf{H}, \tag{2.6}$$

where $\chi$ is defined as the magnetic susceptibility. Noticing the definition of magnetization given by Eq. 2.3, $\chi$ is dimensionless, representing the the magnetic moments induced by **H** per unit volume. The magnetic susceptibility can also be described in terms of molar susceptibility, $\chi_{mol}$, and mass susceptibility $\chi_{mass}$, where

$$\chi_{mol} = \chi V_{mol}; \tag{2.7a}$$

$$\chi_{mass} = \frac{\chi}{\rho}. \tag{2.7b}$$

$V_{mol}$ is the molar volume while $\rho$ refers to the density. Substances with a negative magnetic susceptibility are called diamagnetic, while that with a positive magnetic susceptibility are called paramagnetic.

### 2.2.1 Diamagnetism

Diamagnetism is the property of substances that have only non magnetic atoms. The magnetization, which is induced by the external field, is very weak and opposite to the applied field. The diamagnetic molar susceptibility is very small, usually of the order of $10^{-5}$ $cm^3 \cdot mol^{-1}$, and independent of both field and temperature.

### 2.2.2 Paramagnetism

The magnetism of paramagnetic substances mainly originates from the permanent magnetic moment of the atoms or ions. Besides this, in metals, conduction electrons

also exhibit paramagnetic behaviors, which is much weaker than that of the atoms or ions.

### Curie paramagnetism

In the absence of an external field, as shown in Fig. 2.1(a), magnetic moments of atoms can orient themselves freely in all directions due to the negligible interactions with each other. When an external field is applied, the average alignment is modified. With the increasing of the field, the number of magnetic moments pointing along the field direction increases. Therefore, a small magnetization is induced in the direction of the external field. As shown in Fig. 2.1(b), the paramagnetic magnetization increases

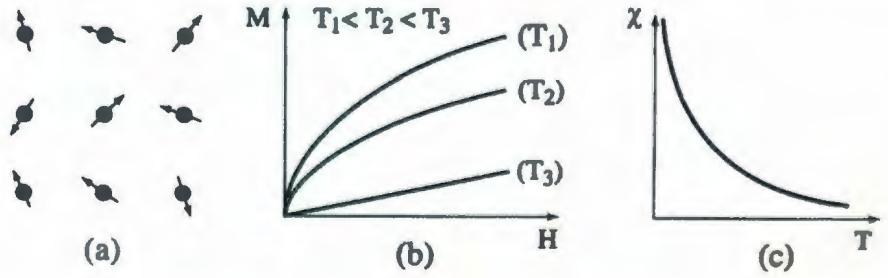


Figure 2.1: Magnetic moment orientation (a), field and temperature dependence of magnetization (b), and temperature dependence of the susceptibility (c) for paramagnetism systems.

with the external field and becomes more linear at higher temperatures. According to Eq. 2.4 and Eq. 2.6, for small fields, where $\chi \ll 1$ and therefore $B \approx \mu_0 H$, $\chi$ can be calculated as

$$\chi = \frac{\mu_0 M}{B}. \tag{2.8}$$

Here the magnetization, **M**, according to Eq. 2.3, can be written using

$$M = n\langle\mu_z\rangle, \tag{2.9}$$

where $n = \frac{N}{V}$ and $\langle\mu_z\rangle$ is derived as $\frac{\mu^2 B}{3k_B T}$[37] representing the average moment along **B**. Hence, the volume magnetic susceptibility for small fields is obtained as

$$\chi = \frac{n\mu_0\mu^2}{3k_B T}. \tag{2.10}$$

This is known as the Curie's Law showing that the susceptibility is inversely proportional to the temperature. Curie's Law is often presented as

$$\chi = \frac{C_{Curie}}{T} \tag{2.11}$$

with $C_{Curie}$ being the Curie's constant. Also shown in Fig. 2.1(c), this susceptibility is positive at low field and becomes infinite at the absolute zero temperature. At room temperature, the paramagnetic molar susceptibility is of the order of $10^{-3}$ to $10^{-2}$ $cm^3 \cdot mol^{-1}$.

### Pauli paramagnetism

In metals, conduction electrons also contribute to the paramagnetism when an external field is applied. At low fields, the density of states for the free electrons is divided into two parts: electrons having their magnetic moments parallel or antiparallel to the external field. With the increasing of the field, the energy of the electrons with magnetic moments antiparallel to the filed is increased, while that of the other part of electrons is decreased. In order to maintain the constant Fermi level, a shift of energy is required. The electrons with magnetic moments antiparallel to the field have to lower their energy by flipping their spins. This leads to an excess of the magnetic moments parallel to the field and, therefore, gives rise to a paramagnetic magnetization.

For small fields, Pauli susceptibility, $\chi_P$, can also be calculated using Eq. 2.8. As free electrons have a spin of $\frac{1}{2}$ and $g = 2$, the magnetization can be obtained by

$$M = \mu_B(n_\uparrow - n_\downarrow). \tag{2.12}$$

where $n_\uparrow - n_\downarrow$ gives the difference of the number of electrons with their magnetic moments parallel ad antiparallel to the field. In this case, assuming that the energy shifts are negligible, we have that

$$n_\uparrow = n_\downarrow = \frac{1}{2}g(E_F)\mu_B B. \tag{2.13}$$

Hence, the Pauli magnetic susceptibility is given by

$$\chi_P = \mu_0\mu_B^2 g(E_F) = \frac{3n\mu_0\mu_B^2}{2E_F}, \tag{2.14}$$

where $n$ is the number of magnetic moment per unit volume and $E_F$ is the Fermi energy. Make use of $E_F = k_B T_F$, Eq. 2.14 can be written in a Curie-like form as

$$\chi_P = \frac{3n\mu_0\mu_B^2}{2k_B T_F}, \tag{2.15}$$

where $T_F$ is the Fermi temperature. Actually, Pauli paramagnetism is a very weak effect compared with the paramagnetism observed due to the Curie's Law.

## 2.3 Magnetic ordering

The paramagnetic behaviors described so far ignore the possible interaction between magnetic moments. In case of significant interaction between moments, the Curie law is renormalized. Moreover, spontaneous magnetic ordering in the absence of an applied magnetic field can also be observed. Three types of magnetic ordering are commonly observed: ferromagnetic, antiferromagnetic, and ferrimagnetic.

### 2.3.1 Ferromagnetism

Ferromagnetic ordering originates from the parallel arrangement of the magnetic moments, as shown in Fig. 2.2(a). However, this spontaneous ordering vanishes when the temperature increased to $T_c$, the Curie temperature. This temperature separates the ferromagnetic phase for $T < T_c$ from the disordered paramagnetic phase for $T > T_c$. In the paramagnetic phase, the field dependence of the magnetization is the same as that of the paramagnetic substances as presented by curves $T = T_2$

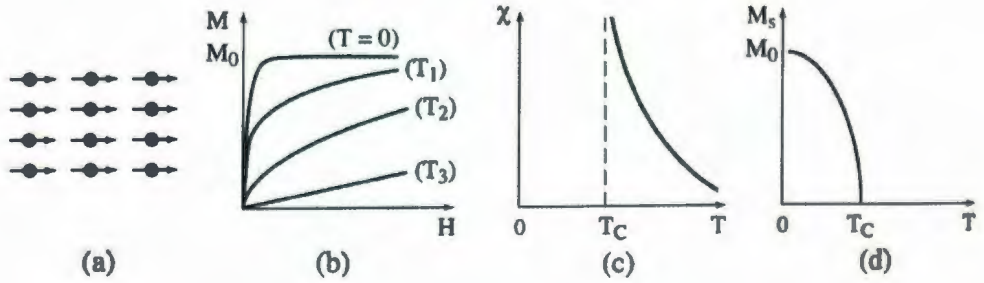


Figure 2.2: Ferromagnetism: (a) Spin lattice; (b) Field dependence of the magnetization ($T_1 < T_c \leqslant T_2 < T_3$); (c)Temperature dependence of the susceptibility; (d) Temperature dependence of the spontaneous magnetization.

and $T = T_3$ in Fig. 2.2(b). However, for $T < T_c$, as shown by Fig. 2.2(d), a spontaneous magnetization, $M_s$, appears at zero field and reaches its maximum value at zero Kelvin. Moreover, as illustrated in Fig. 2.2(c), instead of diverging at zero Kelvin for paramagnetic materials, the ferromagnetic susceptibility is given by the Curie-Weiss law,

$$\chi = \frac{C}{T - T_c} \qquad (T > T_c), \tag{2.16}$$

and shows a singularity at $T = T_c$.

### 2.3.2 Antiferromagnetism

A rather different situation is observed for antiferromagnetic ordering. As shown in Fig. 2.3(a), for a simple antiferromagnetic order the magnetic moments are distributed into two sublattices, their magnetization are equal in magnitude but opposite in direction. Therefore, no net magnetization is observed at zero field. As illustrated in Fig. 2.3(c), the temperature dependence of the susceptibility exhibits a maximum at

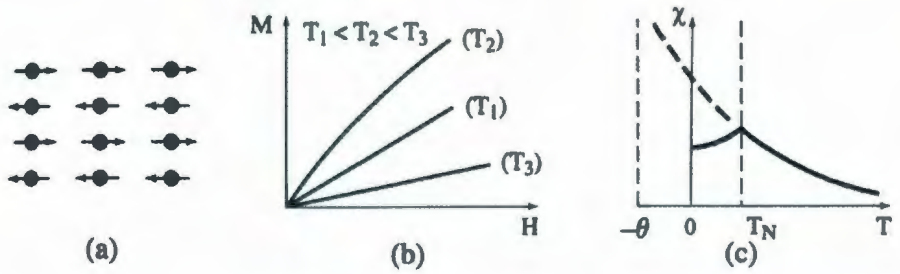


Figure 2.3: Antiferromagnetism: (a) Spin lattice; (b) Field dependence of the magnetization; (c)Temperature dependence of the susceptibility.

the so called Néel temperature $T_N$. This is due to the antiferromagnetic to paramagnetic transition at $T = T_N$. When the temperature is lower than $T_N$, the susceptibility decreases. Above $T_N$, as shown in Fig. 2.3(b) and Fig. 2.3(c), a paramagnetic behavior is observed from both the field dependence of the magnetization and the temperature dependence of the susceptibility. The susceptibility in the paramagnetic region $T > T_N$ is obtained as

$$\chi = \frac{C}{T+\theta} \qquad (T > T_N), \tag{2.17}$$

where $\theta$ is an experimental factor and often be studied experimentally in the form of $\frac{\theta}{T_N}$.

Besides the simplest case shown in Fig. 2.3(a), there exist many antiferromagnetic

substances with complex magnetic structures, especially geometrically frustrated systems. The simplest example is that of three magnetic moments on a triangular lattice shown in Fig. 1.1. Among these three magnetic moments, a 120° configuration is adopted, and then, the magnetic frustration is formed. Other types of geometrically frustrated lattice structures are shown in Fig. 2.4.

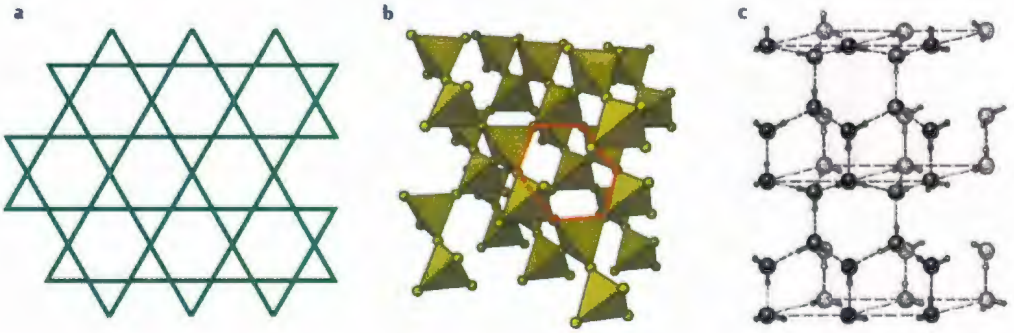


Figure 2.4: Frustrated lattices[12]. (a) The kagome lattice consists of vertex-sharing triangles. (b) The pyrochlore lattice is a net work of vertex-sharing tetrahedra. (c) Hexagonal ice consists of protons (small spheres) that reside on the bonds between two oxygen atoms (large spheres).

### 2.3.3 Ferrimagnetism

The ferrimagnetic ordering can be treated as a mixture between the antiferromagnetic and ferromagnetic cases. As shown in Fig. 2.5(a), there exist antiferromagnetic ordering between magnetic moments of different lattices, while ferromagnetic ordering between magnetic moments of the same lattice. This actually leads to a spontaneous magnetization for temperature below the Curie temperature $T_c$. In other words, as shown in Fig. 2.5(b) and Fig. 2.5(d), the behavior of the magnetization for $T < T_c$ is close to that of a ferromagnet, except that there exists a compensation temperature

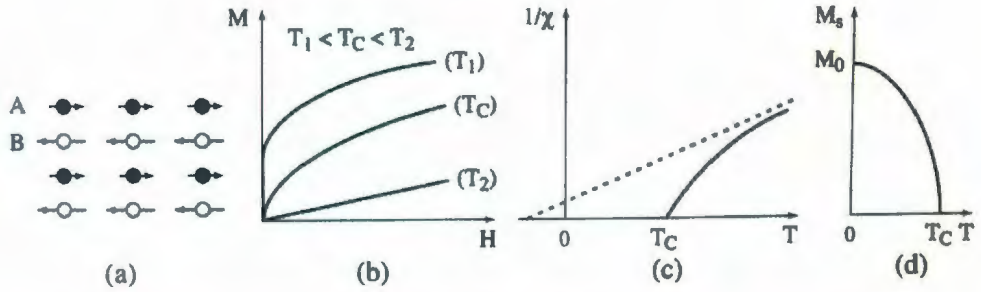


Figure 2.5: Ferrimagnetism: (a) Spin lattice; (b) Field dependence of the magnetization; (c)Temperature dependence of the susceptibility; (d) Temperature dependence of the spontaneous magnetization.

at which the spontaneous magnetization can be canceled due to the exact compensation of both sublattices. Furthermore, as presented in Fig. 2.5(c), the temperature dependence of susceptibility is almost linear at higher temperature. However, when approaching $T_c$, it obviously shift away from a linear behavior.

## 2.4 Exchange interaction

The long-range order of magnetic moments in solids is generally attributed to the short range interaction with each other. Besides the magnetic dipolar interaction, which is too weak to account for the ordering of most magnetic materials, the exchange interactions play the most important role in producing the long-range magnetic order.

The exchange interaction can be described by the exchange constant (or exchange integral) $J$. For a two electrons system,

$$J = \frac{E_S - E_T}{2}, \tag{2.18}$$

where $E_S$ and $E_T$ are energies of singlet state and triplet state, respectively, and the

Hamiltonian for this simple case is

$$\hat{\mathcal{H}}^{spin} = -2J\mathbf{S}_1 \cdot \mathbf{S}_2. \tag{2.19}$$

For a many-body system, Eq. 2.19 can be rewritten as

$$\hat{\mathcal{H}} = -\sum_{ij} J_{ij}\mathbf{S}_i \cdot \mathbf{S}_j \tag{2.20}$$

showing that interactions exist between all neighboring spins. Here, $J_{ij}$ is the exchange constant between the $i^{th}$ and $j^{th}$ spins. For ferromagnets, $J_{ij}$ is positive to ensure the ferromagnetic alignment, while for antiferromagnets, $J_{ij}$ is negative to favor that nearest neighbor magnetic moments are antiparallel to each other.

In some antiferromagnets, there exists an antisymmetric exchange interaction which is related to the overlap of electron distributions on neighboring ions. The magnetization generated from this interaction is directed along the certain crystallographic axes. Therefore, this exchange energy can be described as

$$\hat{\mathcal{H}}_{DM} = \mathbf{D} \cdot \mathbf{S}_1 \times \mathbf{S}_2. \tag{2.21}$$

To minimize $\hat{\mathcal{H}}_{DM}$, $\mathbf{S}_1$ and $\mathbf{S}_1$ are expected to be perpendicular to each other and in an plane that perpendicular to the vector $\mathbf{D}$ to ensure that $\hat{\mathcal{H}}_{DM}$ is negative. Actually, in antiferromagnets, with both negative exchange interaction $J_{ij}$ and $\mathbf{D}$, the nearest two magnetic moments form an angle by canting instead of being exactly antiparallel to each other.

## 2.5 Measurement of magnetic order

An obvious experiment method to detect the magnetic order is to measure the magnetization. One of the most sensitive techniques commonly used is the superconducting

quantum interference device (SQUID)[37]. A superconducting ring, which acts like a very sensitive quantum interferometer, is adopted in this method. When the sample passing through the ring, an induced persistent current, which is proportional to the magnetization in the sample, is obtained. Therefore, the magnetization in the sample can be determined by measuring the current.

A way to study the nature of a magnetic order is to analyze the magnetic susceptibility. Given that the magnetic susceptibility is given by $\frac{M}{H}$, magnetization techniques, for example the SQUID, can be used. A measurement used to determine small magnetic susceptibilities is called Gouy balance. By using this method, the weight change of the sample due to the application of a magnetic field is measured. This change of weight directly corresponds to the amount of unpaired electrons in the solid, and therefore can be used to extract the susceptibility.

In addition, the magnetic structure and dynamics can be studied using neutron scattering. This method is outstanding in gathering direct information on the configuration of the magnetic moments in the sample.

Many other techniques, such as nuclear magnetic resonance (NMR), Mössbauer, and $\mu$-SR experiments, are also used to effectively investigate the magnetism for materials. In our experiment, the ultrasonic velocity measurement is employed to study the nature of the magnetic phase diagram of the antiferromagnet $CsNiCl_3$.

# Chapter 3

# Crystal structure and magnetic properties of $CsNiCl_3$

$CsNiCl_3$ is one of the most studied antiferromagnetic compounds because of its novel properties at low temperatures. In order to better describe the magnetic properties of $CsNiCl_3$, in this chapter we present its crystal structure and its low-temperature magnetic phase diagram. A description of the different phase transitions, along with the spin configurations, are also included.

## 3.1 Crystal structure

$CsNiCl_3$ is a spin-1 hexagonal insulator with a $P6_3/mmc$ ($D^4_{6h}$) space group symmetry. The lattice constants of this compound are $a = b = 7.14$ Å and $c = 5.96$ Å at $T = 4.20$ K[41]. As shown in Fig. 3.1(a), there are two formula units per unit cell. Both of the lattices formed by $Cs^+$ and $Cl^-$ ions are hexagonal and the magnetic $Ni^{2+}$ ions, each surrounded by a trigonally distorted Cl-octahedron, are arranged in chains along the c-direction. Also shown in Fig. 3.1(b), which represents the top view of the

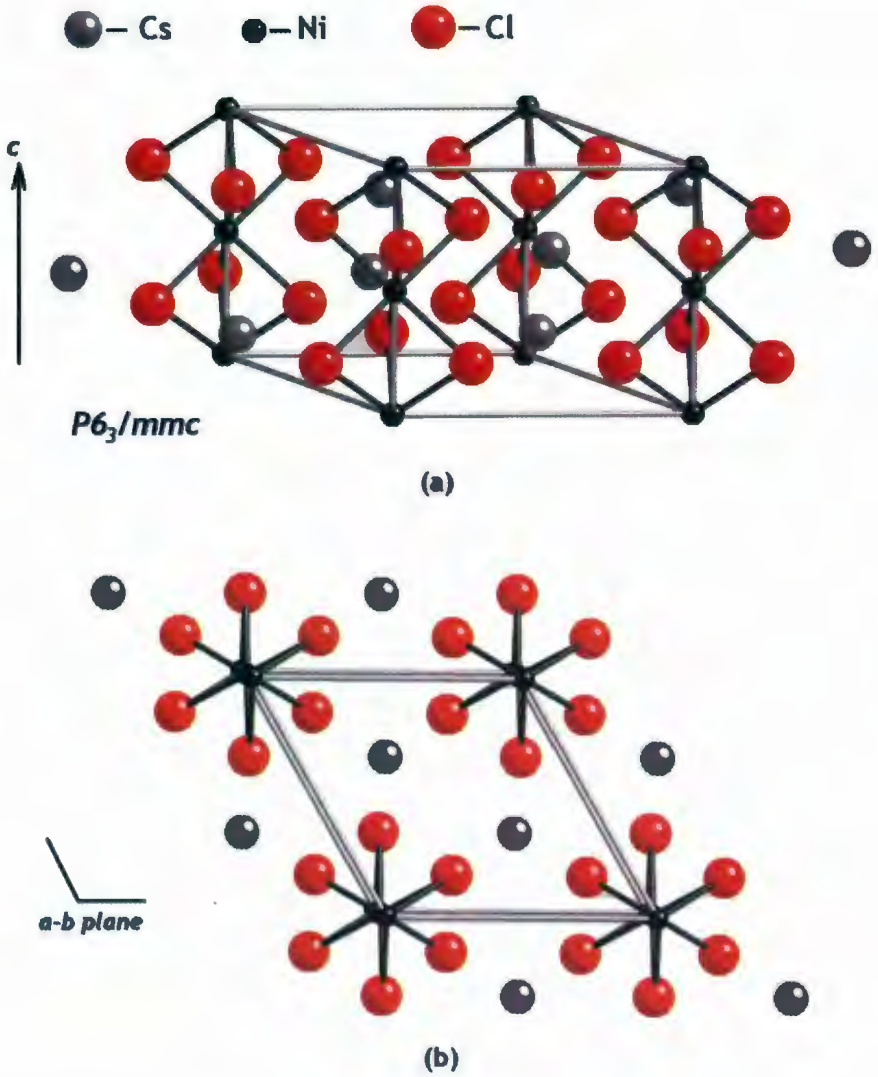


Figure 3.1: Crystal structure of $CsNiCl_3$ (a) and its projection onto the basal plane (b). Magnetic $Ni^{2+}$ moments are coupled along the c-direction via Ni-Cl-Ni paths (see (a)) and via Ni-Cl-Cl-Ni paths in the basal plane (see (b)).

crystal structure projected onto the basal plane, $Ni^{2+}$ moments are located on sites forming stacked layers of triangular planes.

## 3.2 Magnetic phase diagram

As shown in Fig. 3.1, in the basal plane, the $Ni^{2+}$ ions are coupled via a Ni-Cl-Cl-Ni path while along the c-direction the antiferromagnetic coupling is mediated through the Ni-Cl-Ni path. Therefore, the spin-spin interaction is mediated via the superexchange, the strong antiferromagnetic coupling between two magnetic nearest neighbor ions through a non-magnetic anion, between the $Ni^{2+}$ ions along the c-direction through $Cl^-$ anions while no such superexchange exists in the basal plane. This leads to a stronger interaction between $Ni^{2+}$ ions along the chain (c-direction) relative to the basal plane exchange[1]. This anisotropy in the magnetic interaction is well accounted for by the spin Hamiltonian[42]

$$\mathcal{H} = -J_{\parallel} \sum_{i}^{chain} \mathbf{s}_i \cdot \mathbf{s}_{i+1} - J_{\perp} \sum_{i \neq j}^{plane} \mathbf{s}_i \cdot \mathbf{s}_j - D \sum_i (s_i^z)^2 + g\mu_B \mathbf{H} \cdot \sum_i \mathbf{s}_i, \qquad (3.1)$$

where $\mathbf{s}$ is the spin of magnetic ion, $J_{\parallel}$ and $J_{\perp}$ represent the exchange integral along the c-direction and in the basal plane, respectively. According to early works (see Ta-

| Experimental method | $J_{\parallel}/k_B$(K) | $J_{\perp}/k_B$(K) | $D/k_B$(K) |
|---|---|---|---|
| Susceptibility[43] | $-12.1$ | | |
| Optical absorption[44], neutron diffraction[45] | $-13 \sim -16$ | $-0.3 \sim -0.4$ | $0.11 \sim 0.14$ |
| Spin flop field[4] | | | $\leqslant 0.035$ |
| Polarized neutron inelastic scattering[46] | $-16.6$ | 0.1 | $\leqslant 0.035$ |

Table 3.1: Microscopic parameters as determined by different experimental methods.

ble 3.1), both couplings are antiferromagnetic with $J_{\parallel}$ almost two orders of magnitude larger than $J_{\perp}$. For this reason, $CsNiCl_3$ is a good archetype for quasi-one dimensional antiferromagnets. As the single ion anisotropy, $D$ is also small compared with the exchange integrals $J_{\parallel}$ and $J_{\perp}$, $CsNiCl_3$ can also be treated as a nearly isotropic Heisenberg antiferromagnet. The last term in Eq. 3.1 is the Zeeman energy. For a magnetic field applied along c-direction, this term can be simplified to $g\mu_B H \sum_i s_i^z$, where $H$ represents the applied magnetic field.

The magnetic phase diagram of $CsNiCl_3$ for a field applied along the c-direction is shown in Fig. 3.2[16]. A paramagnetic phase and three ordered phases are separated by four phase transition lines emanating from a multicritical point at ($T_m \approx 4.60$ K, $H_m \approx 2.29$ T), which is also called a tetracritical point. As illustrated in the phase diagram, two second-order phase transitions are observed at low fields and the criticality along these phase boundaries is expected to belong to the $XY$ universal class. At zero field, the transitions happen at $T_{N1} \approx 4.85$ K and $T_{N2} \approx 4.40$ K, respectively. In the intermediate phase (for $T_{N2} < T < T_{N1}$), one-third of the spins are aligned parallel to the c-direction with the other spins pointing in the opposite c-direction and canting at an angle $\theta$. As only the component parallel with c-direction is ordered, this state is normally referred as the linear phase. In other words, only the parallel components of the other two-thirds spins are ordered. With a further decrease in temperature, in-plane ordering becomes stronger and the spin configuration changes into an elliptical order. Here, the components in the basal plane are also aligned antiparallel. Both of these two states can be characterized as a period-3 basal-plane modulation with an additional simple period-2 antiferromagnetic alignment along the c-direction[11]. These spin configurations have been confirmed by neutron scattering, ESR, and NMR measurements[47]–[52].

The most unusual phase happens with an external magnetic field applied along

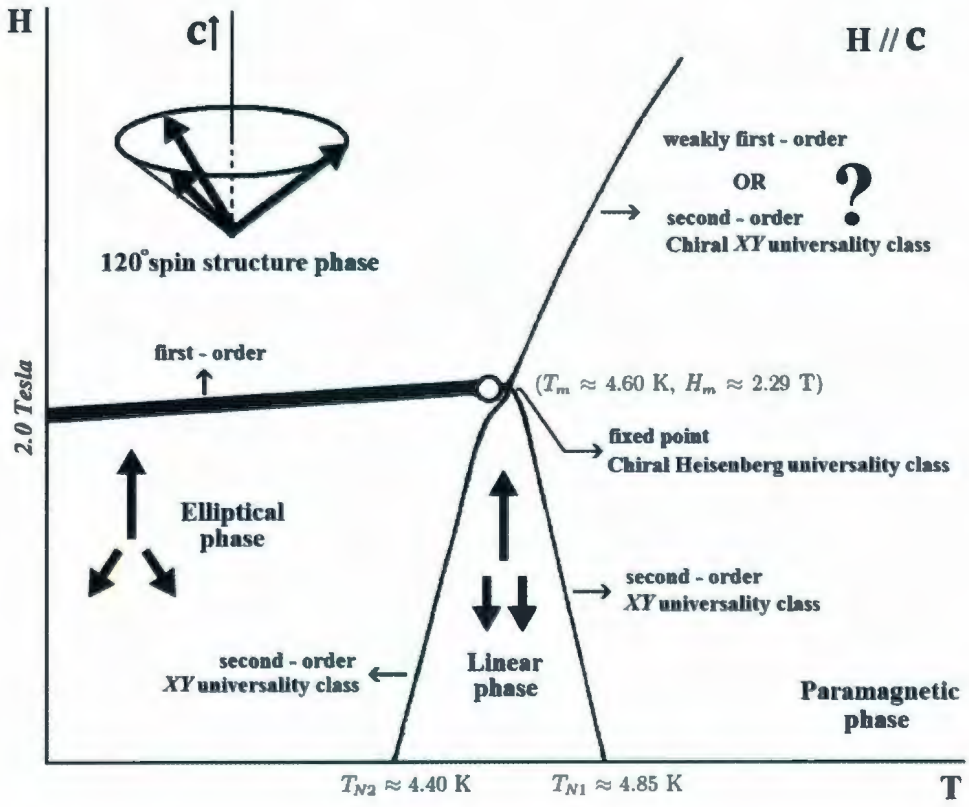


Figure 3.2: Magnetic phase diagram of $CsNiCl_3$ for a magnetic field oriented along the c-direction. The spin configurations, described in the text, are also illustrated.

the c-direction at low temperatures. As shown in the phase diagram, at $T < T_{N2}$, a first-order spin-flop phase transition at $H \approx 2.00$ T leads to a $120^{\circ}$ spin configuration. In this phase, the spins are aligned almost in the basal plane with a small canting angle relative to the basal plane. As the field is increased, the canting angle increases, resulting into a larger net magnetization along the c-direction. The spin basal plan components form a $120^{\circ}$ structure as in the case of easy-plane anisotropy. The phase transition between the $120^{\circ}$ phase and paramagnetic phase is predicted to be continuous and should belong to the chiral $XY$ universality class[13]–[16]. However, other theoretical studies and numerical simulations[20]–[26] support an alternative statement that the $120^{\circ}$ phase transition line should rather be characterized by a weakly first-order type.

# Chapter 4

# Experimental setup

The elastic constants, which are thermodynamic properties susceptible to the spin configurations in the crystal through magnetoelastic coupling, can be determined from ultrasonic velocity measurements[53]. Therefore, ultrasonic velocity measurements as function of both temperature and magnetic field can be used to probe the magnetic phase diagram. In addition, to detect the critical behavior close to a phase transition, a high-precision method is required. Thus, for our investigation, high-resolution ultrasonic velocity measurements, which can achieve resolutions as high as 1 part per million (1ppm), are used to examine the elastic properties of $CsNiCl_3$. To obtain this type of resolution, the acoustic interferometer technique is used to measure the relative sound velocity $\frac{\Delta v}{v}$ instead of the absolute velocity.

In this chapter, we first introduce the $CsNiCl_3$ sample and transducers employed in our experiments. Then, the high-resolution ultrasonic velocity measurements are described in detail.

## 4.1 $CsNiCl_3$ sample crystal and piezoelectric transducers

The $CsNiCl_3$ single crystal used in our experiment was grown by the Bridgman method. This method involves heating polycrystalline material in a container above its melting point and cooling it from one end where a seed crystal is located. Then, single crystal material can be progressively formed along the length of the container. Our sample crystal has approximately the shape of rectangular solid with a length of 8.9 mm along the c-direction and an area of 2.5 mm $\times$2.5 mm in the basal plane. Longitudinal or transverse elastic waves are produced by piezoelectric transducers mounted on one surface in the reflection configuration (see Fig. 4.2(a)), or two paralleled surfaces in the transmission configuration (see Fig. 4.2(b)).

In conventional applications, the upper limit of the ultrasonic frequency range is about 10 MHz. However, in some applications, the frequency can be as high as 5 GHz. In our experiment, the ultrasonic velocity is measured with the standard pulse-echo method at a frequency of about 30 MHz. As shown in Fig. 4.1, a transducer is a piezoelectric crystal with two gold electrodes evaporated on the crystal extremities. Thus, the RF signal applied to these electrodes is converted into mechanical vibrations by the piezoelectric crystal. In our experiment the transducers are bonded on the sample by a glue which works well at low temperatures. Because of the piezoelectric effect, the transducer vibrates at the same frequency as that of the oscillating electrical field applied to the electrodes (see Fig. 4.2(a)). In the reflection configuration, the transducer bonded to one of the two parallel faces of the crystal acts as the emitter and receiver. The mechanical vibration of the transducer generates a sound wave that propagates in the sample. Reflected by the extremities, the sound wave travels back and forth in the crystal. Due to the inverse piezoelectric effect, each time the sound

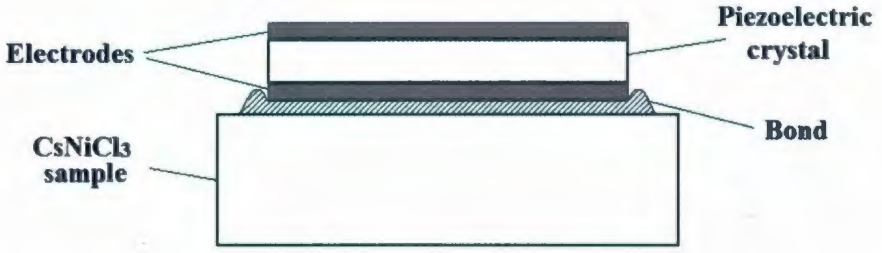


Figure 4.1: Transducer-Bond-Sample arrangement.

wave returns to the transducer, a small fraction of the mechanical energy is converted into an electrical signal which is detected, as shown by Fig. 4.3. In the transmission configuration, Fig. 4.2(b), the transmission and reception stages are decoupled using two transducers. In both cases, in order to determine the time of flight of the acoustic wave between the transmitter and receiver, 1 μs RF pulses are typically used.

## 4.2 Low-temperature and high magnetic field system

A helium bath cryostat containing a superconducting magnet has been used for this investigation. By using liquid helium as the cryogen, the temperature of the system can be as low as 2 K, at which the superconducting magnet is able to generate variable magnetic field up to 15 Tesla. These conditions are indispensable for the investigation of the low-temperature phase transitions observed in $CsNiCl_3$.

As shown in Fig. 4.4, before transferring liquid helium in the reservoir, the insert and sample chamber of the system must be evacuated to avoid the blockage of capillary due to the frozen air or nitrogen. The outer chamber is also under vacuum to

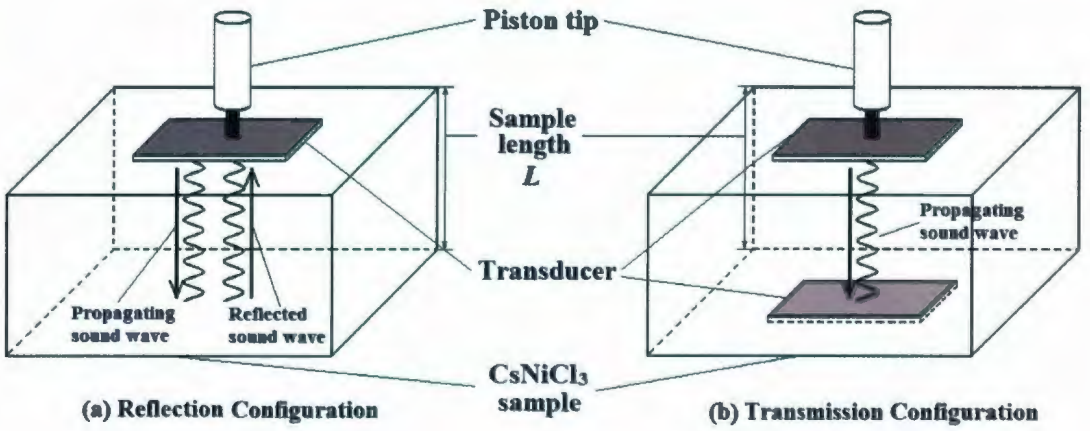


Figure 4.2: Schematic of the propagating of the sound wave in the crystal for both reflection (a) and transmission (b) configurations. For the reflection configuration, the transducer acts as both the emitter and receiver. For the transmission configuration, the transducers bonded on the top and bottom surfaces act as emitter and receiver, respectively. Here the piston is used to improve the coupling between the transducer and the crystal by producing a gentle force on the transducer due to a small compressed spring.

a superinsulation status. This helps to reduce the heat flow from the outside wall of the cryostat which is at room temperature. After the liquid helium transfer, the lower part of the helium reservoir is cooled down to 4.2 K by the liquid helium bath. Meanwhile, the cold gas that evaporates from the liquid helium is used to cool the radiation baffles in the higher part of the inner chamber. This vapor shield, again, protects the helium reservoir from the room temperature radiation heat. The $CsNiCl_3$ crystal is mounted on the sample holder, which is attached on a long probe inside

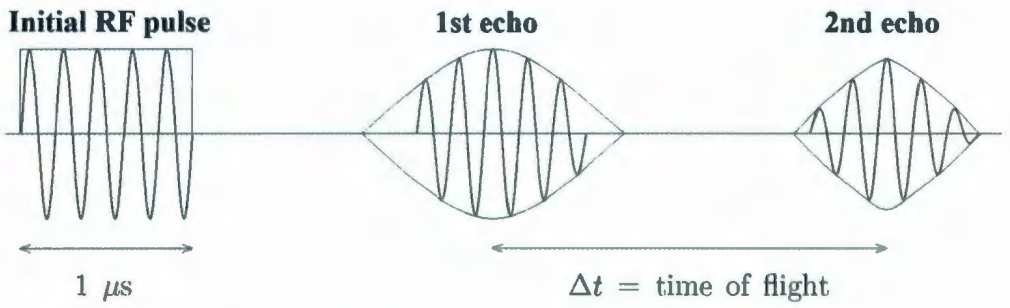


Figure 4.3: Consecutive echoes detected by the receiver. The decrease of the amplitude with the time of flight is due to the acoustic attenuation as the sound wave propagates in the crystal.

the sample chamber. To cool down the $CsNiCl_3$ sample, we need to adjust the capillary to let the helium flow into the sample chamber. At the same time, the safety pressure relief is opened to keep the positive pressure, which can maintain a proper flow of liquid helium from the reservoir into the sample chamber. As the helium gas flows into the sample chamber, $CsNiCl_3$ sample is cooled down. The temperature regulation is achieved by adjusting the power input of the heater inside the sample chamber. Furthermore, by decreasing the pressure inside the sample chamber, the boiling point of helium is decreased and a temperature of about 2 K can be achieved around the sample holder.

The superconducting magnet in this system is a solenoid with a bore radius of 52 mm. This type of magnet works well normally at 4.2 K up to a magnetic field to 13 T. However, lower temperatures can be used to enhance the performance of the magnet, especially for generating magnetic fields up to 15 T. Lambda refrigerators are designed to cool the magnet to about 2.2 K and maintain this temperature continuously[54]. In our system, as shown by the lower part of Fig. 4.4, the lambda

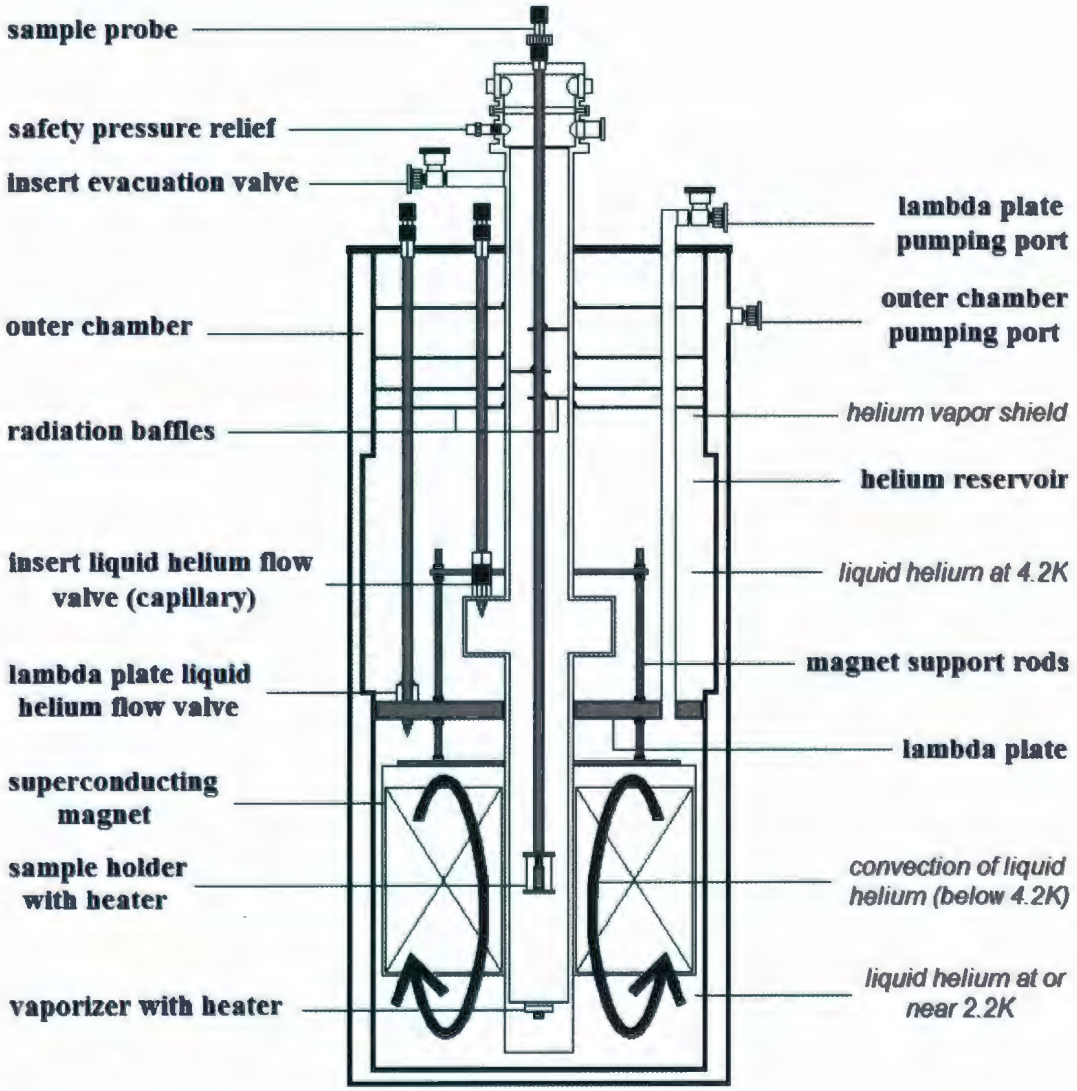


Figure 4.4: Low-temperature and high magnetic field system.

refrigerator consists of a lambda plate, a liquid helium flow valve, and a chamber with a pumping line. Liquid helium is continuously supplied to the lambda chamber via a valve and pumped to a low pressure in order to reduce the temperature inside the chamber attached to the lambda plate. As the liquid helium below the lambda plate is cooler and denser it sinks and induces the convection currents. This convection of the liquid helium maintains the temperature of the superconducting magnet at around 2.2 K, which improves the magnet performance.

## 4.3 Ultrasonic velocity measurements and acoustic interferometer

In the past few decades remarkable progress has been made in the techniques of high-resolution sound velocity measurements. In the reflection configuration, the absolute sound velocity can be determined using

$$v = \frac{2L}{\Delta t}, \tag{4.1}$$

where $\Delta t$ is the measured time of flight for an acoustic wave that travels a total distance of $2L$, $L$ being the sample length.

For higher resolution measurements, an acoustic interferometer is normally used. With this method, the relative change in the velocity, $\frac{\Delta v}{v}$, is measured instead of the absolute velocity. As shown in Fig. 4.5, the principle of this approach is to detect the phase difference between a reference signal and an echo coming from the sample. As shown in the diagram, the continuous RF signal produced by a frequency synthesizer is divided into two parts by the power splitter. The first branch is used as our reference signal. Using Gate 1, the second branch is reshaped to form a $\sim$ 1 μs RF pulse signal, which is then amplified by a 1 Watt broadband power amplifier.

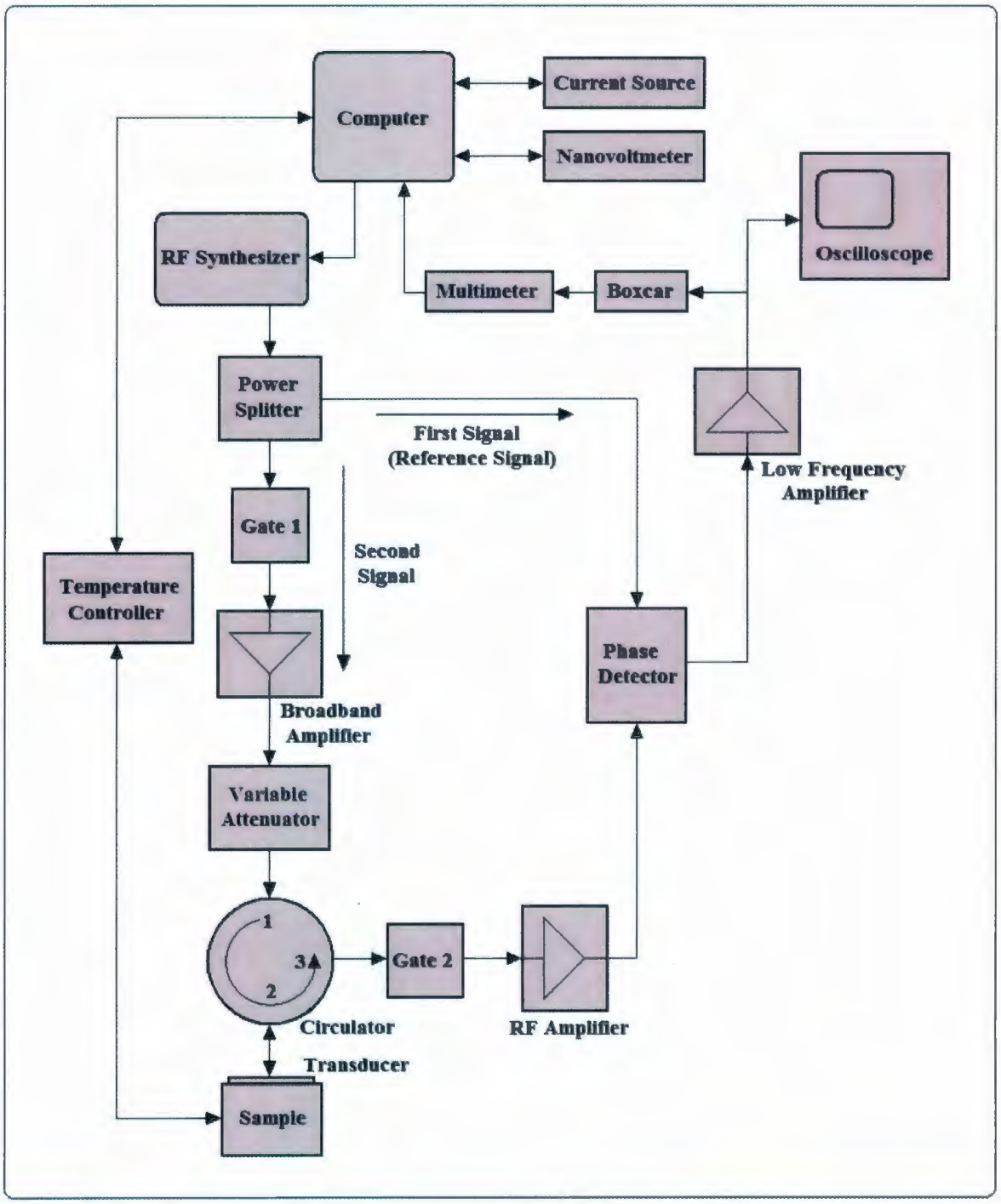


Figure 4.5: Brief block diagram of the acoustic interferometer.

The power used during the experiment is set by a variable attenuator. Then, the attenuated signal is directed to the sample via a circulator, which prevents any large signal from being reflected back to the synthesizer. The RF pulse signal that reaches to the transducer mounted on the crystal is then converted into an acoustic wave via the piezoelectric effect. The acoustic echo then travels between the extremities of the sample. Every time the wave reaches the transducer, a small fraction of the energy is converted back into a RF signal, via the inverse piezoelectric effect. This RF multi-echo pattern then passes through the circulator again via position 2 to position 3 and flows to Gate 2, which is used to filter out the initial pulse from the echo pattern to prevent the saturation of the low noise RF amplifier. Finally, the phase of the RF echo is compared to that of the reference signal using the phase detector, which gives a signal proportional to the phase difference. Under normal conditions, the relative phase of many echoes are observed on the oscilloscope as shown in Fig. 4.6. For the $n$-th echo, given that the period of the RF signal is $T$ and the time of flight corresponds to $\Delta t_n = \frac{2nL}{v}$, the phase difference $\Phi_n$ is simply given as

$$\Phi_n = 2\pi \frac{\Delta t_n}{T} = 2\pi f \frac{2nL}{v} = \frac{4\pi nLf}{v}. \tag{4.2}$$

So the relative phase change of the $n$-th echo can be derived as

$$\frac{\Delta\Phi_n}{\Phi_n} = \frac{\Delta f}{f} + \frac{\Delta L}{L} - \frac{\Delta v}{v}. \tag{4.3}$$

During the experiment, a boxcar is used to measure the phase of one specific echo. The boxcar is also part of a retroaction loop where a computer is used to maintain the phase difference to zero by changing the frequency of the RF signal. Under this condition, Eq. 4.3 reduces to

$$\frac{\Delta v}{v} = \frac{\Delta f}{f} + \frac{\Delta L}{L}, \tag{4.4}$$

which relates the relative velocity $\frac{\Delta v}{v}$ to the sample's expansion $\frac{\Delta L}{L}$. In general, the sample's thermal expansion[55] and magnetostriction[6], as a function of temperature

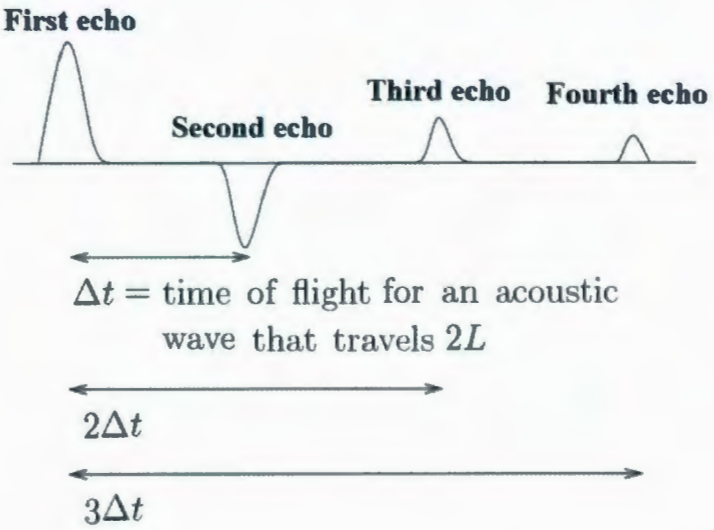


Figure 4.6: A typical multi-echo pattern showing the relative phase shift of four echoes observed on the oscilloscope for the case of the reflection configuration. The time of flight $\Delta t$ between the first and second echo is the time for an acoustic wave to travel a distance $2L$, from the top surface to the bottom then back to the top. The time $n\Delta t$ is the time between the first and the $n$-th echo.

or magnetic field, are orders of magnitude smaller than the variation of the velocity $\frac{\Delta v}{v}$. As a result, if we neglect the sample's expansion, the relative change in velocity can be expressed as

$$\frac{\Delta v}{v} \cong \frac{\Delta f}{f}. \tag{4.5}$$

Thus, by measuring the relative variation of the frequency, we directly obtain the relative change in the sound velocity.

# Chapter 5

# Crystalline elasticity

The goal of this chapter is to introduce some fundamental background knowledge about crystalline properties[56]. Both static and dynamic elasticity are presented in the following sections. The definitions of strain and stress are illustrated in Sections 5.1 and 5.2, while their linear relationship, represented by elastic constants, are given in Section 5.3. Then, based on the theory of plane wave propagation, the dynamic elastic properties are described in Section 5.4. In this section, the Christoffel equation is used to derive the velocity of the plane waves propagating along high symmetry axis.

## 5.1 Static elasticity - strain

Generally speaking, strain $e$ is a concept used to describe the deformation of the solid. Instead of dealing with a complex real three-dimensional case, here we describe the definition of strain $e$ with a simple one-dimensional string. As shown in Fig. 5.1, the length of a string of length $L$ increases under an external force $F$. Given the original and new length of the string as $L$ and $L'$, the relative deformation is $\frac{L'-L}{L}$. Because

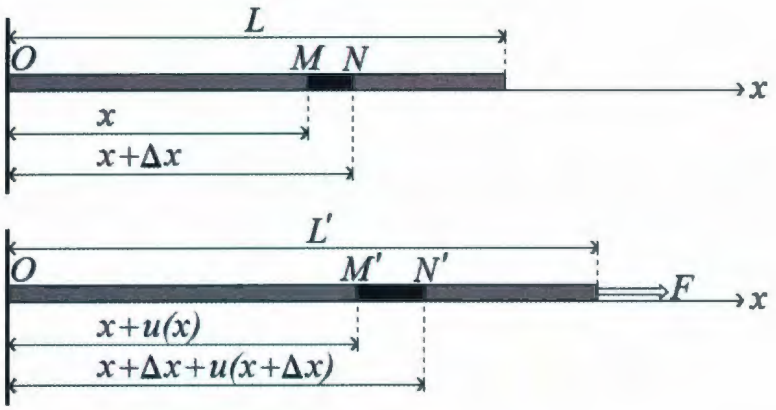


Figure 5.1: Deformation of a string.

it is not necessary that every point on the string be stretched in the same way, we should first define the deformation of a small element and then expand to the vicinity. Therefore, as sketched in Fig. 5.1, points $M$ and $N$ are used to define a small portion $\Delta x$. Before the application of the force, $M$ and $N$ are described by $x$ and $x + \Delta x$. When the force is applied, these two points move to $M'$ and $N'$, respectively. If $u(x)$ and $u(x + \Delta x)$ represent the local deformations, the relative deformation of the section $MN$ can be rewritten as

$$\frac{\overline{M'N'} - \overline{MN}}{\overline{MN}} = \frac{u(x + \Delta x) - u(x)}{\Delta x}. \tag{5.1}$$

Taking the limit $\Delta \to 0$, the strain $e$ reduces to

$$e = \lim_{\Delta x \to 0} \frac{u(x + \Delta x) - u(x)}{\Delta x} = \frac{du}{dx}, \tag{5.2}$$

which is dimensionless.

The deformation for a three-dimensional solid is more complex. For the one-dimensional system, every two points on the string are displaced in the same direction.

However, for a real solid, neighboring points might be stretched in different directions. Thus, in this case the displacements are described by $\vec{u}(\vec{x})$ with

$$d\vec{u} = \frac{\partial \vec{u}}{\partial x_i} dx_i. \tag{5.3}$$

Given this relation, the deformation in the direction $i$ corresponds to

$$du_i = \frac{\partial u_i}{\partial x_j} dx_j. \tag{5.4}$$

Generalizing Eq. 5.2 to a three-dimension solid, the strain must be represented by a second-rank tensor with the elements given by

$$e_{i,j} = \frac{du_i}{dx_j}, \tag{5.5}$$

which can be rewritten into a symmetric and an antisymmetric components as

$$\frac{du_i}{dx_j} = \frac{1}{2}(\frac{\partial u_i}{\partial x_j} + \frac{\partial u_j}{\partial x_i}) + \frac{1}{2}(\frac{\partial u_i}{\partial x_j} - \frac{\partial u_j}{\partial x_i}). \tag{5.6}$$

The first part on the right hand side of Eq. 5.6 represents the strain

$$e_{i,j} = \frac{1}{2}(\frac{\partial u_i}{\partial x_j} + \frac{\partial u_j}{\partial x_i}) \tag{5.7}$$

while the second part corresponds to a rigid-body rotation. As the strain tensor is symmetric relative to the index permutation,

$$e_{i,j} = e_{j,i}, \tag{5.8}$$

the strain tensor

$$e = \begin{pmatrix} e_{1,1} & e_{1,2} & e_{1,3} \\ e_{1,2} & e_{2,2} & e_{2,3} \\ e_{1,3} & e_{2,3} & e_{3,3} \end{pmatrix} \tag{5.9}$$

has a maximum of 6 independent components. Here, the components with $i \neq j$ involve shear deformations while the diagonal elements are associated with longitudinal deformations.

## 5.2 Static elasticity - stress

The stress is defined as the force acting on a unit area in the solid. In the case of orthonormal reference frame, as shown in Fig. 5.2, the stress components $T_{i,k}$ is

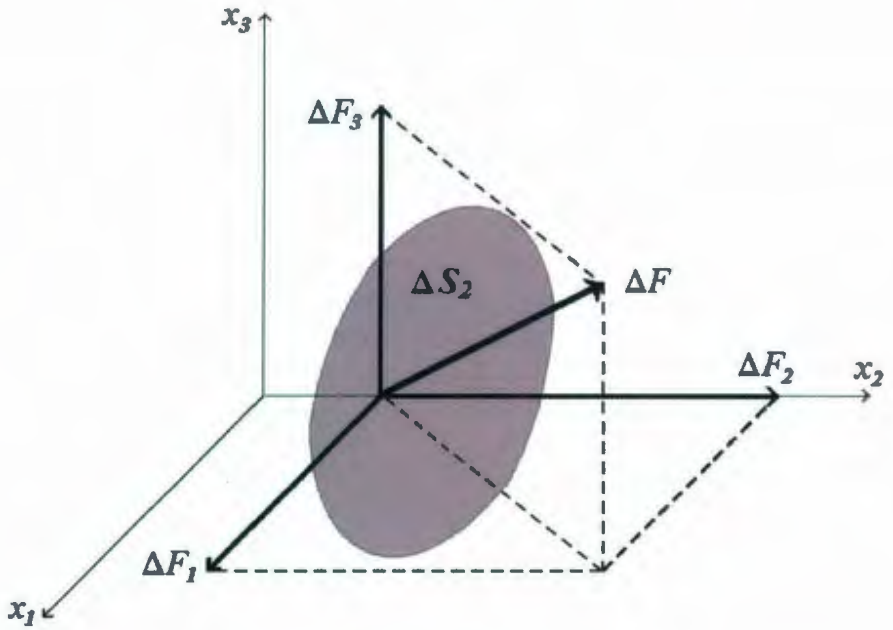


Figure 5.2: Force acting on an surface element $\Delta S_2$, which is orthogonal to $x_2$ axis in a co-ordinate system.

defined as

$$T_{i,k} = \lim_{\Delta S_k \to 0} \frac{\Delta F_i}{\Delta S_k}, \tag{5.10}$$

where $\Delta F_i$ is the $i$-th component of the force $\Delta \vec{F}$ exerted on the surface element $\Delta S_k$. So $T_{i,k}$ represents the $i$-th component of the force exerted on a unit surface, which is perpendicular to the $k$-axis. Given that $i$ and $k$ both run from 1 to 3 (orthonormal reference frame), the stress tensor $T$ has 9 components. As the net force and torque

for the whole system must be zero, this imposes that

$$T_{i,k} = T_{k,i}, \tag{5.11}$$

which shows that the stress tensor is also symmetric. Only 6 independent elements exist and the elements with $i \neq j$ correspond to shear stress while diagonal components represent longitudinal stress.

## 5.3 Static elasticity - elastic constants

In one-dimension, the deformation $x$ of an elastic material is described by the Hooke's law as

$$F = kx, \tag{5.12}$$

where $F$ is the applied force and $k$ is the "spring constant". When working with a three-dimensional crystal[56], for small deformations, the stress $T$ is directly proportional to the strain $e$. The static Hooke's law for a three-dimension body can be rewritten as

$$T_{i,j} = C_{i,j,k,l} e_{k,l}, \qquad i,j,k,l = 1,2,3, \tag{5.13}$$

where $T_{i,j}$ represents a force applied along the $i$-direction acting on a unit area normal to the $j$-direction, $e_{k,l}$ is the deformation per unit length $\frac{\partial u_l}{\partial x_k}$, and $C_{i,j,k,l}$ corresponds to the elastic constants.

The 4th-order tensor $C_{i,j,k,l}$ includes 81 components. Knowing that the internal energy variation can be described as

$$dU = T_{i,k} de_{i,k} + TdS, \tag{5.14}$$

Where $T$ is the absolute temperature and $S$ is the entropy, we have that

$$T_{i,k} = (\frac{\partial U}{\partial e_{i,k}})_S. \tag{5.15}$$

According to Eq. 5.12, we obtain

$$C_{i,j,k,l} = (\frac{\partial T_{i,j}}{\partial e_{k,l}}) = (\frac{\partial^2 U}{\partial e_{i,j} \partial e_{k,l}})_S = C_{k,l,i,j}. \tag{5.16}$$

As the stress and strain tensors are symmetric, and due to Eq. 5.16, we must have that

$$C_{i,j,k,l} = C_{j,i,k,l}, \qquad C_{i,j,k,l} = C_{i,j,l,k}, \qquad C_{i,j,k,l} = C_{k,l,i,j}, \tag{5.17}$$

which reduces the number of the elements in the elastic stiffness tensor to 21. Based on this symmetry, we can label these independent elastic constants using the Voigt notation in the following way:

$$\begin{aligned} &1 \leftrightarrow (1,1) && 2 \leftrightarrow (2,2) && 3 \leftrightarrow (3,3) \\ &4 \leftrightarrow (2,3) = (3,2) && 5 \leftrightarrow (1,3) = (3,1) && 6 \leftrightarrow (1,2) = (2,1). \end{aligned} \tag{5.18}$$

Accordingly, the 21 elastic constants can be represented as a $6 \times 6$ matrix

$$C = \begin{pmatrix} C_{11} & C_{12} & C_{13} & C_{14} & C_{15} & C_{16} \\ C_{12} & C_{22} & C_{23} & C_{24} & C_{25} & C_{26} \\ C_{13} & C_{23} & C_{33} & C_{34} & C_{35} & C_{36} \\ C_{14} & C_{24} & C_{34} & C_{44} & C_{45} & C_{46} \\ C_{15} & C_{25} & C_{35} & C_{45} & C_{55} & C_{56} \\ C_{16} & C_{26} & C_{36} & C_{46} & C_{56} & C_{66} \end{pmatrix}, \tag{5.19}$$

where $C_{\alpha\beta} = C_{i,j,k,l}$ with $\alpha \leftrightarrow (i,j)$ and $\beta \leftrightarrow (k,l)$.

The elastic energy described by this elastic tensor must be invariant under the particular symmetry operations for a certain system. In other words, the number of the independent elastic constants might be smaller than 21. For example, the main symmetry operations of the hexagonal system are $C_{6z}$ (6-fold rotation with respect to z-axis), $C_{2y}$ (2-fold rotation with respect to y-axis), and $I$ (inversion) and the matrix

of these symmetry operations are

$$\alpha_{6z} = \begin{pmatrix} \frac{1}{2} & \frac{\sqrt{3}}{2} & 0 \\ -\frac{\sqrt{3}}{2} & \frac{1}{2} & 0 \\ 0 & 0 & 1 \end{pmatrix}; \tag{5.20}$$

$$\alpha_{2y} = \begin{pmatrix} -1 & 0 & 0 \\ 0 & 1 & 0 \\ 0 & 0 & -1 \end{pmatrix}; \tag{5.21}$$

$$\alpha_I = \begin{pmatrix} -1 & 0 & 0 \\ 0 & -1 & 0 \\ 0 & 0 & -1 \end{pmatrix}. \tag{5.22}$$

In order to satisfy the invariant requirement,

$$C'_{i,j,k,l} = \alpha_i^m \alpha_j^n \alpha_k^p \alpha_l^q C_{m,n,p,q} = C_{i,j,k,l}, \tag{5.23}$$

only 5 independent elements are non-zero. So the elastic tensor for this case is rewritten as

$$C = \begin{pmatrix} C_{11} & C_{12} & C_{13} & 0 & 0 & 0 \\ C_{12} & C_{11} & C_{13} & 0 & 0 & 0 \\ C_{13} & C_{13} & C_{33} & 0 & 0 & 0 \\ 0 & 0 & 0 & C_{44} & 0 & 0 \\ 0 & 0 & 0 & 0 & C_{44} & 0 \\ 0 & 0 & 0 & 0 & 0 & \frac{1}{2}(C_{11} - C_{12}) \end{pmatrix}. \tag{5.24}$$

## 5.4 Dynamic elasticity - plane wave propagation

To describe the propagation of acoustic waves in solid, we need to start from the equation of motion which is related to Newton's law and Hooke's law. The force

density for material under stress is defined as

$$f_i = \frac{\partial T_{i,j}}{\partial x_j}. \tag{5.25}$$

According to Newton's second law, the force density $f_i$ can be expressed as

$$f_i = \rho \frac{\partial^2 u_i}{\partial t^2}, \tag{5.26}$$

where $\rho$ is the density, $\frac{\partial^2 u_i}{\partial t^2}$ stands for the acceleration and $u_i$ represents the $i$-th component of the displacement $u$. Combining Eq. 5.25 and Eq. 5.26, the equation of motion for the elastic medium can be written as

$$\rho \frac{\partial^2 u_i}{\partial t^2} = \frac{\partial T_{i,j}}{\partial x_j}. \tag{5.27}$$

Together with Hooke's law, Eq. 5.13, we rewrite this equation of motion as

$$\rho \frac{\partial^2 u_i}{\partial t^2} = C_{i,j,k,l} \frac{\partial^2 u_l}{\partial x_j \partial x_k}. \tag{5.28}$$

For plane waves, solution for this equation can be represented as

$$u_i = u_{0i} e^{i(\mathbf{k}\cdot\mathbf{r} - \omega t)} \qquad i = 1, 2, 3, \tag{5.29}$$

where $u_{0i} = \delta_{il} u_{0l}$ is the wave polarization (i.e. the particle displacement direction) while $\mathbf{k}$ and $\omega$ are the wave vector and the frequency, respectively. So Eq. 5.28 can be rewritten as

$$(\rho\omega^2 \delta_{il} - C_{i,j,k,l} k_j k_k) u_{0l} = 0. \tag{5.30}$$

Dividing both sides of Eq. 5.30 by $k^2$, we obtain the well-known Christoffel equation

$$(\rho v^2 \delta_{il} - C_{i,j,k,l} n_j n_k) u_{0l} = 0, \tag{5.31}$$

where $v = \frac{\omega}{k}$, the phase velocity, while $n_j$ and $n_k$ represent the cosine direction of the wave vector relative to a coordinate system associated with the proper axis of the crystal. If we define a second-rank tensor as

$$\Gamma_{il} = C_{i,j,k,l} n_j n_k, \tag{5.32}$$

the Christoffel equation can be written as,

$$(\Gamma_{il} - \rho v^2 \delta_{il}) u_{0l} = 0. \tag{5.33}$$

The velocity of the sound waves can be obtained by solving the secular equation

$$|\Gamma_{il} - \rho v^2 \delta_{il}| = 0. \tag{5.34}$$

For every direction of propagation, three different waves, one longitudinal mode and two transverse modes, with orthogonal polarizations, can be obtained. Longitudinal waves are polarized along the direction of propagation while transverse modes are polarized perpendicular to the direction of propagation. Thus, according to Eq. 5.34, the velocities depend directly on the elastic tensor. In the case of $CsNiCl_3$, based on the symmetry properties of the hexagonal system, only 5 independent components are necessary and the elastic tensor $C$ reduces to

$$C_{hexagonal} = \begin{pmatrix} C_{11} & C_{12} & C_{13} & 0 & 0 & 0 \\ C_{12} & C_{11} & C_{13} & 0 & 0 & 0 \\ C_{13} & C_{13} & C_{33} & 0 & 0 & 0 \\ 0 & 0 & 0 & C_{44} & 0 & 0 \\ 0 & 0 & 0 & 0 & C_{44} & 0 \\ 0 & 0 & 0 & 0 & 0 & C_{66} \end{pmatrix}, \tag{5.35}$$

where $C_{66} = \frac{1}{2}(C_{11} - C_{12})$. The sound velocity can always be written as

$$v = \sqrt{\frac{C_{eff}}{\rho}}, \tag{5.36}$$

where $C_{eff}$ represents the relevant combination of the independent elastic constants $C_{\alpha\beta}$ given in Eq. 5.35. For example, if the direction of propagation is along the z-direction, we have $n_1 = 0$, $n_2 = 0$ and $n_3 = 1$ and accordingly $\Gamma_{il} = C_{i,3,3,l}$. In this

case, the tensor $\Gamma_{il}$ is

$$\Gamma = \begin{pmatrix} C_{55} & C_{45} & C_{35} \\ C_{45} & C_{44} & C_{34} \\ C_{35} & C_{34} & C_{33} \end{pmatrix}. \tag{5.37}$$

As $C_{34} = C_{35} = C_{45} = 0$ and $C_{55} = C_{44}$ for a hexagonal system, the tensor reduces to

$$\Gamma = \begin{pmatrix} C_{44} & 0 & 0 \\ 0 & C_{44} & 0 \\ 0 & 0 & C_{33} \end{pmatrix}. \tag{5.38}$$

Hence, the eigenvalues correspond to

$$\lambda_1 = C_{33}, \qquad \lambda_2 = \lambda_3 = C_{44} \tag{5.39}$$

and the solutions for Eq. 5.34 are obtained as

$$v_1 = \sqrt{\frac{C_{33}}{\rho}}, \qquad v_2 = v_3 = \sqrt{\frac{C_{44}}{\rho}}. \tag{5.40}$$

The polarizations are given by the eigenvectors in Eq. 5.33 and correspond to

$$\lambda_1 : u_1 \rightarrow [0,0,1]; \quad \lambda_2 : u_2 \rightarrow [0,1,0]; \quad \lambda_3 : u_3 \rightarrow [1,0,0]. \tag{5.41}$$

Given that the direction of propagation is [0,0,1], the solution $u_1$ represents a longitudinal mode while $u_2$ and $u_3$ are associated with transverse modes.

For this investigation, measurements along the [100] and [001] direction have been made. The relations between the elastic constants and the sound velocities along the principal crystallographic directions are listed in Table 5.1.

| Direction | Mode | $\rho v^2$ |
|---|---|---|
| .. | $L_x$ | $C_{11}$ |
| [100] | $T_z$ | $C_{44}$ |
| .. | $T_y$ | $C_{66}$ |
| .. | $L_y$ | $C_{11}$ |
| [010] | $T_z$ | $C_{44}$ |
| .. | $T_x$ | $C_{66}$ |
| .. | $L_z$ | $C_{33}$ |
| [001] | $T_x$ | $C_{44}$ |
| .. | $T_y$ | $C_{44}$ |

Table 5.1: Relations among wave vectors, propagation modes, and elastic constants in hexagonal crystal, where $L_i$ is used for longitudinal waves and $T_j$ represents transverse waves with a polarization along the j-th axis.

# Chapter 6

# Experimental data

According to Eq. 5.36, the effective elastic constant $C_{eff}$ associated with an acoustic mode can be determined from velocity measurements using the usual relation

$$C_{eff} = \rho v^2, \tag{6.1}$$

where $\rho$ represents the density. For $CsNiCl_3$, given an estimated density of $\rho = 3700$ kg/m$^3$, the elastic constants have been obtained previously at room temperature as shown in Table 6.1[57]. According to Eq. 6.1, for small variation, the normalized

| Sound Velocities ($\pm 20$ m/s) | Elastic Constants ($\pm 0.05 \times 10^{10}$ N/m$^2$) |
|---|---|
| $v_L[100] = 6140$ | $C_{11} = 13.90$ |
| $v_L[001] = 4080$ | $C_{33} = 6.16$ |
| $v_{T_z}[100] = 2500$ | $C_{44} = 2.31$ |
| $v_{T_{\perp z}}[100] = 3100$ | $C_{66} = 3.56$ |
| $(C_{12} = C_{11} - 2C_{66})$ | $C_{12} = 6.78$ |

Table 6.1: Sound velocities and elastic constants measurements for $CsNiCl_3$ obtained at room temperature[57].

change of the elastic constant can be simply evaluated using

$$\frac{\Delta C_{eff}}{C_{eff}} = 2\frac{\Delta v}{v}. \tag{6.2}$$

For that reason, the temperature and magnetic field dependence of the relative variation of elastic constant, $\frac{\Delta C_{eff}}{C_{eff}}$, can be investigated by using the ultrasonic velocity measurements.

In our experiments, considering that the crystal symmetry of $CsNiCl_3$ is hexagonal, the behavior of $C_{33}$ and $C_{44}$ have been obtained using longitudinal ($L_z$) and transverse ($T_x$ or $T_y$) waves propagating along the main symmetry axis, [001]. For $C_{66}$, transverse modes ($T_x$ along the [010] or $T_y$ along the [100]) with the directions of propagation and polarization both perpendicular to the [001] direction had to be used. The transducers used for longitudinal modes $C_{33}$ and transverse modes $C_{44}$ are mounted on faces perpendicular to the [001] direction. For transverse modes $C_{66}$, the transducers are mounted on faces perpendicular to the [010] or [100] direction.

In this chapter, we first present the zero field temperature scan, while data as a function of temperature and magnetic field for $\frac{\Delta C_{33}}{C_{33}}$, $\frac{\Delta C_{44}}{C_{44}}$ and $\frac{\Delta C_{66}}{C_{66}}$ are reported in the second section. Finally, based on our experimental results, the experimental magnetic phase diagram of $CsNiCl_3$ is derived.

## 6.1 Temperature dependence at $H = 0$

The temperature dependence of $\frac{\Delta C_{33}}{C_{33}}$, $\frac{\Delta C_{66}}{C_{66}}$, and $\frac{\Delta C_{44}}{C_{44}}$ for $H = 0$, are presented in Fig. 6.1. According to the data, two phase transitions are observed with $T_{N1} \approx 4.75$ K and $T_{N2} \approx 4.35$ K. At $T_{N2} \approx 4.35$ K, the phase transition between the linear phase and the elliptical phase (L-E phase transition) is clearly visible on all three curves. Meanwhile, at $T_{N1} \approx 4.75$ K, we easily see the phase transition between

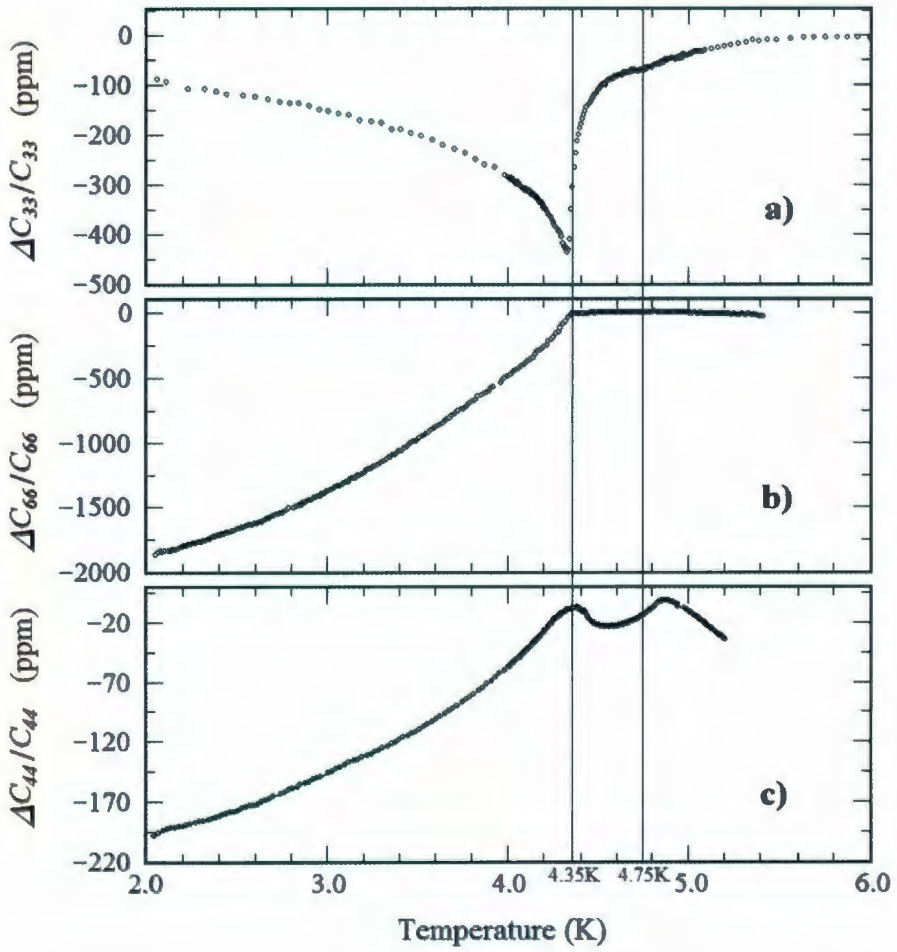


Figure 6.1: Temperature dependence of the relative variation of the elastic constants a) $C_{33}$, b) $C_{66}$, and c) $C_{44}$ at $H = 0$. The phases corresponding to $T < 4.35$ K, 4.35 K$\leqslant T \leqslant 4.75$ K, and $T > 4.75$ K are elliptical, linear, and paramagnetic phases, respectively.

the paramagnetic phase and the linear phase (P-L phase transition) from the data associated with $\frac{\Delta C_{33}}{C_{33}}$ and $\frac{\Delta C_{44}}{C_{44}}$. For $\frac{\Delta C_{66}}{C_{66}}$, the transition is also visible, however, the anomaly is barely noticeable. We also notice that, for $T < T_{N2}$, all three curves show a power law temperature dependence close to the critical temperature. However, the sign of the temperature dependence for $C_{33}$ is opposite to those of $C_{44}$ and $C_{66}$. The temperature dependence is analyzed in more details in Chapter 10.

## 6.2 Temperature and magnetic field dependence

The temperature dependence of $\frac{\Delta C_{33}}{C_{33}}$, $\frac{\Delta C_{44}}{C_{44}}$, and $\frac{\Delta C_{66}}{C_{66}}$, for a magnetic field applied along the c-direction, are shown in Fig. 6.2 - 6.4, respectively. Data obtained for magnetic fields lower than the multicritical field $H_m = 2.29$ T are presented by broken lines, while for higher fields continuous lines are used for clarity. At lower fields ($H < H_m$), data for $\frac{\Delta C_{33}}{C_{33}}$ (Fig. 6.2) and $\frac{\Delta C_{44}}{C_{44}}$ (Fig. 6.3) show anomalies corresponding to the P-L and L-E phase transitions. However, from $\frac{\Delta C_{66}}{C_{66}}$ (Fig. 6.4), only the anomaly corresponding to the L-E phase transition is clearly visible. At higher magnetic fields, all data sets show one phase transition that can be associated with the $120^{o}$ phase.

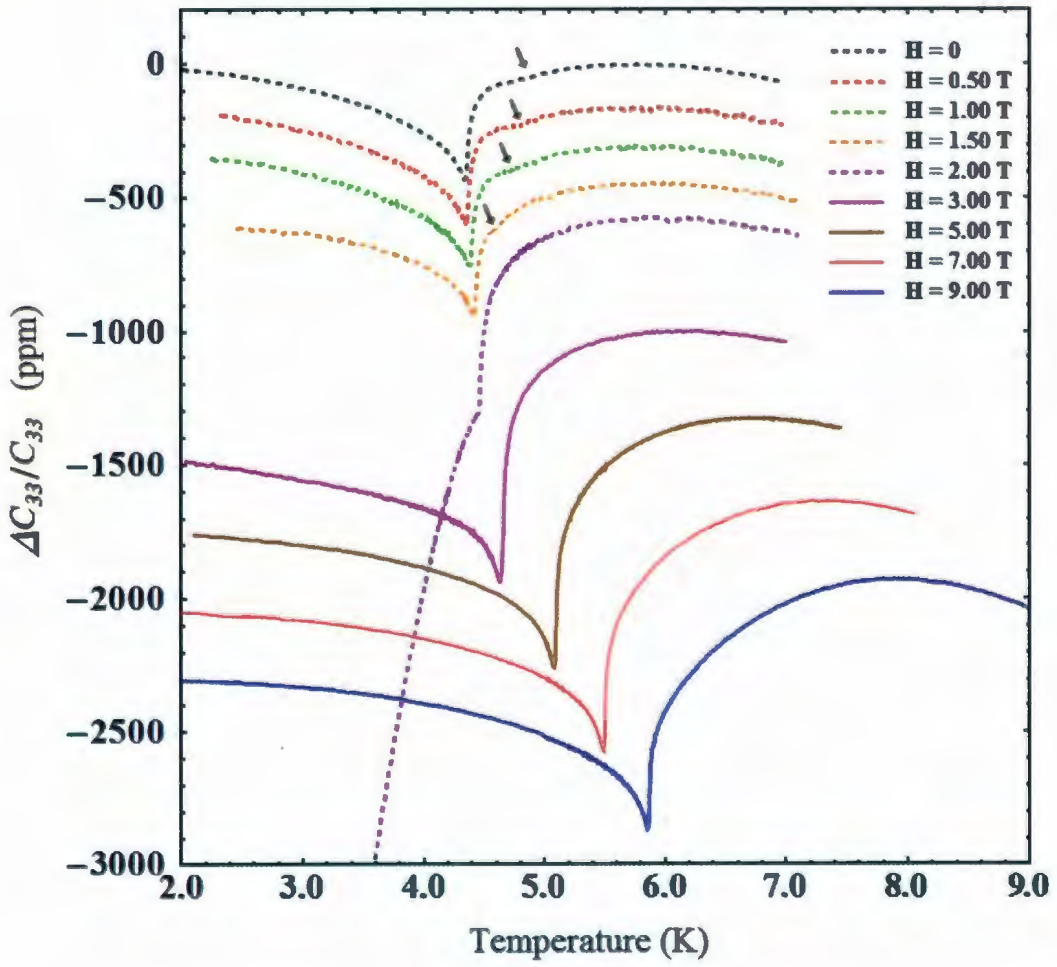


Figure 6.2: Relative variation of the elastic constant $C_{33}$ as a function of temperature at different magnetic fields. Phase transitions between paramagnetic phase and linear phase are indicated by the small arrows. The continuous and broken lines represent data obtained above and below the multicritical field ($H_m = 2.29$ T), respectively.

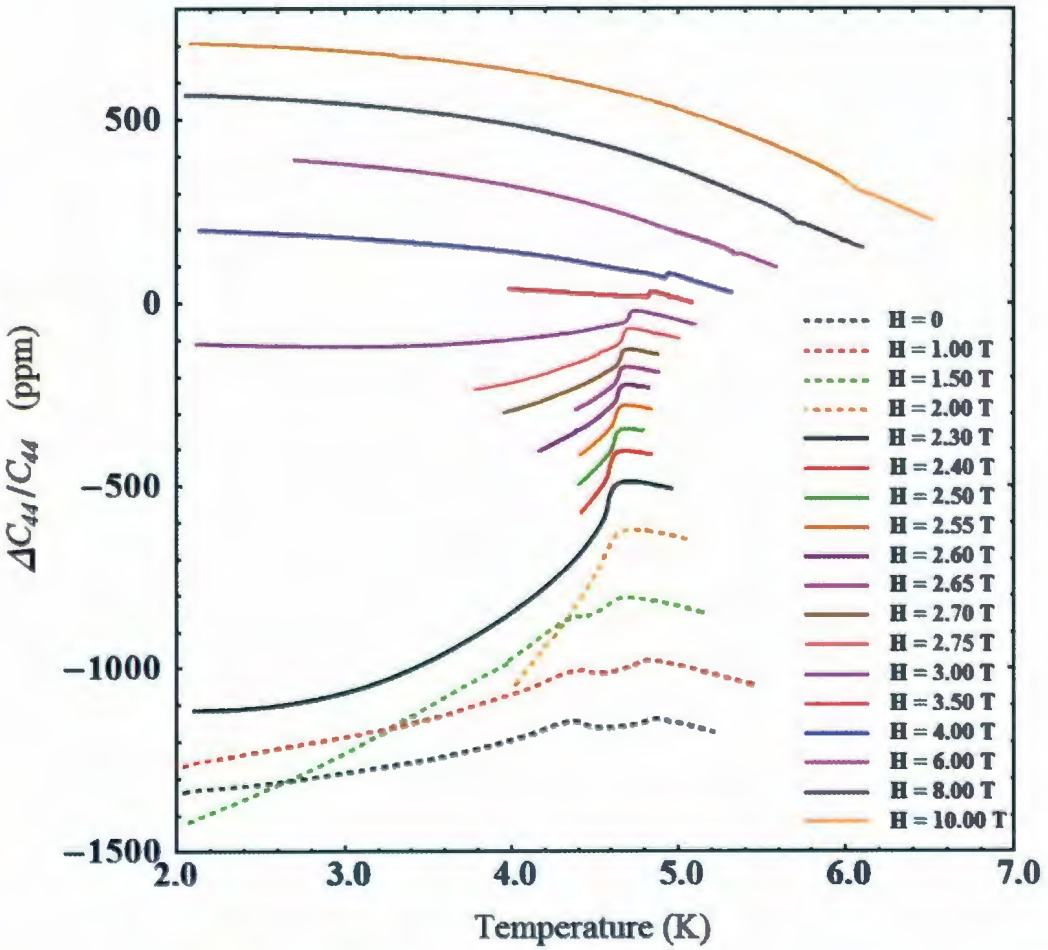


Figure 6.3: Relative variation of the elastic constant $C_{44}$ as a function of temperature at different magnetic fields. The continuous and broken lines represent data obtained above and below the multicritical field ($H_m = 2.29$ T), respectively.

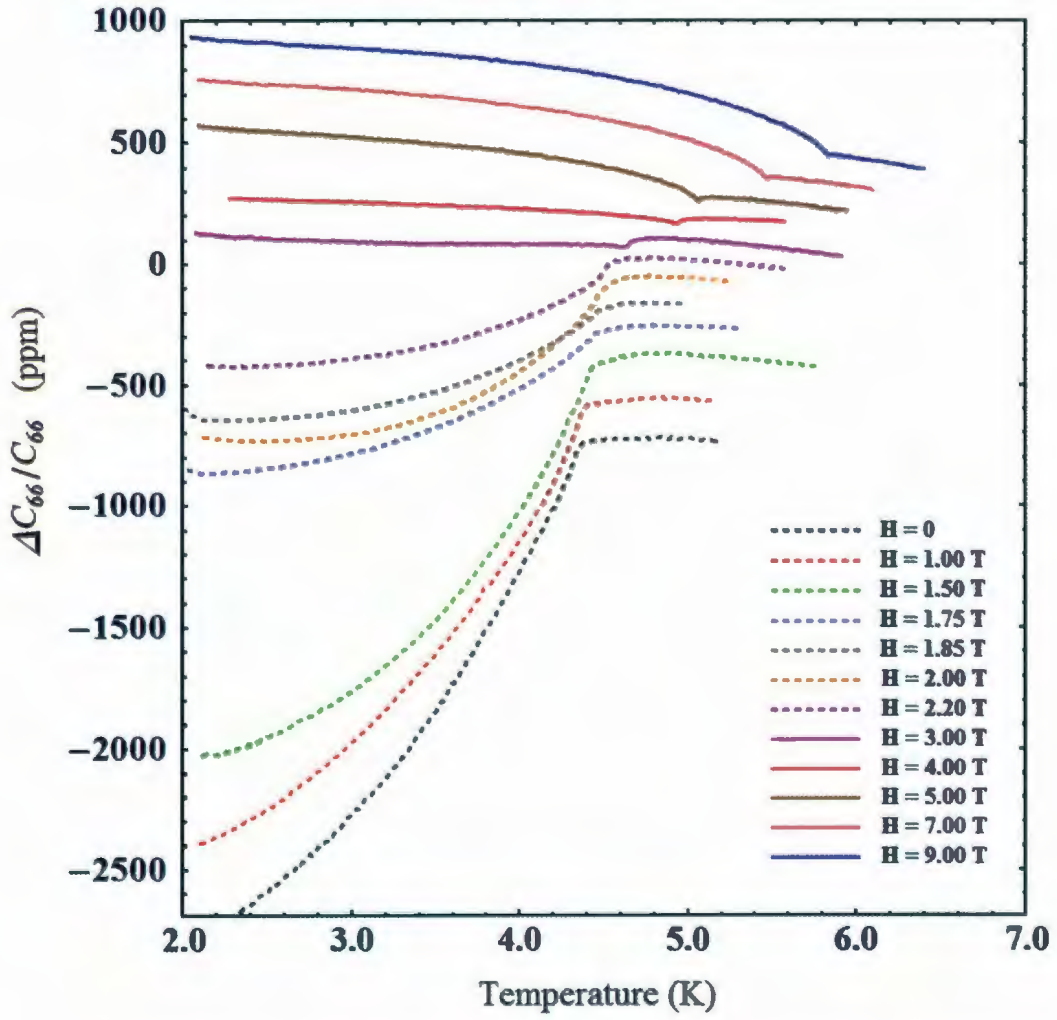


Figure 6.4: Relative variation of the elastic constant $C_{66}$ as a function of temperature at different magnetic fields. The continuous and broken lines represent data obtained above and below the multicritical field ($H_m = 2.29$ T), respectively.

The experimental results of the magnetic field dependence of $\frac{\Delta C_{33}}{C_{33}}$, $\frac{\Delta C_{44}}{C_{44}}$, and $\frac{\Delta C_{66}}{C_{66}}$ are presented in Fig. 6.5 - 6.7, respectively. The data obtained for temperatures lower than the multicritical temperature ($T_m = 4.50$ K) are presented by broken lines, while for higher temperatures continuous lines are used for clarity. Based on these experimental data, for $T < T_m$, a well defined minimum in the velocity observed at $H \approx 2.00$ T can be associated with a spin-flop phenomena. Meanwhile, for $T > T_m$, anomalies typical of a phase transition are observed at the boundary of the $120^{\circ}$ spin structure. For these experimentally obtained curves, the critical fields at different temperatures are located by finding the positions with the largest slopes.

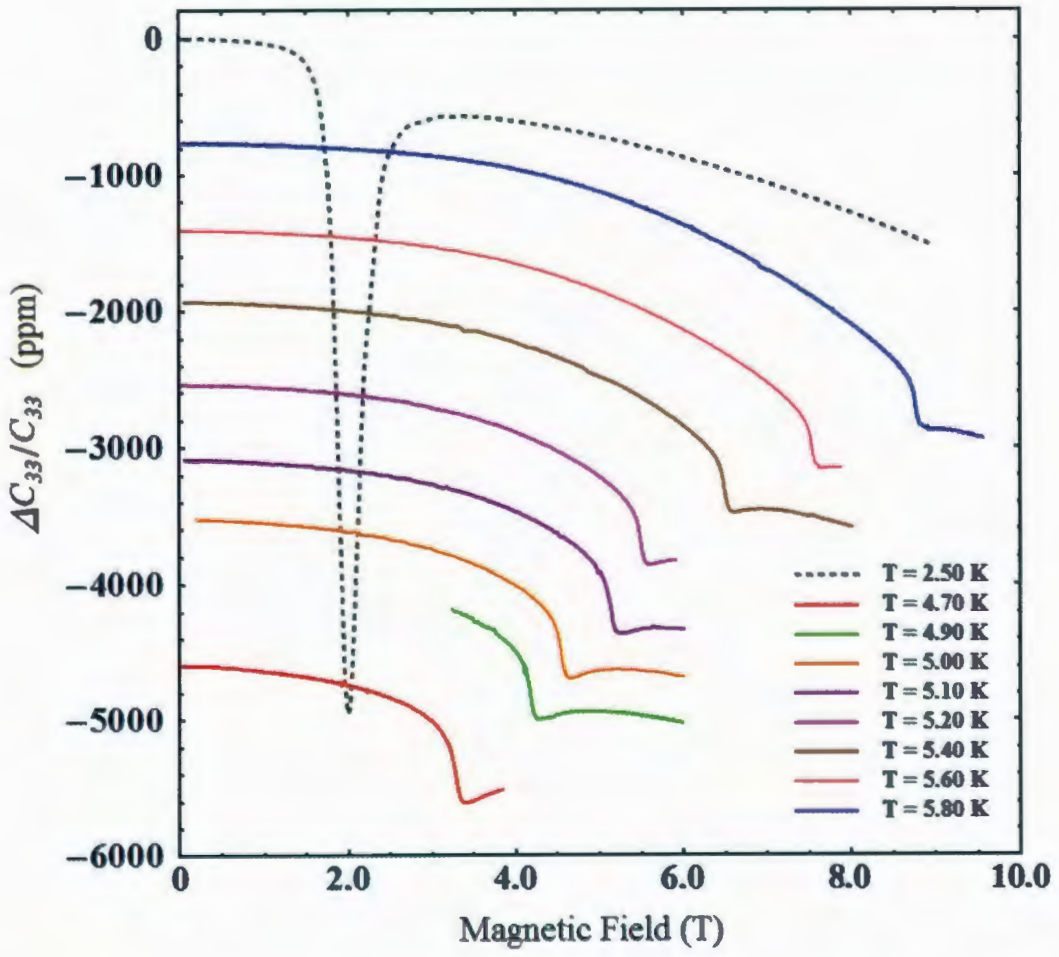


Figure 6.5: Relative variation of the elastic constant $C_{33}$ as a function of magnetic field. The continuous and broken lines represent data obtained above and below the multicritical point ($T_m = 4.50$ K), respectively.

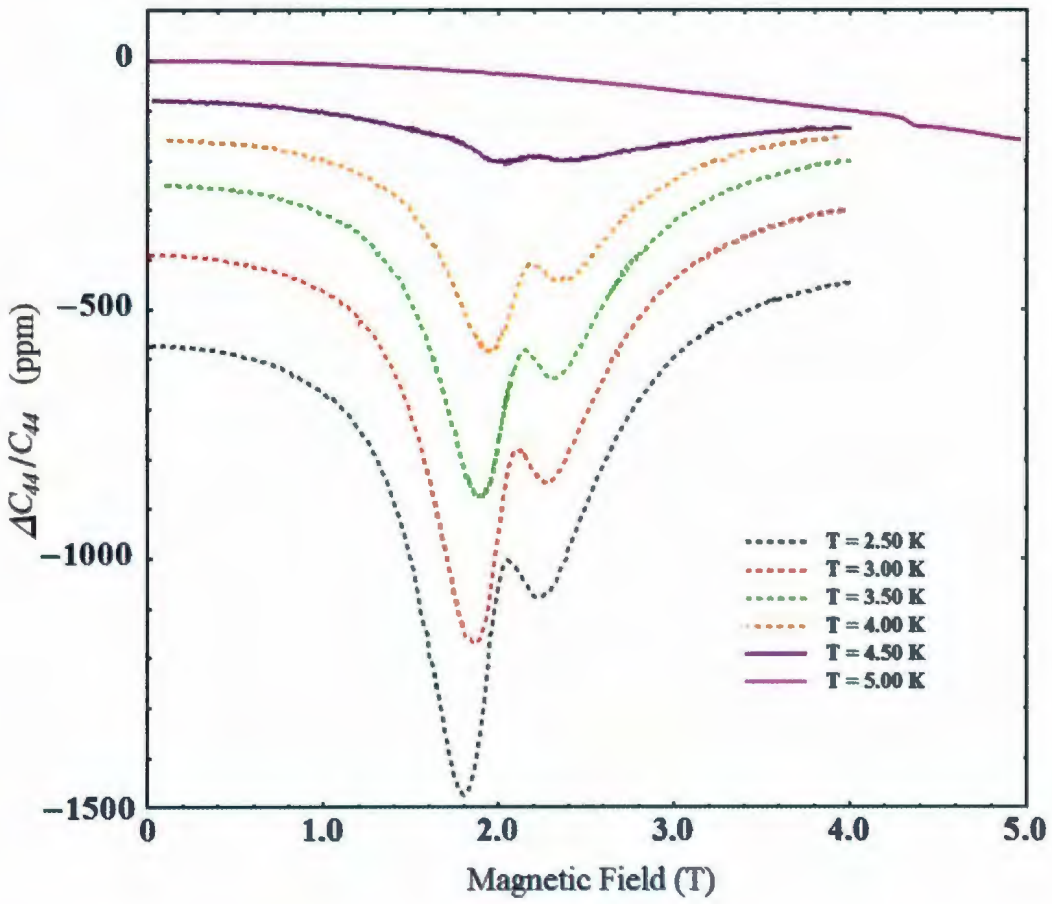


Figure 6.6: Relative variation of the elastic constant $C_{44}$ as a function of magnetic field. The continuous and broken lines represent data obtained above and below the multicritical point ($T_m = 4.50$ K), respectively.

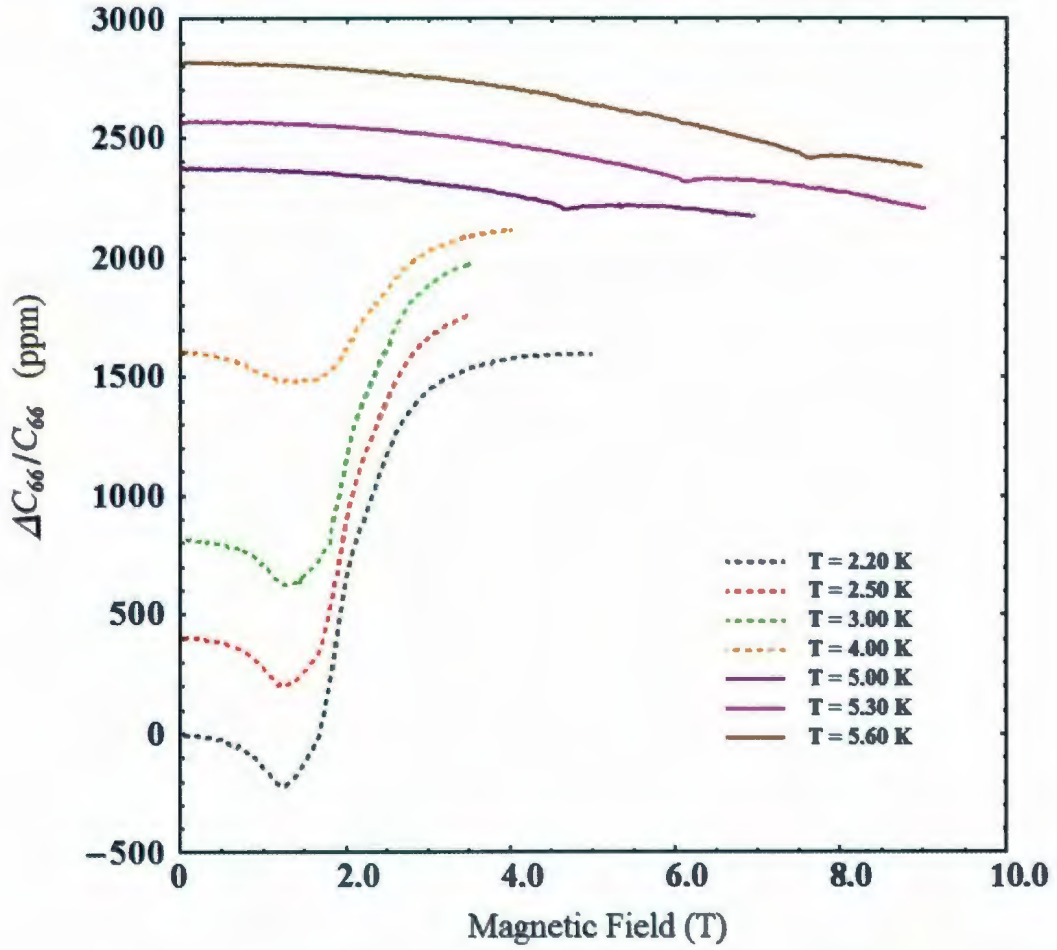


Figure 6.7: Relative variation of the elastic constant $C_{66}$ as a function of magnetic field. The continuous and broken lines represent data obtained above and below the multicritical point ($T_m = 4.50$ K), respectively.

## 6.3 Experimental magnetic phase diagram of $CsNiCl_3$

The temperature and magnetic field dependence of $\frac{\Delta C_{33}}{C_{33}}$, $\frac{\Delta C_{44}}{C_{44}}$, and $\frac{\Delta C_{66}}{C_{66}}$ have been used to derive the low temperature magnetic phase diagram of $CsNiCl_3$ shown in Fig. 6.8. These data are consistent with results obtained by other groups[4].

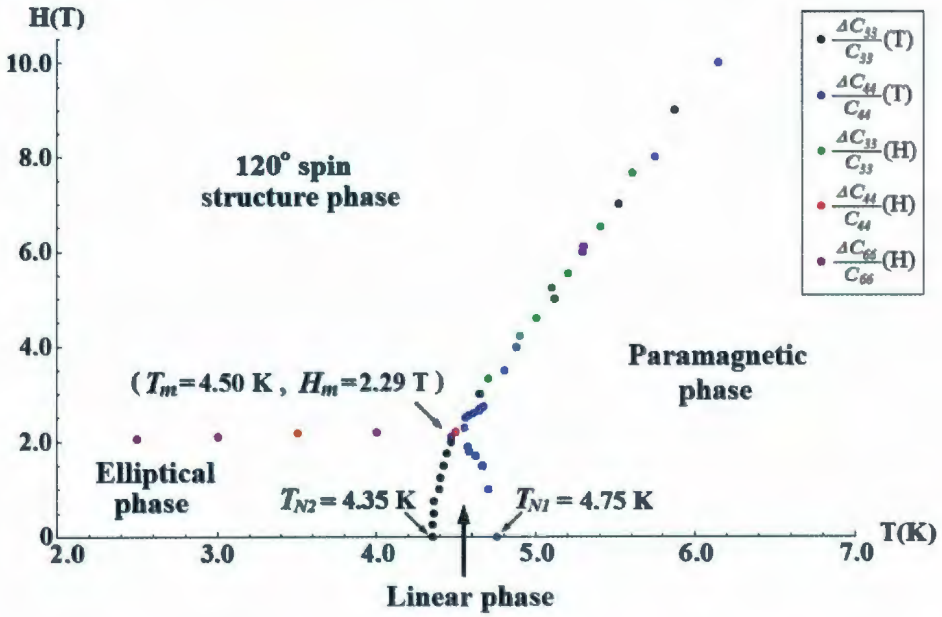


Figure 6.8: Experimental magnetic phase diagram of $CsNiCl_3$ for H//c derived from the sound velocity measurements. Different colors are used to illustrate the source of data.

# Chapter 7

# Landau theory for phase transition

Landau theory is a phenomenological model that describes phase transitions without giving any information about the microscopic causes of the transition[58]. The explanatory power of the theory is to establish the overall consistency of the global characteristics of the transition (space symmetry and structural changes etc...) with experimental results of various relevant macroscopic quantities such as thermal expansion, dielectric properties, and elastic constants. The most important concepts in Landau theory are the order parameter and the free energy. The free energy, which is a function of the order parameters, is successfully used to describe second-order phase transitions and most first-order phase transitions.

## 7.1 Order parameters and free energy

To put it simply, the order parameter is a variable used to describe the degree of order for temperatures lower than the transition temperature, also referred as the critical temperature, $T_c$. In a continuous phase transition the order parameter goes continuously to zero as the critical temperature is approached from below. Different

phases have their own characteristic order parameter. The usual mean-field Landau free-energy is expressed as a Taylor expansion in powers of the order parameter which characterizes a specific phase[11]. Moreover, this free energy must be invariant under the symmetry transformations associated with the high-temperature phase. In our case, as the spin polarization $S$ is chosen as the order parameter, the free energy must be invariant under the inversion and time-reversal symmetry operation. To satisfy these invariant requirements, only even powers are allowed in the Landau free-energy. Expanded to a sixth order in $S$, the Landau free-energy for isotropic systems can be constructed as

$$F_L = \frac{A}{2}S^2 + \frac{B}{4}S^4 + \frac{C}{6}S^6. \tag{7.1}$$

In a conventional Landau free-energy, $A$ is temperature dependent and defined as

$$A = a(T - T_0), \tag{7.2}$$

where $a > 0$.

## 7.2 The second-order phase transition

In general, the second-order phase transitions are successfully described with the first two terms of Eq. 7.1, hence,

$$F_L = \frac{A}{2}S^2 + \frac{B}{4}S^4. \tag{7.3}$$

Given that $A = a(T - T_0)$, the coefficient $B$ must be positive in order to have a minimum in the free energy. Then the equation of state can be derived as

$$\frac{\partial F_L}{\partial S} = S(A + BS^2) = 0, \tag{7.4}$$

which has two solutions:

$$S = 0, \tag{7.5}$$

and

$$S = \sqrt{-\frac{A}{B}} = \sqrt{\frac{-a(T - T_0)}{B}}. \tag{7.6}$$

For the paramagnetic phase, where $S = 0$, the stability condition requires that

$$\frac{\partial^2 F_L}{\partial S^2} = A = a(T - T_0) \geqslant 0. \tag{7.7}$$

This indicates that $S = 0$ for the temperature region with $T \geqslant T_0$ and accordingly that the phase transition corresponds to $T_c = T_0$. For $S \neq 0$, we have

$$\frac{\partial^2 F_L}{\partial S^2} = A + 3BS^2 \geqslant 0. \tag{7.8}$$

Inserting $S$ from Eq. 7.6, we obtain

$$\frac{\partial^2 F_L}{\partial S^2} = -2A = -2a(T - T_c) \geqslant 0. \tag{7.9}$$

This can be satisfied as long as $T \leqslant T_c$.

$F_L$ as function of $S$ described by Eq. 7.3 is shown in Fig. 7.1. Here the solid lines represent the stable states for $T > T_c$ and $T < T_c$, while the dashed line represents the free energy at $T = T_c$. According to Fig. 7.1, for $T \geqslant T_c$, $F_L$ is stable at $S = 0$, however when $T < T_c$, the minimum in the free energy $F_L$ is observed at $S \neq 0$. The temperature dependence of the order parameter, given by Eq. 7.6, is illustrated in Fig. 7.2. As shown, the magnitude of the order parameter changes continuously at the transition temperature. This denotes a second-order phase transition or continuous phase transition. In general, the temperature dependence of the order parameter $S$ for the ordered phase can be described in terms of a critical exponent $\beta$ as

$$S \propto \tau^{\beta}, \tag{7.10}$$

where $\tau$ is the reduced temperature, $\tau = 1 - \frac{T}{T_c}$. Thus, according to the Landau theory, the mean-field value of the critical exponent is $\beta = 0.5$.

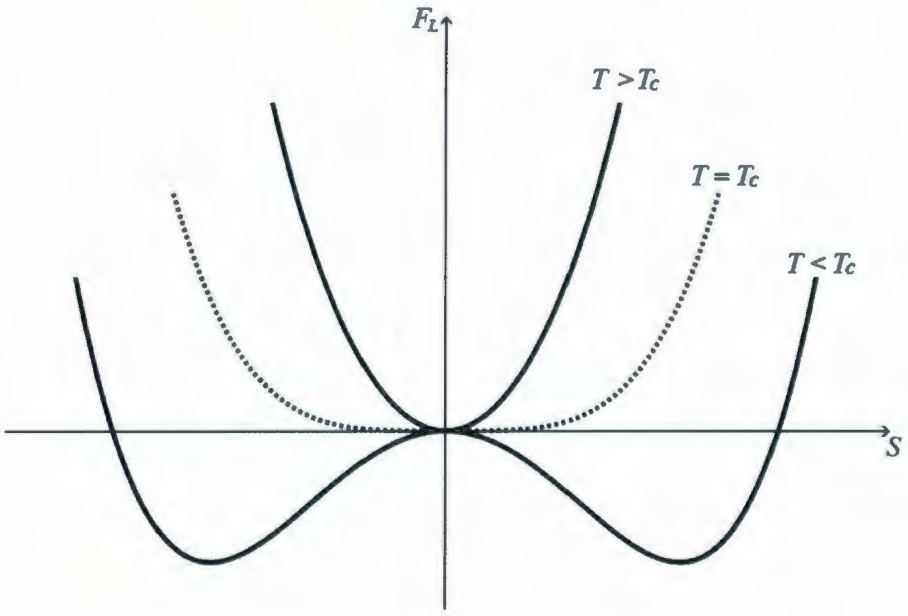


Figure 7.1: Landau free-energy as function of the order parameter for a second-order phase transition.

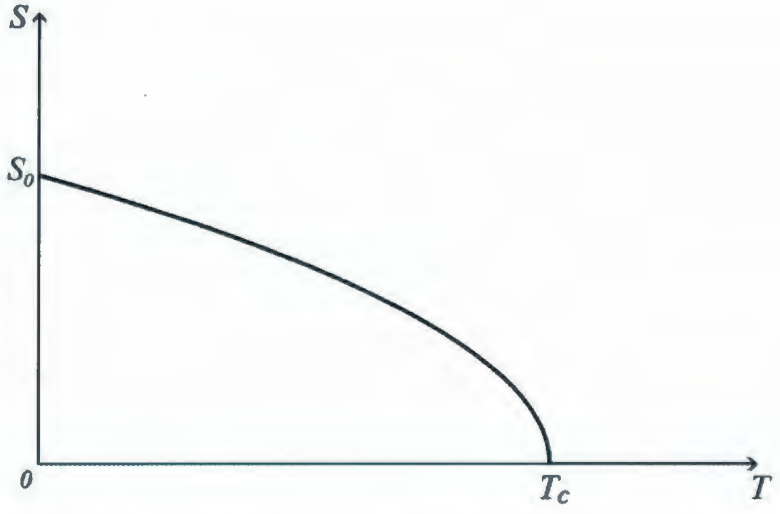


Figure 7.2: Order parameter as function of temperature for a second-order phase transition.

As mentioned in Chapter 3 (see Fig.3.2), the criticality for $CsNiCl_3$ along the phase boundaries associated with $T_{N1}$ and $T_{N2}$ is predicted to belong to the $XY$ universal class and the multicritical point is expected to belong to the chiral Heisenberg universality class[16]. Therefore, the expected values of $\beta$ at low magnetic fields should be 0.346 (see Table 1.1). For the high magnetic field phase transition, according to Kawamura[13]–[16], the value of the critical exponent $\beta$ should correspond to that of the chiral $XY$ universal class as $\beta = 0.25$. However, if the true nature of this phase transition is weakly first-order, there is no critical exponent associated with the phase transition.

## 7.3 The first-order phase transition

To describe a first-order phase transition, the sixth order term is taken into account and the Landau free-energy can be written as

$$F_L = \frac{A}{2}S^2 + \frac{B}{4}S^4 + \frac{C}{6}S^6. \tag{7.11}$$

Here $A$ is also defined as

$$A = a(T - T_0). \tag{7.12}$$

In order to have a minimum in $F_L$, we must set $B < 0$ and $C > 0$.

The relation between $F_L$ and $S$ in different temperature regions is illustrated in Fig. 7.3. As shown in Fig. 7.3, when $T \geqslant T_2$ (curves 1 and 2), $F_L$ is stable at $S = 0$. As the temperature is decreased, $F_L$ is still stabilized at the local minimum $S = 0$ until temperature reaches $T_c$. This situation is caused by the potential barrier between both local minimums when $T_c < T < T_2$ (curves 3, 4 and 5). Only when the potential barrier disappears, can the stable state change to the other local minimum where $S \neq 0$, minimizing the energy at the same time (curves 6 and 7). The same

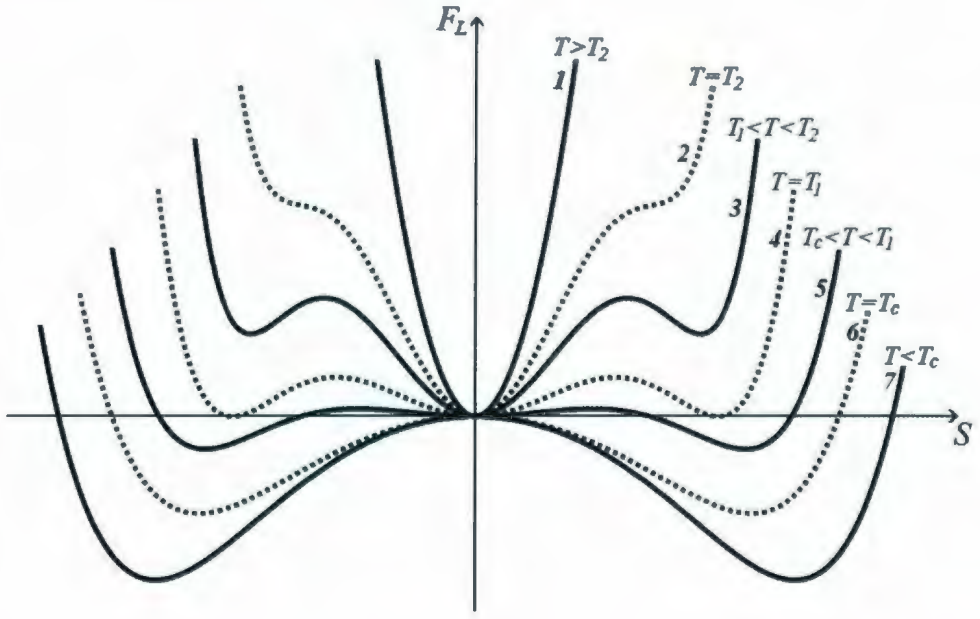


Figure 7.3: Landau free-energy as function of the order parameter for a first-order phase transition.

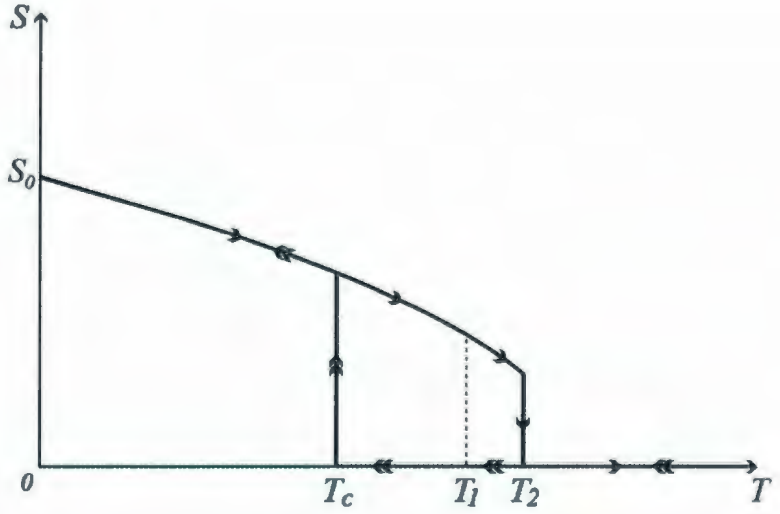


Figure 7.4: Order parameter as function of temperature for a first-order phase transition.

process happens when we increase the temperature. When $T \leqslant T_c$ (curve 6 and 7), $F_L$ is stable at the local minimum where $S \neq 0$. This state doesn't change until the temperature reaches $T_2$, where the potential barrier disappears. At $T = T_2$ (curve 2), $F_L$ slips back to the other stable state and $S$ suddenly changes back to zero. Based on Fig. 7.3, the behavior of $S$ as function of temperature for the first-order phase transition is summarized in Fig. 7.4. We notice that the phase transition happens at different critical temperatures depending whether the temperature increases or decreases. This phenomena is defined as hysteresis. Moreover, at the phase boundary $S$ changes suddenly between zero and nonzero value, which, together with the hysteresis, characterizes the first-order phase transition.

To determine $T_c$, $T_1$ and $T_2$, we need to start from the equation of state $\frac{\partial F_L}{\partial S} = 0$ and the stability condition $\frac{\partial^2 F_L}{\partial S^2} \geqslant 0$. To meet the requirement imposed by $\frac{\partial F_L}{\partial S} = 0$, we obtain $S = 0$ or $A + BS^2 + CS^4 = 0$. The solution with $S = 0$ stands for the paramagnetic phase, while $A + BS^2 + CS^4 = 0$ represents the solution for the ordered phase. Solving for $S^2$, we obtain

$$S^2 = \frac{-B \pm \sqrt{B^2 - 4AC}}{2C}, \tag{7.13}$$

in the ordered phase. Given that $A$ is a temperature dependent coefficient, we need to consider different cases.

(1) $B^2 - 4AC < 0$

In this case, $A > \frac{B^2}{4C}$. Given that $A = a(T - T_0)$, we obtain that

$$T > \frac{B^2}{4aC} + T_0. \tag{7.14}$$

When Eq. 7.14 is satisfied, there is no solution for Eq. 7.13 and $F_L$ can only be minimized at $S = 0$. This again describes the paramagnetic phase where $\frac{\partial^2 F_L}{\partial S^2} \geqslant 0$ is also satisfied.

(2) $B^2 - 4AC = 0$

If $B^2 - 4AC = 0$, we have

$$T_2 = \frac{B^2}{4aC} + T_0 \tag{7.15}$$

and

$$S^2(T_2) = \frac{-B}{2C}. \tag{7.16}$$

This describes the situation of curve 2.

(3) $T = T_c$

The critical temperature $T_c$ can be obtained using that

$$\left.\frac{\partial^2 F_L}{\partial S^2}\right|_{S=0} = A = a(T_c - T_0) = 0 \tag{7.17}$$

showing that

$$T_c = T_0. \tag{7.18}$$

(4) $T = T_1$

To determine $T_1$, as shown by curve 4, we need to solve both

$$F_L = \frac{A}{2}S^2 + \frac{B}{4}S^4 + \frac{C}{6}S^6 = 0 \tag{7.19}$$

and

$$\frac{\partial F_L}{\partial S} = A + BS^2 + CS^4 = 0. \tag{7.20}$$

Then $T_1 = \frac{3B^2}{16aC} + T_c$ is obtained.

# Chapter 8

# Landau Model for $CsNiCl_3$

At low temperatures $CsNiCl_3$ has a very rich phase diagram associated with different spin configurations. In other words, with the variation of temperature and magnetic field, the symmetry of the system changes. The problem we are facing is that we need a theoretical model that accounts for the observed symmetry change and the measured thermodynamics properties of $CsNiCl_3$. As discussed in Chapter 1, a solution to this problem can be obtained by using a Landau type model, which expresses the behavior of free energy in terms of thermodynamic variables in the vicinity of a critical point[36]. As shown by Plumer et al.[11],[30],[31],[57]–[62], Landau models have been used successfully to describe the magnetic properties of $ABX_3$ systems. In particular, the magnetic phase diagram of $CsNiCl_3$ is well accounted for by the Landau free-energy derived by Plumer et al.[11].

## 8.1 Landau free-energy and order parameters for $CsNiCl_3$

In this section, the derivation of Landau free-energy for $CsNiCl_3$, based on Plumer's work[11], is reproduced for convenience. Based on this free energy, we show how the magnetic phase diagram of $CsNiCl_3$ can be accounted for using only a few experimental critical temperatures and magnetic fields. In order to describe the temperature and magnetic field dependence of the phase boundaries, the temperature and magnetic field dependence of the magnetization $m_z$ is also needed.

### 8.1.1 Invariant terms and the Hamiltonian

When a phase transition happens, the symmetry of the system normally changes[58]. If the symmetry properties of the high and low temperature phases belong to the groups $G_0$ and $G$, respectively, the group theory indicates that $G$ must be a subgroup of $G_0$ in the case of a continuous phase transition. Thus, if a system remains invariant under the symmetry operations associated with $G_0$, it will automatically be invariant with respect to any operations belonging to $G$. Accordingly, we can employ the group $G_0$ to specify the form of the free energy, which must be invariant under all symmetry properties associated with that group[22],[58].

For example, most hexagonal $ABX_3$ compounds belong to the symmetry group $P6_3/mmc$, including 24 symmetry operations[63]. However, as all these operations can be obtained using the generators, $C_{6z}$ (6-fold rotation with respect to z-axis), $C_{2y}$ (2-fold rotation with respect to y-axis), and $I$ (inversion), it is sufficient to consider these three operations in order to derive the invariant form of the free energy. As shown in the published work of Plumer et al.[11], the form of the phenomenological

Landau free-energy of $ABX_3$ systems can be determined by formulating the relevant microscopic Hamiltonian. The Hamiltonian for two interacting spins $s_a$ and $s_b$ is

$$\mathcal{H} = \sum_{ab} J_{ab} \mathbf{s}_a \mathbf{s}_b, \qquad a, b = x, y, z, \tag{8.1}$$

where $J_{ab}$ is the exchange coefficient. This Hamiltonian must be invariant with respect to inversion $I$, time-reversal, $C_{6z}$, and $C_{2y}$ operations. Under these symmetry operations, the element of the second-rank tensor $J$ transforms as

$$J'_{ij} = \alpha_i^k \alpha_j^l J_{kl}. \tag{8.2}$$

where $\alpha_i^k$ and $\alpha_j^l$ are the components of the $3 \times 3$ $\alpha$-matrix

$$\alpha = \begin{pmatrix} \alpha_1^1 & \alpha_1^2 & \alpha_1^3 \\ \alpha_2^1 & \alpha_2^2 & \alpha_2^3 \\ \alpha_3^1 & \alpha_3^2 & \alpha_3^3 \end{pmatrix}. \tag{8.3}$$

For crystals with a hexagonal group symmetry, the $\alpha$-matrices for the generators are

$$\alpha_I = \begin{pmatrix} -1 & 0 & 0 \\ 0 & -1 & 0 \\ 0 & 0 & -1 \end{pmatrix}, \quad \alpha_{6z} = \begin{pmatrix} \frac{1}{2} & \frac{\sqrt{3}}{2} & 0 \\ -\frac{\sqrt{3}}{2} & \frac{1}{2} & 0 \\ 0 & 0 & 1 \end{pmatrix}, \quad \alpha_{2y} = \begin{pmatrix} -1 & 0 & 0 \\ 0 & 1 & 0 \\ 0 & 0 & -1 \end{pmatrix}. \tag{8.4}$$

As mentioned previously, the tensor $J$ must be invariant under the transformations associated with the generators, leading to $J'_{ij} = J_{ij}$. Thus, the possible terms reduce to

$$J_{ab} = \begin{pmatrix} J_{xx} & 0 & 0 \\ 0 & J_{xx} & 0 \\ 0 & 0 & J_{zz} \end{pmatrix}, \tag{8.5}$$

which indicates that the Hamiltonian for two interacting spins for crystals with a hexagonal structure can be written in terms of two independent exchange coefficients

as

$$\mathcal{H} = J_{xx}(s_x s_x + s_y s_y) + J_{zz} s_z s_z. \tag{8.6}$$

Expressed in terms of $\mathbf{s} \cdot \mathbf{s}$ and $s_z^2$, Eq. 8.6 can be represented as

$$\mathcal{H} = J_{xx}\mathbf{s} \cdot \mathbf{s} + (J_{zz} - J_{xx}) s_z^2, \tag{8.7}$$

where $J_{xx}$ stands for the isotropic exchange coefficient, while $D = (J_{zz} - J_{xx})$ can be treated as an anisotropic exchange contribution. Based on Eq. 8.7, the Hamiltonian for magnetic compounds with a hexagonal symmetry can be rewritten as

$$\mathcal{H} = J_{\parallel} \sum_{i}^{chain} \mathbf{s}_i \cdot \mathbf{s}_{i+1} + J_{\perp} \sum_{i \neq j}^{plane} \mathbf{s}_i \cdot \mathbf{s}_j - D \sum_i (s_i^z)^2 - \mathbf{H} \cdot \sum_i \mathbf{s}_i. \tag{8.8}$$

The isotropic exchange between nearest neighbor magnetic ions is described by the first two terms where $J_{\parallel}$ is the exchange interaction along the c-direction while the basal plane interaction is accounted for by the exchange coefficient $J_{\perp}$. The anisotropy exchange of the system can be represented as $\sum_{i \neq j}(J_{zz} - J_{xx}) s_{iz} s_{jz}$, however, if one consider the dominant contribution, where $i = j$, it reduces to the usual on-site case corresponding to the third term of Eq. 8.8, with $D$ being the single-ion anisotropy coefficient. Finally, the last term represents the usual Zeeman contribution associated with the application of an external magnetic field $\mathbf{H}$. As the spin configuration must minimize the energy, the sign and magnitude of $D$ determines the orientation of the spin relative to the crystal axes. The pure Heisenberg model is defined when $D = 0$ as no restriction on the spin orientation is imposed. If $D < 0$, to minimize the anisotropy energy, spins are confined to the basal plane and are described using $XY$ models. When $D > 0$, the anisotropy terms is supposed to be minimized by aligning the spins parallel to the c-direction, but in fact the spin configuration is determined by the competition between the first three terms of Eq. 8.8. The very large $D$ leads to an Ising model. For $CsNiCl_3$, based on the experimental results given in Chapter 3,

$\frac{J_\parallel}{J_\perp} \gg 1$ with $J_\parallel \gg D$, consequently $CsNiCl_3$ is considered to be a typical example of a quasi-one dimensional nearly isotropic Heisenberg antiferromagnet.

### 8.1.2 Landau free-energy

The derivation of the Landau free-energy in this section is based on Plumer's approach[11],[11] where the integral form of the Landau free-energy for $CsNiCl_3$ can be constructed to a fourth order in spin as

$$\begin{aligned} F[\boldsymbol{s}(\mathbf{r})] = & \int d\mathbf{r}_1 d\mathbf{r}_2 A(\boldsymbol{\tau}) \boldsymbol{s}(\mathbf{r}_1) \cdot \boldsymbol{s}(\mathbf{r}_2) \\ & + \frac{1}{2} \int d\mathbf{r}_1 d\mathbf{r}_2 d\mathbf{r}_3 d\mathbf{r}_4 B(\mathbf{r}_1, \mathbf{r}_2; \mathbf{r}_3, \mathbf{r}_4) \boldsymbol{s}(\mathbf{r}_1) \cdot \boldsymbol{s}(\mathbf{r}_2) \boldsymbol{s}(\mathbf{r}_3) \cdot \boldsymbol{s}(\mathbf{r}_4) \\ & + \frac{1}{2} D \int d\mathbf{r} [s_z(\mathbf{r})]^2 - \mathbf{H} \cdot \int d\mathbf{r} \boldsymbol{s}(\mathbf{r}), \end{aligned} \tag{8.9}$$

with $\boldsymbol{\tau}=\mathbf{r}_1-\mathbf{r}_2$ and $\mathbf{H}$ being the applied magnetic field. The first part of this equation, $\int d\mathbf{r}_1 d\mathbf{r}_2 A(\boldsymbol{\tau}) \boldsymbol{s}(\mathbf{r}_1) \cdot \boldsymbol{s}(\mathbf{r}_2)$, comes from the isotropic term of Eq. 8.8 while the third part, $\frac{1}{2} D \int d\mathbf{r} [s_z(\mathbf{r})]^2$, is the integral form of the anisotropy contribution. In $ABX_3$ systems, as the spins are localized on the lattice sites of $Ni^{2+}$, which is the magnetic ions, the local spin density can be defined as

$$\boldsymbol{s}(\mathbf{r}) = (V/N) \sum_{\mathbf{R}} \boldsymbol{\rho}(\mathbf{r}) \delta(\mathbf{r} - \mathbf{R}), \tag{8.10}$$

where $\mathbf{R}$ represents the lattice position of the magnetic ions. The non-local spin density $\boldsymbol{\rho}(\mathbf{r})$ characterizes the long range order of the system as

$$\boldsymbol{\rho}(\mathbf{r}) = \mathbf{m} + \mathbf{S} e^{i\mathbf{Q}\cdot\mathbf{r}} + \mathbf{S}^* e^{-i\mathbf{Q}\cdot\mathbf{r}}, \tag{8.11}$$

where $\mathbf{m}$ is the uniform magnetization induced by the field $\mathbf{H}$, while $\mathbf{S}$ and $\mathbf{Q}$ are the polarization and wave vector, respectively. Using this spin density expression,

Plumer et al.[11],[22] has shown that the Landau free-energy Eq. 8.9 is given by

$$\begin{aligned} F_L(S, S_z) = {} & A_Q S^2 - A_z |S_z|^2 + B_1 S^4 + \frac{1}{2} B_2 |\mathbf{S} \cdot \mathbf{S}|^2 \\ & + \frac{1}{2} \tilde{A}_0 m^2 - \frac{1}{2} A_{z0} m_z^2 + \frac{1}{4} B_3 m^4 + 2B_4 |\mathbf{m} \cdot \mathbf{S}|^2 + B_5 m^2 S^2 \\ & - \mathbf{m} \cdot \mathbf{H}, \end{aligned} \tag{8.12}$$

where $S^2 = \mathbf{S} \cdot \mathbf{S^*}$ and $A_Q$ depends on temperature as

$$A_Q = a(T - T_Q). \tag{8.13}$$

The polarization vector $\mathbf{S}$ can be written in terms of real vectors as

$$\mathbf{S} = \mathbf{S}_1 + i\mathbf{S}_2, \tag{8.14}$$

where the imaginary part is employed to describe the changes of angle between neighboring spins. Here, $\mathbf{S}_1$ and $\mathbf{S}_2$ are given by

$$\mathbf{S}_1 = S \cos\beta [\sin\theta \ \hat{\rho}_1 + \cos\theta \ \hat{z}]; \tag{8.15a}$$

$$\mathbf{S}_2 = S \sin\beta \ \hat{\rho}_2, \tag{8.15b}$$

where $\hat{\rho}_1$, $\hat{\rho}_2$ are unit orthogonal vectors lying in the basal plane, while $\hat{z}$ is along the c-axis. Together with Eq. 8.14 and 8.15, the Landau free-energy can be rewritten as

$$\begin{aligned} F_L(S, \beta, \theta) = {} & C_S S^2 - C_\theta S^2 \cos^2\theta + C_\beta S^2 \sin^2\beta + 2B_2 S^4 \sin^4\beta + \frac{1}{2} B S^4 \\ & + \frac{1}{2} A_0 m_z^2 + \frac{1}{4} B_3 m_z^4 - m_z H, \end{aligned} \tag{8.16}$$

where $C_S = A_Q + B_5 m_z^2$, $C_\theta = A_z - 2B_4 m_z^2$, $C_\beta = C_\theta \cos^2\theta - 2B_2 S^2$, and $A_0 = \tilde{A}_0 - A_{z0} \equiv a(T - T_0)$. Here $S$ and $\beta$ are zero field order parameters while $\theta$ characterizes the phase transition under an applied magnetic field. Notice that $S\sin\beta$ is the basal plane component of $S$, thus for convenience we define $S_\perp = S\sin\beta$ as the polarization perpendicular to c-axis. Meanwhile, we also define $\zeta = \cos\theta$ in order to characterize

the spin-flop phase transition observed under the magnetic field. Hence, using this notation the Landau free-energy, Eq. 8.16, can be rewritten as

$$F_L(S, S_\perp, \zeta) = (A_Q - A_z\zeta^2)S^2 + \frac{1}{2}BS^4 + A_z\zeta^2 S_\perp^2 + 2B_2 S_\perp^4 - 2B_2 S^2 S_\perp^2 + \frac{1}{2}A_0 m_z^2 + \frac{1}{4}B_3 m_z^4 + B_5 m_z^2 S^2 + 2B_4\zeta^2(S^2 - S_\perp^2)m_z^2 - m_z H. \quad (8.17)$$

All four phases in the phase diagram Fig.1.2(b) are associated with different values for these three order parameters $S$, $S_\perp$ and $\zeta$ as listed in Table 8.1. Given that

| Phase | $S$ | $S_\perp$ | $\zeta$ |
|---|---|---|---|
| Paramagnetic | 0 | 0 | 1 |
| Linear | $S$ | 0 | 1 |
| Elliptical | $S$ | $S_\perp$ | 1 |
| $120^\circ$ spin structure | $S$ | $S_\perp$ | 0 |

Table 8.1: Order parameters in different phases.

the order parameters are defined to describe the degree of order in a phase below its transition temperature, in the paramagnetic phase $S$ and $S_\perp$ must be set to zero. In the linear phase, we need a nonzero order parameter $S$ to describe the spin configuration. Furthermore, given that the spins are aligned along the c-direction, the basal plane component of the spin polarization, $S_\perp$, is still zero. With further decrease in temperature, spin canting appears with respect to c-axis in the elliptical phase. Thus, both $S$ and $S_\perp$ are nonzero. As the spin-flop phase transition happens due to the application of a magnetic field along the c-axis, the spins suddenly flip into the basal plane, with a small component along the c-axis. Therefore, in the $120^\circ$ spin structure, both $S$ and $S_\perp$ remain nonzero. Thus, the spin-flop phase transition is related to the

discontinuous change of the order parameter $\zeta$ from the value 1 in the low magnetic field phases to 0 in the 120° phase.

### 8.1.3 Temperature and magnetic field dependence of the order parameters and magnetization

One of the main ideas of the Landau theory is that there exist order parameters that minimize the energy. In other words, the first derivative of free energy $F_L$ with respect to the order parameter $S$ or $S_\perp$ should be zero. This also applies to $m_z$. In the following section, the temperature and magnetic field dependence of the order parameters are derived for each phase separately.

For clarity, the subscript "p", "l", "e", and "120" are used to identify the paramagnetic, linear, elliptical and 120° phase, respectively. Based on this Landau free-energy, the phase diagram of $CsNiCl_3$ is derived.

Paramagnetic phase

As discussed above, as $S$ and $S_\perp$ are set to zero, the Landau free-energy reduces to its simplest form

$$F_{L(p)} = \frac{1}{2}A_0 m_z^2 + \frac{1}{4}B_3 m_z^4 - m_z H, \tag{8.18}$$

and $m_z$ can be solved by minimizing $F_{L(p)}$ with respect to $m_z$. According to Eq. 8.18, we have

$$\frac{\partial F_{L(p)}}{\partial m_z} = -H + A_0 m_z + B_3 m_z^3 = 0. \tag{8.19}$$

Solving for $m_z$, we obtain

$$m_{zp}(A_0, H) = \frac{(2/3)^{\frac{1}{3}} A_0}{(9B_3^2 H + \sqrt{3}\sqrt{4A_0^3 B_3^3 + 27B_3^4 H^2})^{\frac{1}{3}}} + \frac{(9B_3^2 H + \sqrt{3}\sqrt{4A_0^3 B_3^3 + 27B_3^4 H^2})^{\frac{1}{3}}}{18^{\frac{1}{3}} B_3}, \tag{8.20}$$

where $A_0 = a(T - T_0)$ accounts for the temperature dependence. Because expressions for $m_z$ in ordered states are too long, we only show the actual solution of $m_z$ in the

paramagnetic phase.

Linear phase

In the linear phase, where $S_\perp = 0$ and $\zeta = 1$, the Landau free-energy can be rewritten in terms of $S$, $\zeta = 1$, and $m_z$ as

$$F_{L(l)} = (A_Q - A_z)S^2 + \frac{1}{2}BS^4 + \frac{1}{2}A_0 m_z^2 + \frac{1}{4}B_3 m_z^4 + (B_5 + 2B_4)m_z^2 S^2 - m_z H. \quad (8.21)$$

Thus, the temperature and magnetic field dependence of $S$ and $m_z$ can be determined according to Eq. 8.21 by solving

$$\frac{\partial F_{L(l)}}{\partial S} = A_Q - A_z + BS^2 + (2B_4 + B_5)m_z^2 = 0 \quad (8.22)$$

and

$$\frac{\partial F_{L(l)}}{\partial m_z} = -H + A_0 m_z + 2(2B_4 + B_5)S^2 m_z + B_3 m_z^3 = 0. \quad (8.23)$$

Solving Eq. 8.22, we obtain $S$ as

$$S_l(A_Q, m_{zl}) = \sqrt{\frac{-A_Q + A_z - (2B_4 + B_5)m_{zl}^2}{B}}, \quad (8.24)$$

where $A_Q = a(T - T_Q)$ accounts for the temperature contributions. With the help of Eq. 8.24, the order parameter $S$ in Eq. 8.23 is eliminated and then the temperature and magnetic field dependence of $m_z$ can be solved. As this analytical solution is long, we will refer to it as $m_{zl}$. Substituting $m_{zl}$ in Eq. 8.24, the temperature and magnetic field dependence of $S$ can be calculated. At zero magnetic field, as $S$ and $m_{zl}$ are both null at the paramagnetic-linear phase boundary, where the temperature is defined as $T_{N1}$. Hence, at $T = T_{N1}$ and $m_{zl} = 0$, based on Eq. 8.24,

$$S_l(T = T_{N1}, m_{zl} = 0) = \sqrt{\frac{-a(T_{N1} - T_Q) + A_z}{B}} = 0, \quad (8.25)$$

we obtain that

$$T_{N1} = \frac{A_z}{a} + T_Q. \quad (8.26)$$

Elliptical phase

In the elliptical phase, both $S$ and $S_\perp$ remain nonzero and $\zeta = 1$. Hence, the Landau free-energy is

$$F_{L(e)} = (A_Q - A_z)S^2 + \frac{1}{2}BS^4 + A_z S_\perp^2 + 2B_2 S_\perp^4 - 2B_2 S^2 S_\perp^2 + \frac{1}{2}A_0 m_z^2 + \frac{1}{4}B_3 m_z^4 + B_5 m_z^2 S^2 + 2B_4(S^2 - S_\perp^2)m_z^2 - m_z H. \quad (8.27)$$

The temperature and magnetic field dependence of $S$, $S_\perp$, and $m_z$ can be solved by minimizing $F_{L(e)}$ with respect to $S$, $S_\perp$, and $m_z$ using that

$$\frac{\partial F_{L(e)}}{\partial S} = 2(A_Q - A_z)S - 4B_2 S_\perp^2 S + 2(2B_4 + B_5)m_z^2 S + 2BS^3 = 0, \quad (8.28)$$

$$\frac{\partial F_{L(e)}}{\partial S_\perp} = 2A_z S_\perp - 4B_2 S^2 S_\perp - 4B_4 m_z^2 S_\perp + 8B_2 S_\perp^3 = 0, \quad (8.29)$$

and

$$\frac{\partial F_{L(e)}}{\partial m_z} = -H + A_0 m_z + 2(2B_4 + B_5)S^2 m_z - 4B_4 S_\perp^2 m_z + B_3 m_z^3 = 0. \quad (8.30)$$

Solving the first two equations simultaneously, we obtain

$$S_e(A_Q, m_{ze}) = \sqrt{\frac{-2A_Q + A_z - 2(B_4 + B_5)m_{ze}^2}{2(B - B_2)}} \quad (8.31)$$

and

$$S_{\perp e}(A_Q, m_{ze}) = \sqrt{\frac{-A_z(B - 2B_2) - 2A_Q B_2 + 2((B - B_2)B_4 - B_2(B_4 + B_5))m_{ze}^2}{4B_2(B - B_2)}}, \quad (8.32)$$

where $A_Q = a(T - T_Q)$ accounts for the temperature contributions. Here, $m_{ze}$ represents the temperature and magnetic field dependence of the magnetization in the elliptical phase. Considering that $S_\perp$ and $m_{ze}$ are zero at $T_{N2}$, we obtain

$$T_{N2} = \frac{A_z}{a} - \frac{A_z B}{2aB_2} + T_Q. \quad (8.33)$$

120° phase

In the 120° phase, $\zeta$ changes to 0 in order to describe the spin-flop phase transition. Therefore, the Landau free-energy in terms of $S$, $S_\perp$, and $m_z$ is

$$F_{L(120)} = A_Q S^2 + \frac{1}{2}BS^4 + 2B_2 S_\perp^4 - 2B_2 S^2 S_\perp^2 + \frac{1}{2}A_0 m_z^2 + \frac{1}{4}B_3 m_z^4 + B_5 m_z^2 S^2 - m_z H. \quad (8.34)$$

Using the same method, we have that

$$\frac{\partial F_{L(120)}}{\partial S} = 2A_Q S - 4B_2 S_\perp^2 S + 2B_5 m_z^2 S + 2BS^3 = 0, \quad (8.35)$$

$$\frac{\partial F_{L(120)}}{\partial S_\perp} = -4B_2 S^2 S_\perp + 8B_2 S_\perp^3 = 0, \quad (8.36)$$

and

$$\frac{\partial F_{L(120)}}{\partial m_z} = -H + A_0 m_z + 2B_5 S^2 m_z + B_3 m_z^3 = 0. \quad (8.37)$$

According to Eq. 8.36, we immediately obtain

$$S_{120}(A_Q, m_{z120}) = \sqrt{2} S_{\perp 120}(A_Q, m_{z120}), \quad (8.38)$$

while

$$S_{\perp 120}(A_Q, m_{z120}) = \sqrt{\frac{-A_Q - B_5 m_{z120}^2}{2(B - B_2)}}, \quad (8.39)$$

where $A_Q = a(T - T_Q)$ accounts for the temperature contributions.

With the help of all these solutions, the temperature and magnetic field dependence of the order parameters and the magnetization and the expressions for the phase boundaries can be obtained. The theoretical prediction of the phase diagram of $CsNiCl_3$ is shown in the following section.

## 8.2 Landau prediction of the phase diagram

To determine the phase diagram, we need to solve for the temperature dependence of the critical magnetic field. Therefore, we can use the fact that the magnetization $m_z$

must be continuous at the phase boundaries. For example, on the phase boundary between the paramagnetic phase and the linear phase, the order parameter $S = 0$ and the magnetization is continuous. We can set $S = 0$ in Eq. 8.22 and solve for $m_z$ which gives the temperature dependence of $m_z$ on this phase boundary as

$$m_{z(p-l)} = \sqrt{\frac{-A_Q + A_z}{2B_4 + B_5}}, \tag{8.40}$$

where $A_Q = a(T - T_Q)$ and "(p-l)" is used to indicate that this is the solution at the boundary between the paramagnetic and linear phase. Substituting $m_{z(p-l)}$ back into Eq. 8.23, we obtain the temperature dependence of the critical magnetic field $H$ on this phase boundary corresponding to

$$H_{(p-l)}(A_0, A_Q) = A_0\sqrt{\frac{-A_Q + A_z}{2B_4 + B_5}} + B_3(\frac{-A_Q + A_z}{2B_4 + B_5})^{\frac{3}{2}}. \tag{8.41}$$

Using the same method, the temperature dependence of the critical magnetic field at other phase boundaries are

$$\begin{aligned} H_{(l-e)}(A_0, A_Q) = {} & A_0\sqrt{\frac{A_z(B - 2B_2) + 2A_QB_2}{2(BB_4 - B_2(2B_4 + B_5))}} \\ & + \sqrt{\frac{A_z(B - 2B_2) + 2A_QB_2}{2(BB_4 - B_2(2B_4 + B_5))^3}}(A_Q(B_2B_3 - 2B_4B_5 - 4B_4^2) \\ & + A_z(BB_3 - 2B_2B_3 - 4B_4B_5 - 2B_5^2)), \end{aligned} \tag{8.42}$$

$$H_{(e-120)}(A_0, A_Q) = \frac{2\sqrt{A_z}A_0B_4 + A_zB_3}{2\sqrt{2}B_4^{\frac{3}{2}}} - \frac{\sqrt{2}A_zA_QB_5 + 2A_zB_5^2}{2\sqrt{2}B^{\frac{3}{2}}(B - B_2)}, \tag{8.43}$$

$$H_{(p-120)}(A_0, A_Q) = \sqrt{-\frac{A_Q}{B_5}}(A_0 - \frac{A_QB_3}{B_5}). \tag{8.44}$$

For the phase transitions associated with the $120^\circ$ spin configuration, even if the phase transition is first-order, for convenience, we consider the behavior of the order parameters to be continuous. This consideration is based on the fact that, in our case, the discontinuities are relatively small and can be ignored.

The temperature and magnetic field of the multicritical point are defined as $T_m$ and $H_m$. Based on the fact that all four phase transition lines intercept at this point, analytical solutions for $T_m$ and $H_m$ can be obtained using Eq. 8.41 - Eq. 8.44. To recapitulate, analytical solutions for all critical points are given by

$$T_{N1} = \frac{A_z}{a} + T_Q, \tag{8.45a}$$

$$T_{N2} = T_{N1} - \frac{A_z B}{2aB_2} = \frac{A_z}{a} - \frac{A_z B}{2aB_2} + T_Q, \tag{8.45b}$$

$$T_m = T_{N1} - \frac{A_z(2B_4 + B_5)}{2aB_4} = -\frac{A_z B_5}{2aB_4} + T_Q, \tag{8.45c}$$

$$H_m = \frac{\sqrt{\frac{A_z}{B_4}}(A_z(B_3 - B_5) + 2aB_4(T_Q - T_0))}{2\sqrt{2}B_4}. \tag{8.45d}$$

Consequently, the experimental critical points listed in Table 8.2 can be used to determine the values of the Landau model parameters. The value of $T_Q$ has been obtain by extrapolating the $H_{(p-120)}$ phase boundary down to zero field, according to our experimental data $T_Q = 4.20$ K. Numerical values of all Landau coefficients

| | |
|---|---|
| $T_Q$ | 4.20 K |
| $T_0$ | −34.80 K |
| $T_{N1}$ | 4.75 K |
| $T_{N2}$ | 4.35 K |
| $T_m$ | 4.50 K |
| $H_m$ | 2.29 T |
| $H_c(T_c = 6.14\text{ K})$ | 10.00 T |

Table 8.2: The experimental values of the critical points used to obtain the magnetic phase diagram.

| | |
|---|---|
| $a$ | 400 |
| $A_z/a$ | 0.55 |
| $B/a$ | 6.960 |
| $B_2/a$ | 4.785 |
| $B_3/a$ | 3.462 |
| $B_4/a$ | 0.169 |
| $B_5/a$ | $-0.185$ |

Table 8.3: Coefficients used to obtain the magnetic phase diagram of $CsNiCl_3$.

obtained here are given in Table 8.3. With these coefficients, the temperature and magnetic field dependence of the phase boundaries can be calculated using Eq. 8.41 - Eq. 8.44 in order to reproduce the magnetic phase diagram of $CsNiCl_3$. We compare in Fig. 8.1, the calculated phase diagram with our experimental phase diagram of $CsNiCl_3$ for a magnetic field applied along the c-direction. We notice that the obtained theoretical prediction reproduces well all four phase boundaries. The small departure close to the multicritical point ($T_m$, $H_m$) is due to the difficulty to pinpoint the experimental critical value in that range. This is principally associated with the fact that the amplitude of the anomaly on the velocity curves becomes very small. Finally, let us point out that the analytical results presented in this chapter are consistent with that of the work published by Plumer et al.[11].

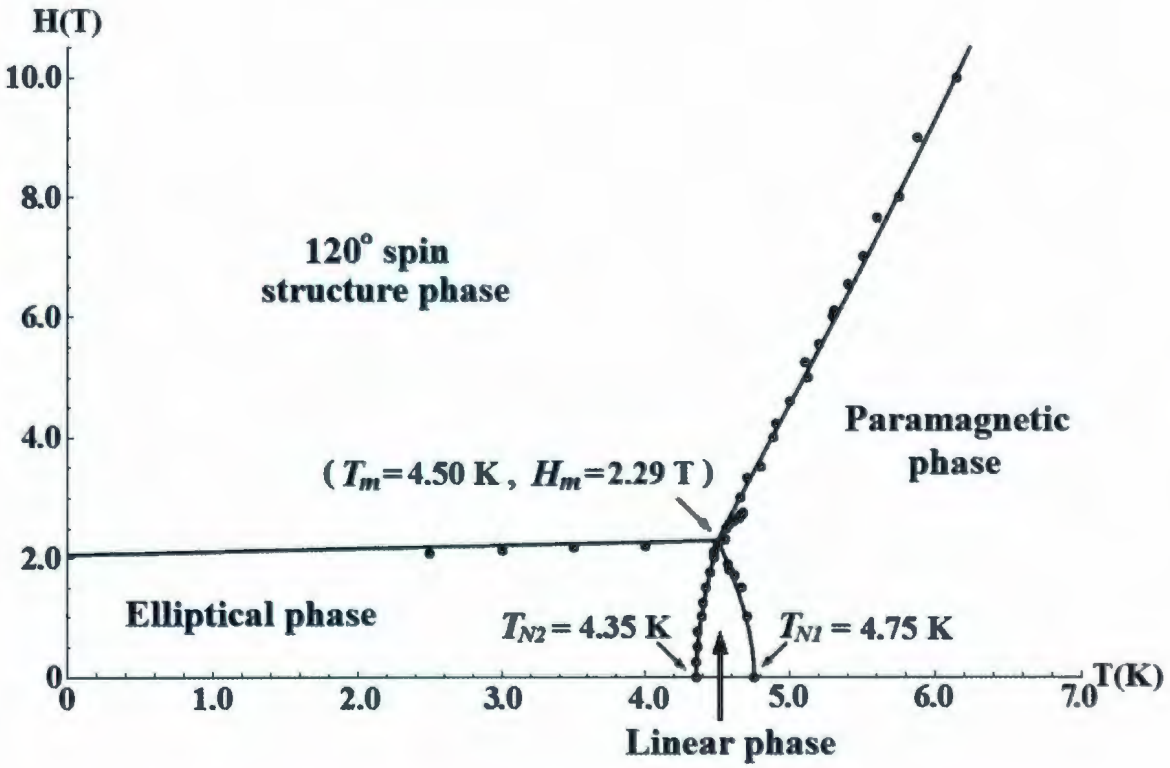


Figure 8.1: Magnetic phase diagram of $CsNiCl_3$ for H//c. Filled circles correspond to experimental data obtained from our ultrasonic velocity measurements, and the lines represent the results of the Landau theory.

# Chapter 9

# Total free energy

In our work, the total free energy is composed of the Landau free-energy, the elastic energy and the magnetoelastic coupling terms. The magnetoelastic coupling effect, which relates strains and the order parameters, is proved to be very useful in order to describe the magnetic properties and the elastic properties of quasi-one-dimensional antiferromagnet, especially for $CsNiCl_3$. Consequently, the total free energy needs to be expressed as

$$F_{total} = F_L(\eta) + F_{el}(e) + F_C(e, \eta), \tag{9.1}$$

where $\eta$ represents the order parameter and $e$ stands for strains.

In this chapter, we will present the derivation of the total free energy which takes into account the Landau free-energy $F_L(\eta)$ as derived in Chapter 8, the elastic energy $F_{el}(e)$, and the magnetoelastic energy $F_C(e, \eta)$. From this model, relations between elastic constants, strains and order parameters are obtained. Although Landau theory is a mean-field theoretical model, these phenomenological relations can still be used in order to analyze experimental data, where a non-mean-field critical exponent $\beta$ is assumed for the temperature dependence of the order parameter.

## 9.1 Elastic energy of $CsNiCl_3$

The second part of the total energy Eq. 9.1 is the elastic energy which is caused by small elastic distortions. According to the Hooke's law, using the Voigt notation ($\alpha, \beta = 1, 2, 3, 4, 5, 6$), the elastic energy can be written as

$$U = \frac{1}{2} C_{\alpha\beta} e_\alpha e_\beta, \tag{9.2}$$

where $C_{\alpha\beta}$ represents the elastic constants while $e_\alpha$ stands for the strains. The strain components $e_\alpha$ are related to their cartesian representation using the correspondences

$$\begin{aligned} &e_1 \leftrightarrow e_{1,1} && e_2 \leftrightarrow e_{2,2} && e_3 \leftrightarrow e_{3,3} \\ &e_4 \leftrightarrow 2e_{2,3} && e_5 \leftrightarrow 2e_{1,3} && e_6 \leftrightarrow 2e_{1,2}. \end{aligned} \tag{9.3}$$

Thus, based on the 5 independent elastic constants as shown in Eq. 5.35, the elastic energy for $CsNiCl_3$ can be expressed as

$$\begin{aligned} F_{el}(e) = &\frac{1}{2} C_{11}(e_{1,1}^2 + e_{2,2}^2) + \frac{1}{2} C_{33} e_{3,3}^2 \\ &+ C_{12} e_{1,1} e_{2,2} + C_{13}(e_{1,1} + e_{2,2}) e_{3,3} + 2C_{44}(e_{1,3}^2 + e_{2,3}^2) + 2C_{66} e_{1,2}^2. \end{aligned} \tag{9.4}$$

## 9.2 Magnetoelastic coupling terms

Magnetoelastic contributions to the free energy account for uniform strain-spin coupling. In our study[59], we restrict our discussion on the linear-quadratic (l-q) and quadratic-quadratic (q-q) terms. All these terms must also be invariant with respect to hexagonal symmetry operations. Using cartesian notation, we can express the magnetoelastic coupling terms as

$$F_C = \sum_{i,j,k,l} K_{i,j,k,l} e_{i,j} S_k S_l + \sum_{m,n,p,q,r,s} V_{m,n,p,q,r,s} e_{m,n} e_{p,q} S_r S_s, \tag{9.5}$$

where $K_{i,j,k,l}$ and $V_{m,n,p,q,r,s}$ are elements of the tensors $K$ and $V$ representing coefficients for l-q and q-q coupling. The invariant elements are determined by applying the main symmetry operations associated with the generators of hexagonal group, $C_{2y}$, $C_{6z}$, and inversion $I$ on the tensors.

### 9.2.1 l-q magnetoelastic coupling terms

For l-q terms, given that $S_k S_l = S_l S_k$ and $e_{i,j} = e_{j,i}$, the 4th-order tensor can be written as a 2nd-order tensor. Using the symmetry operations, the invariant elements correspond to

$$K = \begin{pmatrix} K_{1,1,1,1} & K_{1,1,2,2} & K_{1,1,3,3} & 0 & 0 & 0 \\ K_{1,1,2,2} & K_{1,1,1,1} & K_{1,1,3,3} & 0 & 0 & 0 \\ K_{3,3,1,1} & K_{3,3,1,1} & K_{3,3,3,3} & 0 & 0 & 0 \\ 0 & 0 & 0 & K_{2,3,2,3} & 0 & 0 \\ 0 & 0 & 0 & 0 & K_{2,3,2,3} & 0 \\ 0 & 0 & 0 & 0 & 0 & K_{1,2,1,2} \end{pmatrix}, \tag{9.6}$$

where $K_{1,2,1,2} = \frac{1}{2}(K_{1,1,1,1} - K_{1,1,2,2})$. Thus, the l-q coupling terms can be expressed as

$$\begin{aligned} F_{C(l-q)} = & K_{1,1,1,1}(e_{1,1}S_xS_x + e_{2,2}S_yS_y + 2e_{1,2}S_xS_y) \\ & + K_{1,1,2,2}(e_{1,1}S_yS_y + e_{2,2}S_xS_x - 2e_{1,2}S_xS_y) \\ & + K_{1,1,3,3}(e_{1,1} + e_{2,2})S_zS_z \\ & + K_{3,3,1,1}e_{3,3}(S_xS_x + S_yS_y) \\ & + K_{3,3,3,3}e_{3,3}S_zS_z \\ & + K_{1,3,1,3}(4e_{1,3}S_xS_z + 4e_{2,3}S_yS_z). \end{aligned} \tag{9.7}$$

For uniform deformations, these terms can be evaluated using the integral form as

$$\sum_{i,j,k,l} K_{i,j,k,l} e_{i,j} S_k S_l = \int d\mathbf{r}_1 \int d\mathbf{r}_2 \int d\mathbf{r}_3 K_{i,j,k,l}(\mathbf{r}_1; \mathbf{r}_2 - \mathbf{r}_3) e_{i,j}(\mathbf{r}_1) S_k(\mathbf{r}_2) S_l(\mathbf{r}_3). \tag{9.8}$$

For example, terms associated with $K_{1,1,1,1}$ can be represented as

$$K_{1,1,1,1}(e_{1,1} S_x S_x + e_{2,2} S_y S_y + 2e_{1,2} S_x S_y), \tag{9.9}$$

and the integral form that relates to $e_{1,1} S_x S_x$ is

$$\int d\mathbf{r}_1 \int d\mathbf{r}_2 \int d\mathbf{r}_3 K_{1,1,1,1}(\mathbf{r}_1; \mathbf{r}_2 - \mathbf{r}_3) e_{1,1}(\mathbf{r}_1) S_x(\mathbf{r}_2) S_x(\mathbf{r}_3). \tag{9.10}$$

Using the spin density (Eq. 8.10), we obtain

$$\int d\mathbf{r}_1 \sum_{\mathbf{R}} \sum_{\mathbf{R}'} K_{1,1,1,1}(\mathbf{r}_1; \mathbf{R} - \mathbf{R}') e_{1,1}(\mathbf{r}_1) \frac{V}{N} \rho_x(\mathbf{R}) \frac{V}{N} \rho_x(\mathbf{R}'), \tag{9.11}$$

where $\mathbf{R}$ and $\mathbf{R}'$ represent the lattice positions correspond to $\mathbf{r}_2$ and $\mathbf{r}_3$, respectively. For a uniform deformation, $\int d\mathbf{r} e_{i,j}(\mathbf{r}) = e_{i,j}$, above expression is simplified to

$$e_{1,1} (\frac{V}{N})^2 \sum_{\mathbf{R}} \sum_{\mathbf{R}'} K_{1,1,1,1}(\mathbf{R} - \mathbf{R}') \rho_x(\mathbf{R}) \rho_x(\mathbf{R}'). \tag{9.12}$$

Employing the definition of spin density (Eq. 8.11), this becomes

$$e_{1,1} (\frac{V}{N})^2 \sum_{\mathbf{R}} \sum_{\mathbf{R}'} K_{1,1,1,1}(\mathbf{R} - \mathbf{R}') (\mathbf{S}_x e^{i\mathbf{Q}\mathbf{R}} + \mathbf{S}_x^* e^{-i\mathbf{Q}\mathbf{R}} + m_x)(\mathbf{S}_x e^{i\mathbf{Q}\mathbf{R}'} + \mathbf{S}_x^* e^{-i\mathbf{Q}\mathbf{R}'} + m_x), \tag{9.13}$$

which can be rewritten as

$$\begin{aligned} e_{1,1} (\frac{V}{N})^2 & \sum_{\mathbf{R}} \sum_{\mathbf{R}'} K_{1,1,1,1}(\mathbf{R} - \mathbf{R}') \\ & (\mathbf{S}_x \mathbf{S}_x e^{i\mathbf{Q}(\mathbf{R}+\mathbf{R}')} + \mathbf{S}_x \mathbf{S}_x^* e^{i\mathbf{Q}(\mathbf{R}-\mathbf{R}')} + \mathbf{S}_x e^{i\mathbf{Q}\mathbf{R}} m_x + \mathbf{S}_x^* \mathbf{S}_x e^{i\mathbf{Q}(\mathbf{R}'-\mathbf{R})} \\ & + \mathbf{S}_x^* \mathbf{S}_x^* e^{-i\mathbf{Q}(\mathbf{R}+\mathbf{R}')} + \mathbf{S}_x^* e^{-i\mathbf{Q}\mathbf{R}} m_x + \mathbf{S}_x e^{i\mathbf{Q}\mathbf{R}'} m_x + \mathbf{S}_x^* e^{-i\mathbf{Q}\mathbf{R}'} m_x + m_x^2). \end{aligned} \tag{9.14}$$

Defining $\boldsymbol{\tau} = \mathbf{R}' - \mathbf{R}$, Expression 9.14 becomes

$$e_{1,1}(\frac{V}{N})^2 \sum_{\mathbf{R}} \sum_{\boldsymbol{\tau}} K_{1,1,1,1}(\boldsymbol{\tau})$$
$$(\mathbf{S}_x \mathbf{S}_x e^{i\mathbf{Q}(\boldsymbol{\tau}+2\mathbf{R})} + \mathbf{S}_x \mathbf{S}_x^* e^{-i\mathbf{Q}\boldsymbol{\tau}} + \mathbf{S}_x e^{i\mathbf{Q}\mathbf{R}} m_x + \mathbf{S}_x^* \mathbf{S}_x e^{i\mathbf{Q}\boldsymbol{\tau}} + \mathbf{S}_x^* \mathbf{S}_x^* e^{-i\mathbf{Q}(\boldsymbol{\tau}+2\mathbf{R})}$$
$$+ \mathbf{S}_x^* e^{-i\mathbf{Q}\mathbf{R}} m_x + \mathbf{S}_x e^{i\mathbf{Q}(\boldsymbol{\tau}+\mathbf{R})} m_x + \mathbf{S}_x^* e^{-i\mathbf{Q}(\boldsymbol{\tau}+\mathbf{R})} m_x + m_x^2). \tag{9.15}$$

According to the Landau model, the ordered spin structure is characterized by the wave vector $\mathbf{Q}$ with using the $n$th Fourier component of the spin density to define the order parameter[9]. Here for the case of $CsNiCl_3$, all the ordered phases have a periodicity of 3, hence, $n$ is 3 and $3\mathbf{Q}$ is equivalent to a reciprocal lattice vector $\mathbf{G}$. Based on this discussion, we have $3\mathbf{Q} = \mathbf{G}$ and then

$$\frac{1}{N} \sum_{\mathbf{R}} e^{\pm i 2\mathbf{Q}\mathbf{R}} = \Delta_{2\mathbf{Q},\mathbf{G}} = 0 \tag{9.16}$$

and

$$\frac{1}{N} \sum_{\mathbf{R}} e^{\pm i\mathbf{Q}\mathbf{R}} = \Delta_{\mathbf{Q},\mathbf{G}} = 0, \tag{9.17}$$

where $\Delta_{n\mathbf{Q},\mathbf{G}}$ is Kronecker $\delta$ function, which is

$$\Delta_{n\mathbf{Q},\mathbf{G}} = \begin{cases} 1 & \text{if } n\mathbf{Q} = \mathbf{G}, \\ 0 & \text{otherwise}, \end{cases} \tag{9.18}$$

so that Expression 9.15 becomes

$$e_{1,1} \frac{V}{N} \sum_{\boldsymbol{\tau}} K_{1,1,1,1}(\boldsymbol{\tau})(\mathbf{S}_x \mathbf{S}_x^* e^{-i\mathbf{Q}\boldsymbol{\tau}} + \mathbf{S}_x^* \mathbf{S}_x e^{i\mathbf{Q}\boldsymbol{\tau}} + m_x^2). \tag{9.19}$$

Defining

$$K_{1,1,\pm Q} = \frac{V}{N} \sum_{\boldsymbol{\tau}} K_{1,1,1,1}(\boldsymbol{\tau}) e^{\pm i\mathbf{Q}\boldsymbol{\tau}}, \tag{9.20}$$

and

$$K_{1,1,0} = \frac{V}{N} \sum_{\boldsymbol{\tau}} K_{1,1,1,1}(\boldsymbol{\tau}), \tag{9.21}$$

Expression 9.19 can be rewritten as

$$K_{1,1,Q}e_{1,1}(\mathbf{S}_x\mathbf{S}_x^* + \mathbf{S}_x^*\mathbf{S}_x) + K_{1,1,0}e_{1,1}m_x^2. \tag{9.22}$$

Using the same approach, the invariant terms for the l-q coupling can be obtained as

$$\begin{aligned}
F_{C(l-q)} = {} & K_{1,1,Q}e_{1,1}(\mathbf{S}_x\mathbf{S}_x^* + \mathbf{S}_x^*\mathbf{S}_x) + K_{1,1,0}e_{1,1}m_x^2 \\
& + K_{1,1,Q}e_{2,2}(\mathbf{S}_y\mathbf{S}_y^* + \mathbf{S}_y^*\mathbf{S}_y) + K_{1,1,0}e_{2,2}m_y^2 \\
& + 2K_{1,1,Q}e_{1,2}(\mathbf{S}_x\mathbf{S}_y^* + \mathbf{S}_x^*\mathbf{S}_y) + 2K_{1,1,0}e_{1,2}m_xm_y \\
& + K_{1,2,Q}e_{1,1}(\mathbf{S}_y\mathbf{S}_y^* + \mathbf{S}_y^*\mathbf{S}_y) + K_{1,2,0}e_{1,1}m_y^2 \\
& + K_{1,2,Q}e_{2,2}(\mathbf{S}_x\mathbf{S}_x^* + \mathbf{S}_x^*\mathbf{S}_x) + K_{1,2,0}e_{2,2}m_x^2 \\
& - 2K_{1,2,Q}e_{1,2}(\mathbf{S}_x\mathbf{S}_y^* + \mathbf{S}_x^*\mathbf{S}_y) - 2K_{1,2,0}e_{1,2}m_xm_y \\
& + K_{1,3,Q}(e_{1,1} + e_{2,2})(\mathbf{S}_z\mathbf{S}_z^* + \mathbf{S}_z^*\mathbf{S}_z) + K_{1,3,0}(e_{1,1} + e_{2,2})m_z^2 \\
& + K_{3,1,Q}e_{3,3}(\mathbf{S}_x\mathbf{S}_x^* + \mathbf{S}_x^*\mathbf{S}_x) + K_{3,1,0}e_{3,3}m_x^2 \\
& + K_{3,1,Q}e_{3,3}(\mathbf{S}_y\mathbf{S}_y^* + \mathbf{S}_y^*\mathbf{S}_y) + K_{3,1,0}e_{3,3}m_y^2 \\
& + K_{3,3,Q}e_{3,3}(\mathbf{S}_z\mathbf{S}_z^* + \mathbf{S}_z^*\mathbf{S}_z) + K_{3,3,0}e_{3,3}m_z^2 \\
& + 4K_{5,5,Q}e_{1,3}(\mathbf{S}_x\mathbf{S}_z^* + \mathbf{S}_x^*\mathbf{S}_z) + 4K_{5,5,0}e_{1,3}m_xm_z \\
& + 4K_{5,5,Q}e_{2,3}(\mathbf{S}_y\mathbf{S}_z^* + \mathbf{S}_y^*\mathbf{S}_z) + 4K_{5,5,0}e_{2,3}m_ym_z,
\end{aligned} \tag{9.23}$$

where the coefficients are defined as

$$K_{\alpha,\beta,Q} = \frac{V}{N}\sum_{\boldsymbol{\tau}} K_{i,j,k,l}(\boldsymbol{\tau})e^{\pm i\mathbf{Q}\boldsymbol{\tau}}. \tag{9.24a}$$

$$K_{\alpha,\beta,0} = \frac{V}{N}\sum_{\boldsymbol{\tau}} K_{i,j,k,l}(\boldsymbol{\tau}). \tag{9.24b}$$

Here, $\alpha$ and $\beta$ are Voigt indexes associated with the invariant elements $K_{i,j,k,l}$.

As mentioned in Section 8.1.2, the polarization vector can be written in terms of real vectors as

$$\mathbf{S} = \mathbf{S}_1 + i\mathbf{S}_2, \tag{9.25}$$

and for the case of the magnetic field applied along the c-direction (z-axis), $\mathbf{S}_1$ and $\mathbf{S}_2$ are given by

$$\mathbf{S}_1 = S\cos\beta[\sin\theta\ \hat{\rho}_1 + \cos\theta\ \hat{z}], \tag{9.26a}$$

$$\mathbf{S}_2 = S\sin\beta\ \hat{\rho}_2. \tag{9.26b}$$

Here, $\hat{\rho}_1$ and $\hat{\rho}_2$ are two perpendicular unit vectors lying in the basal plane. Thus, we define $\hat{\rho}_1$ and $\hat{\rho}_2$ in terms of the in-plane unit vectors $\hat{x}$ and $\hat{y}$ as

$$\hat{\rho}_1 = \cos\phi\ \hat{x} + \sin\phi\ \hat{y}, \tag{9.27a}$$

$$\hat{\rho}_2 = -\sin\phi\ \hat{x} + \cos\phi\ \hat{y}, \tag{9.27b}$$

where $\phi$ is the phase angle measured relative to an arbitrary x-direction. Therefore, $\mathbf{S}_1$ and $\mathbf{S}_2$ can be rewritten in terms of $\hat{x}$, $\hat{y}$ and $\hat{z}$ as

$$\mathbf{S}_1 = S\cos\beta[\sin\theta(\cos\phi\ \hat{x} + \sin\phi\ \hat{y}) + \cos\theta\ \hat{z}], \tag{9.28a}$$

$$\mathbf{S}_2 = S\sin\beta(-\sin\phi\ \hat{x} + \cos\phi\ \hat{y}). \tag{9.28b}$$

For H//z, where $m_x = m_y = 0$, making use of the Voigt notation for the strains (Eq. 9.3), the l-q magnetoelastic coupling terms can be simplified as

$$\begin{aligned}
F_{C'(l-q)} &= 2(K_{1,1,Q}e_1 + K_{1,2,Q}e_2 + K_{3,1,Q}e_3)S^2(\cos^2\beta\sin^2\theta\cos^2\phi + \sin^2\beta\sin^2\phi) \\
&+ 2(K_{1,1,Q}e_2 + K_{1,2,Q}e_1 + K_{3,1,Q}e_3)S^2(\cos^2\beta\sin^2\theta\sin^2\phi + \sin^2\beta\cos^2\phi) \\
&+ 2(K_{1,3,Q}(e_1 + e_2) + K_{3,3,Q}e_3)S^2\cos^2\beta\cos^2\theta \\
&+ 2K_{5,5,Q}e_4S^2\sin 2\theta\cos^2\beta\sin\phi \\
&+ 2K_{5,5,Q}e_5S^2\sin 2\theta\cos^2\beta\cos\phi \\
&+ (K_{1,1,Q} - K_{1,2,Q})e_6S^2\sin 2\phi(\cos^2\beta\sin^2\theta - \sin^2\beta) \\
&+ (K_{1,3,0}(e_1 + e_2) + K_{3,3,0}e_3)m_z^2.
\end{aligned} \tag{9.29}$$

Again, using the definition of the parameters $S_\perp = S\sin\beta$ and $\zeta = \cos\theta$, the l-q magnetoelastic coupling terms can be furthermore simplified. We notice that, $\sin 2\theta = 2\sin\theta\cos\theta = \zeta\sqrt{1-\zeta^2}$. Thus, for $\zeta = 1$ and $\zeta = 0$, $\sin 2\theta = 0$. Therefore, we can simply drop all terms proportional to $\sin 2\theta$, and Eq. 9.29 reduces to

$$\begin{aligned} F_{C(l-q)}(e,S,S_\perp,\zeta) = \\ & 2(K_{1,1,Q}e_1 + K_{1,2,Q}e_2 + K_{3,1,Q}e_3)[(S^2 - S_\perp^2)(1-\zeta^2)\cos^2\phi + S_\perp^2\sin^2\phi] \\ & + 2(K_{1,1,Q}e_2 + K_{1,2,Q}e_1 + K_{3,1,Q}e_3)[(S^2 - S_\perp^2)(1-\zeta^2)\sin^2\phi + S_\perp^2\cos^2\phi] \\ & + 2(K_{1,3,Q}(e_1+e_2) + K_{3,3,Q}e_3)(S^2 - S_\perp^2)\zeta^2 \\ & + (K_{1,1,Q} - K_{1,2,Q})e_6[(S^2 - S_\perp^2)(1-\zeta^2) - S_\perp^2]\sin 2\phi \\ & + (K_{1,3,0}(e_1+e_2) + K_{3,3,0}e_3)m_z^2. \end{aligned} \tag{9.30}$$

### 9.2.2 q-q magnetoelastic coupling terms

Quadratic-quadratic (q-q) magnetoelastic coupling terms, $\sum_{m,n,p,q,r,s} V_{m,n,p,q,r,s}e_{m,n}e_{p,q}S_rS_s$, can be determined using the same approach. First, we find that there are 17 independent coupling terms $V_{m,n,p,q,r,s}$ allowed by symmetry, where indexes $m, n, p, q, r$ and $s$ run from 1 to 3. After evaluating each integrals, the coupling coefficients are defined as

$$V_{\alpha,\beta,\gamma,Q} = \frac{V}{N}\sum\nolimits_{\boldsymbol{\tau}} V_{\alpha,\beta,\gamma}(\boldsymbol{\tau})e^{\pm i\mathbf{Q}\boldsymbol{\tau}}, \tag{9.31a}$$

$$V_{\alpha,\beta,\gamma,0} = \frac{V}{N}\sum\nolimits_{\boldsymbol{\tau}} V_{\alpha,\beta,\gamma}(\boldsymbol{\tau}), \tag{9.31b}$$

where $\alpha, \beta, \gamma = 1, 2, 3, 4, 5, 6$.

The q-q coupling terms are listed in Table 9.1. All these q-q magnetoelastic coupling terms can be simplified with the spin relations. For a magnetic field applied along c-direction ($m_x = m_y = 0$), the nonzero q-q magnetoelastic coupling terms are listed in Table 9.2. As discussed in the previous section, any coupling terms

| Coefficients | Associated terms |
|---|---|
| $V_{1,1,1,Q}$ | $\frac{1}{3}(3e_{1,1}^2+e_{2,2}^2)(\mathbf{S}_x\mathbf{S}_x^*+\mathbf{S}_x^*\mathbf{S}_x)+\frac{2}{3}(2e_{1,2}^2+e_{2,2}^2+e_{1,1}e_{2,2})(\mathbf{S}_y\mathbf{S}_y^*+\mathbf{S}_y^*\mathbf{S}_y)+\frac{8}{3}e_{1,2}e_{2,2}(\mathbf{S}_x\mathbf{S}_y^*+\mathbf{S}_x^*\mathbf{S}_y)$ |
| $V_{1,1,2,Q}$ | $\frac{2}{3}(3e_{1,2}^2+e_{2,2}^2)(\mathbf{S}_x\mathbf{S}_x^*+\mathbf{S}_x^*\mathbf{S}_x)+\frac{1}{3}(3e_{1,1}^2+2e_{1,2}^2+e_{2,2}^2-2e_{1,1}e_{2,2})(\mathbf{S}_y\mathbf{S}_y^*+\mathbf{S}_y^*\mathbf{S}_y)-\frac{8}{3}e_{1,2}e_{2,2}(\mathbf{S}_x\mathbf{S}_y^*+\mathbf{S}_x^*\mathbf{S}_y)$ |
| $V_{1,1,3,Q}$ | $(e_{1,1}^2+e_{2,2}^2+2e_{1,2}^2)(\mathbf{S}_z\mathbf{S}_z^*+\mathbf{S}_z^*\mathbf{S}_z)$ |
| $V_{1,2,1,Q}$ | $-2(e_{1,2}^2-e_{1,1}e_{2,2})(\mathbf{S}_x\mathbf{S}_x^*+\mathbf{S}_x^*\mathbf{S}_x)-2(e_{1,2}^2-e_{1,1}e_{2,2})(\mathbf{S}_y\mathbf{S}_y^*+\mathbf{S}_y^*\mathbf{S}_y)$ |
| $V_{1,2,3,Q}$ | $-2(e_{1,2}^2-e_{1,1}e_{2,2})(\mathbf{S}_z\mathbf{S}_z^*+\mathbf{S}_z^*\mathbf{S}_z)$ |
| $V_{1,3,1,Q}$ | $2e_{1,1}e_{3,3}(\mathbf{S}_x\mathbf{S}_x^*+\mathbf{S}_x^*\mathbf{S}_x)+2e_{2,2}e_{3,3}(\mathbf{S}_y\mathbf{S}_y^*+\mathbf{S}_y^*\mathbf{S}_y)+4e_{1,2}e_{3,3}(\mathbf{S}_x\mathbf{S}_y^*+\mathbf{S}_x^*\mathbf{S}_y)$ |
| $V_{1,3,2,Q}$ | $2e_{2,2}e_{3,3}(\mathbf{S}_x\mathbf{S}_x^*+\mathbf{S}_x^*\mathbf{S}_x)+2e_{1,1}e_{3,3}(\mathbf{S}_y\mathbf{S}_y^*+\mathbf{S}_y^*\mathbf{S}_y)-4e_{1,2}e_{3,3}(\mathbf{S}_x\mathbf{S}_y^*+\mathbf{S}_x^*\mathbf{S}_y)$ |
| $V_{1,3,3,Q}$ | $2(e_{1,1}+e_{2,2})e_{3,3}(\mathbf{S}_z\mathbf{S}_z^*+\mathbf{S}_z^*\mathbf{S}_z)$ |
| $V_{1,4,4,Q}$ | $-8(e_{1,2}e_{2,3}-e_{1,3}e_{2,2})(\mathbf{S}_x\mathbf{S}_z^*+\mathbf{S}_x^*\mathbf{S}_z)-8(e_{1,2}e_{1,3}-e_{1,1}e_{2,3})(\mathbf{S}_y\mathbf{S}_z^*+\mathbf{S}_y^*\mathbf{S}_z)$ |
| $V_{1,5,5,Q}$ | $8(e_{1,1}e_{1,3}+e_{1,2}e_{2,3})(\mathbf{S}_x\mathbf{S}_z^*+\mathbf{S}_x^*\mathbf{S}_z)+8(e_{1,2}e_{1,3}+e_{2,2}e_{2,3})(\mathbf{S}_y\mathbf{S}_z^*+\mathbf{S}_y^*\mathbf{S}_z)$ |
| $V_{1,6,6,Q}$ | $\frac{4}{3}(3e_{1,2}^2-e_{2,2}^2)(\mathbf{S}_x\mathbf{S}_x^*+\mathbf{S}_x^*\mathbf{S}_x)+\frac{4}{3}(e_{2,2}^2-e_{1,2}^2-2e_{1,1}e_{2,2})(\mathbf{S}_y\mathbf{S}_y^*+\mathbf{S}_y^*\mathbf{S}_y)+\frac{8}{3}(3e_{1,1}e_{1,2}-e_{1,2}e_{2,2})(\mathbf{S}_x\mathbf{S}_y^*+\mathbf{S}_x^*\mathbf{S}_y)$ |
| $V_{3,3,1,Q}$ | $e_{3,3}^2(\mathbf{S}_x\mathbf{S}_x^*+\mathbf{S}_x^*\mathbf{S}_x)+e_{3,3}^2(\mathbf{S}_y\mathbf{S}_y^*+\mathbf{S}_y^*\mathbf{S}_y)$ |
| $V_{3,3,3,Q}$ | $e_{3,3}^2(\mathbf{S}_z\mathbf{S}_z^*+\mathbf{S}_z^*\mathbf{S}_z)$ |
| $V_{3,5,5,Q}$ | $8e_{1,3}e_{3,3}(\mathbf{S}_x\mathbf{S}_z^*+\mathbf{S}_x^*\mathbf{S}_z)+8e_{2,3}e_{3,3}(\mathbf{S}_y\mathbf{S}_z^*+\mathbf{S}_y^*\mathbf{S}_z)$ |
| $V_{5,5,1,Q}$ | $4e_{1,3}^2(\mathbf{S}_x\mathbf{S}_x^*+\mathbf{S}_x^*\mathbf{S}_x)+4e_{2,3}^2(\mathbf{S}_y\mathbf{S}_y^*+\mathbf{S}_y^*\mathbf{S}_y)+8e_{1,3}e_{2,3}(\mathbf{S}_x\mathbf{S}_y^*+\mathbf{S}_x^*\mathbf{S}_y)$ |
| $V_{5,5,2,Q}$ | $4e_{2,3}^2(\mathbf{S}_x\mathbf{S}_x^*+\mathbf{S}_x^*\mathbf{S}_x)+4e_{1,3}^2(\mathbf{S}_y\mathbf{S}_y^*+\mathbf{S}_y^*\mathbf{S}_y)-8e_{1,3}e_{2,3}(\mathbf{S}_x\mathbf{S}_y^*+\mathbf{S}_x^*\mathbf{S}_y)$ |
| $V_{5,5,3,Q}$ | $4(e_{1,3}^2+e_{2,3}^2)(\mathbf{S}_z\mathbf{S}_z^*+\mathbf{S}_z^*\mathbf{S}_z)$ |
| $V_{1,1,1,0}$ | $\frac{1}{3}(3e_{1,1}^2+e_{2,2}^2)m_x^2+\frac{2}{3}(2e_{1,2}^2+e_{2,2}^2+e_{1,1}e_{2,2})m_y^2+\frac{8}{3}e_{1,2}e_{2,2}m_xm_y$ |
| $V_{1,1,2,0}$ | $\frac{2}{3}(3e_{1,2}^2+e_{2,2}^2)m_x^2+\frac{1}{3}(3e_{1,1}^2+2e_{1,2}^2+e_{2,2}^2-2e_{1,1}e_{2,2})m_y^2-\frac{8}{3}e_{1,2}e_{2,2}m_xm_y$ |
| $V_{1,1,3,0}$ | $(e_{1,1}^2+e_{2,2}^2+2e_{1,2}^2)m_z^2$ |
| $V_{1,2,1,0}$ | $-2(e_{1,2}^2-e_{1,1}e_{2,2})m_x^2-2(e_{1,2}^2-e_{1,1}e_{2,2})m_y^2$ |
| $V_{1,2,3,0}$ | $-2(e_{1,2}^2-e_{1,1}e_{2,2})m_z^2$ |
| $V_{1,3,1,0}$ | $2e_{1,1}e_{3,3}m_x^2+2e_{2,2}e_{3,3}m_y^2+4e_{1,2}e_{3,3}m_xm_y$ |
| $V_{1,3,2,0}$ | $2e_{2,2}e_{3,3}m_x^2+2e_{1,1}e_{3,3}m_y^2-4e_{1,2}e_{3,3}m_xm_y$ |
| $V_{1,3,3,0}$ | $2(e_{1,1}+e_{2,2})e_{3,3}m_z^2$ |
| $V_{1,4,4,0}$ | $-8(e_{1,2}e_{2,3}-e_{1,3}e_{2,2})m_xm_z-8(e_{1,2}e_{1,3}-e_{1,1}e_{2,3})m_ym_z$ |
| $V_{1,5,5,0}$ | $8(e_{1,1}e_{1,3}+e_{1,2}e_{2,3})m_xm_z+8(e_{1,2}e_{1,3}+e_{2,2}e_{2,3})m_ym_z$ |
| $V_{1,6,6,0}$ | $\frac{4}{3}(3e_{1,2}^2-e_{2,2}^2)m_x^2+\frac{4}{3}(e_{2,2}^2-e_{1,2}^2-2e_{1,1}e_{2,2})m_y^2+\frac{8}{3}(3e_{1,1}e_{1,2}-e_{1,2}e_{2,2})m_xm_y$ |
| $V_{3,3,1,0}$ | $e_{3,3}^2m_x^2+e_{3,3}^2m_y^2$ |
| $V_{3,3,3,0}$ | $e_{3,3}^2m_z^2$ |
| $V_{3,5,5,0}$ | $8e_{1,3}e_{3,3}m_xm_z+8e_{2,3}e_{3,3}m_ym_z$ |
| $V_{5,5,1,0}$ | $4e_{1,3}^2m_x^2+4e_{2,3}^2m_y^2+8e_{1,3}e_{2,3})m_xm_y$ |
| $V_{5,5,2,0}$ | $4e_{2,3}^2m_x^2+4e_{1,3}^2m_y^2-8e_{1,3}e_{2,3})m_xm_y$ |
| $V_{5,5,3,0}$ | $4(e_{1,3}^2+e_{2,3}^2)m_z^2$ |

Table 9.1: Quadratic-quadratic magnetoelastic coupling terms sorted by the coefficients. These coefficients are defined in Eq. 9.31.

| Coefficients | Associated terms |
|---|---|
| $V_{1,1,1,Q}$ | $\frac{2}{3}(3e_1^2+e_2^2)[(S^2-S_\perp^2)(1-\zeta^2)\cos^2\phi+S_\perp^2\sin^2\phi]$<br>$+\frac{2}{3}(2e_2^2+e_6^2+2e_1e_2)[(S^2-S_\perp^2)(1-\zeta^2)\sin^2\phi+S_\perp^2\cos^2\phi]$<br>$+\frac{4}{3}e_2e_6\sin 2\phi[(S^2-S_\perp^2)(1-\zeta^2)-S_\perp^2]$ |
| $V_{1,1,2,Q}$ | $\frac{1}{6}(4e_2^2+3e_6^2)[(S^2-S_\perp^2)(1-\zeta^2)\cos^2\phi+S_\perp^2\sin^2\phi]$<br>$+\frac{1}{6}(6e_1^2+2e_2^2+e_6^2-4e_1e_2)[(S^2-S_\perp^2)(1-\zeta^2)\sin^2\phi+S_\perp^2\cos^2\phi]$<br>$-\frac{4}{3}e_2e_6\sin 2\phi[(S^2-S_\perp^2)(1-\zeta^2)-S_\perp^2]$ |
| $V_{1,1,3,Q}$ | $(2e_1^2+2e_2^2+e_6^2)(S^2-S_\perp^2)\zeta^2$ |
| $V_{1,2,1,Q}$ | $(4e_1e_2-e_6^2)[(S^2-S_\perp^2)(1-\zeta^2)\cos^2\phi+S_\perp^2\sin^2\phi]$<br>$+(4e_1e_2-e_6^2)[(S^2-S_\perp^2)(1-\zeta^2)\sin^2\phi+S_\perp^2\cos^2\phi]$ |
| $V_{1,2,3,Q}$ | $(4e_1e_2-e_6^2)(S^2-S_\perp^2)\zeta^2$ |
| $V_{1,3,1,Q}$ | $4e_1e_3[(S^2-S_\perp^2)(1-\zeta^2)\cos^2\phi+S_\perp^2\sin^2\phi]$<br>$+4e_2e_3[(S^2-S_\perp^2)(1-\zeta^2)\sin^2\phi+S_\perp^2\cos^2\phi]$<br>$+2e_3e_6\sin 2\phi[(S^2-S_\perp^2)(1-\zeta^2)-S_\perp^2]$ |
| $V_{1,3,2,Q}$ | $4e_2e_3[(S^2-S_\perp^2)(1-\zeta^2)\cos^2\phi+S_\perp^2\sin^2\phi]$<br>$+4e_1e_3[(S^2-S_\perp^2)(1-\zeta^2)\sin^2\phi+S_\perp^2\cos^2\phi]$<br>$-2e_3e_6\sin 2\phi[(S^2-S_\perp^2)(1-\zeta^2)-S_\perp^2]$ |
| $V_{1,3,3,Q}$ | $4(e_1+e_2)e_3(S^2-S_\perp^2)\zeta^2$ |
| $V_{1,6,6,Q}$ | $\frac{2}{3}(3e_6^2-4e_2^2)[(S^2-S_\perp^2)(1-\zeta^2)\cos^2\phi+S_\perp^2\sin^2\phi]$<br>$+\frac{4}{3}(2e_2^2-e_6^2-4e_1e_2)[(S^2-S_\perp^2)(1-\zeta^2)\sin^2\phi+S_\perp^2\cos^2\phi]$<br>$+\frac{4}{3}(3e_1e_6-e_2e_6)\sin 2\phi[(S^2-S_\perp^2)(1-\zeta^2)-S_\perp^2]$ |
| $V_{3,3,1,Q}$ | $2e_3^2[(S^2-S_\perp^2)(1-\zeta^2)\cos^2\phi+S_\perp^2\sin^2\phi]$<br>$+2e_3^2[(S^2-S_\perp^2)(1-\zeta^2)\sin^2\phi+S_\perp^2\cos^2\phi]$ |
| $V_{3,3,3,Q}$ | $2e_3^2(S^2-S_\perp^2)\zeta^2$ |
| $V_{5,5,1,Q}$ | $2e_5^2[(S^2-S_\perp^2)(1-\zeta^2)\cos^2\phi+S_\perp^2\sin^2\phi]$<br>$+2e_4^2[(S^2-S_\perp^2)(1-\zeta^2)\sin^2\phi+S_\perp^2\cos^2\phi]$<br>$+2e_4e_5\sin 2\phi[(S^2-S_\perp^2)(1-\zeta^2)-S_\perp^2]$ |
| $V_{5,5,2,Q}$ | $2e_4^2[(S^2-S_\perp^2)(1-\zeta^2)\cos^2\phi+S_\perp^2\sin^2\phi]$<br>$+2e_5^2[(S^2-S_\perp^2)(1-\zeta^2)\sin^2\phi+S_\perp^2\cos^2\phi]$<br>$-2e_4e_5\sin 2\phi[(S^2-S_\perp^2)(1-\zeta^2)-S_\perp^2]$ |
| $V_{5,5,3,Q}$ | $2(e_4^2+e_5^2)(S^2-S_\perp^2)\zeta^2$ |
| $V_{1,1,3,0}$ | $\frac{1}{2}(2e_1^2+2e_2^2+e_6^2)m_z^2$ |
| $V_{1,2,3,0}$ | $\frac{1}{2}(4e_1e_2-e_6^2)m_z^2$ |
| $V_{1,3,3,0}$ | $2(e_1+e_2)e_3m_z^2$ |
| $V_{3,3,3,0}$ | $e_3^2m_z^2$ |
| $V_{5,5,3,0}$ | $(e_4^2+e_5^2)m_z^2$ |

Table 9.2: Nonzero quadratic-quadratic magnetoelastic coupling terms represented in terms of the order parameters.

proportional to $\sin 2\theta$ vanish. Moreover, because $m_x = m_y = 0$, only terms with $m_z^2$ remain.

For the linear phase, as spins align parallel to the c-direction, strains only couple with $S$. For the elliptical phase, both spin components (basal plane and parallel to the c-direction are ordered), so we have both $S_\perp^2$ and $S_z^2 = S^2 - S_\perp^2$ in the coupling terms. For the magnetic field induced $120^\circ$ phase, the spins are almost aligned in the basal plane, with a small component along the c-axis. Therefore, both $S$ and $S_\perp$ remain nonzero in this phase. Furthermore, as derived by Eq. 8.38, $S = \sqrt{2}S_\perp$.

So far the elastic energy, $F_{el}$, and magnetoelastic coupling terms, $F_C(e, \eta)$, of $CsNiCl_3$ are derived. Together with the Landau free-energy of $CsNiCl_3$, $F_L(\eta)$, which is obtained by Plumer et al.[11],[11], the total free energy of $CsNiCl_3$, $F_{total}$, can be written out according to Eq. 9.1. Based on this total free energy, the elastic constants can be calculated in all the four phases. This will be discussed in the next chapter.

# Chapter 10

# Elastic constants of $CsNiCl_3$

The elastic constants $C^*_{mn}$ in the low temperature phases can be calculated according to the total free energy $F_{total}$ by using[64]

$$C^*_{mn} = \frac{\partial^2 F_{total}}{\partial e_m \partial e_n} - \frac{\partial^2 F_{total}}{\partial \eta \partial e_m}\left(\frac{\partial^2 F_{total}}{\partial \eta^2}\right)^{-1}\frac{\partial^2 F_{total}}{\partial e_n \partial \eta}, \tag{10.1}$$

where $e_m$ and $e_n$ represent strain components and $\eta$ is the order parameter. Given that the total free energy, $F_{total}$, is expressed in terms of the order parameters ($S$, $S_\perp$ and $\zeta$), the magnetization ($m_z$), and the strains ($e_m$), the calculated elastic constants are also written as functions of these parameters. The temperature and magnetic field dependence of the order parameters and magnetization have already been obtained in Section 8.1.3, while that of the strains are derived in this chapter. Based on these results, the temperature and magnetic field dependence of the elastic constants can be obtained in all four phases. These theoretical results are used to reproduce the behavior of the elastic constants as a function of the temperature and the magnetic field.

We notice that the total free energy is also function of an unspecified angle, $\phi$. As a matter of fact, $\phi$ plays an important role in describing the symmetry properties of

$CsNiCl_3$. Therefore, the value of $\phi$ is determined first in this chapter.

## 10.1 Discussion of $\phi = 0$

For the case of a magnetic field applied along the c-direction, as shown in Eq. 9.25 and Eq. 9.26, the polarization vector $\mathbf{S}$ is expressed in terms of orthogonal unit vectors $\hat{z}$, $\hat{\rho_1}$ and $\hat{\rho_2}$. Here $\hat{z}$ is along the c-direction while $\hat{\rho_1}$ and $\hat{\rho_2}$ lie in the basal plane. In Eq. 9.27, the angle $\phi$ is employed to define the orientation of $\hat{\rho_1}$ and $\hat{\rho_2}$ relative to the lattice basis vectors. As shown in Fig. 10.1, for the hexagonal antiferromagnet $CsNiCl_3$, the in-plane positions of the magnetic $Ni^{2+}$ ions with respect to the hexagonal lattice are

$$\mathbf{R}_n = n_1\mathbf{a} + n_2\mathbf{b}, \tag{10.2}$$

where $\mathbf{a}$ and $\mathbf{b}$ are the primitive Bravais-lattices vectors in the basal plane and $n_i$ are integers.

According to the NMR observation[10] and X. Zhu's theoretical calculation[9], the basal-plane component of magnetic moment is found to be perpendicular to one of the in-plane primitive reciprocal-lattice vectors. As a result, as shown in Fig .10.1, for example, if the magnetic moment is perpendicular to $\vec{a}^*$, it must be aligned along $y$-axis. This also indicates that there are six equivalent magnetic domains rotated by 60° relative to each other. Hence, as the $x$ and $y$ directions can be interchanged, one of the domains corresponds to $\phi = 0$. This is also supported by neutron-diffraction studies[65]. Therefore, in the following calculation, $\phi = 0$ is used to determine the temperature and magnetic field dependence of the strains and the elastic constants.

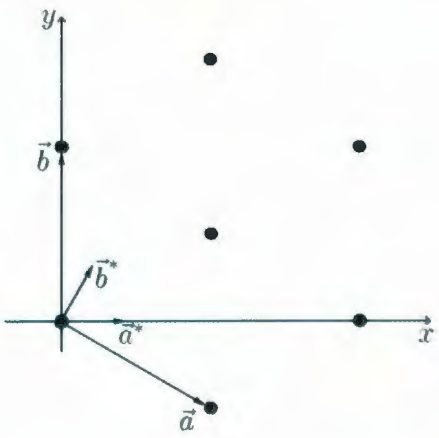


Figure 10.1: Positions of $Ni^{2+}$ magnetic ions in the basal plane, where $\vec{a}$ and $\vec{b}$ are primitive Bravais-lattice vectors while $\vec{a}^*$ and $\vec{b}^*$ are primitive reciprocal-lattice vectors.

## 10.2 Temperature and magnetic field dependence of strain

Minimizing the free energy with respect to the strains, we can solve for the temperature and magnetic field dependence of strains. With only l-q coupling terms, the total free energy has the form of

$$F_{total(l-q)} = F_L(S, S_\perp, \zeta) + F_{el}(e) + Fc_{(l-q)}(e, S, S_\perp, \zeta). \tag{10.3}$$

The full expressions of $F_L(S, S_\perp, \zeta)$, $F_{el}(e)$ and $Fc_{(l-q)}(e, S, S_\perp, \zeta)$ are shown by Eq. 8.17, Eq. 9.4 and Eq. 9.30. Minimizing $F_{total(l-q)}$ with respect to the strains,

$$\frac{\partial F_{total(l-q)}}{\partial e_n} = 0, \tag{10.4}$$

solutions for each strain components, as function of order parameters ($S$ and $S_\perp$) and magnetization ($m_z$), are obtained. To be consistent with the experimental data

of thermal expansion coefficient in the basal plane obtained by Rayne *et al*[55], the elastic constant $C_{13}$ has been set to zero.

In the linear phase, where $S_\perp = 0$ and $\zeta = 1$, we obtain that

$$e_1 = -\frac{2K_{1,3,Q}S^2 + K_{1,3,0}m_z^2}{C_{11}+C_{12}}, \tag{10.5a}$$

$$e_2 = -\frac{2K_{1,3,Q}S^2 + K_{1,3,0}m_z^2}{C_{11}+C_{12}}, \tag{10.5b}$$

$$e_3 = -\frac{2K_{3,3,Q}S^2 + K_{3,3,0}m_z^2}{C_{33}}, \tag{10.5c}$$

$$e_4 = 0, \tag{10.5d}$$

$$e_5 = 0, \tag{10.5e}$$

$$e_6 = 0. \tag{10.5f}$$

We notice that, $e_4 = e_5 = e_6 = 0$, which shows that no shear deformation exist, and $e_1 = e_2$, which indicates that in the basal plane the deformations along $x$ and $y$ directions are equivalent. Furthermore, all the strains are independent of the phase angle $\phi$.

In the elliptical phase, given both $S_\perp$ and $S$ are nonzero and $\zeta = 1$, the corresponding strains are

$$e_1 = -\frac{2K_{1,1,Q}S_\perp^2(\sin^2\phi C_{11} - \cos^2\phi C_{12}) + 2K_{1,2,Q}S_\perp^2(\cos^2\phi C_{11} - \sin^2\phi C_{12})}{C_{11}^2 - C_{12}^2} - \frac{2K_{1,3,Q}(S^2 - S_\perp^2) + K_{1,3,0}m_z^2}{C_{11}+C_{12}}, \tag{10.6a}$$

$$e_2 = -\frac{2K_{1,2,Q}S_\perp^2(\sin^2\phi C_{11} - \cos^2\phi C_{12}) + 2K_{1,1,Q}S_\perp^2(\cos^2\phi C_{11} - \sin^2\phi C_{12})}{C_{11}^2 - C_{12}^2} - \frac{2K_{1,3,Q}(S^2 - S_\perp^2) + K_{1,3,0}m_z^2}{C_{11}+C_{12}}, \tag{10.6b}$$

$$e_3 = -\frac{2K_{3,3,Q}(S^2 - S_\perp^2) + 2K_{3,1,Q}S_\perp^2 + K_{3,3,0}m_z^2}{C_{33}}, \tag{10.6c}$$

$$e_4 = 0, \tag{10.6d}$$

$$e_5 = 0, \tag{10.6e}$$

$$e_6 = \frac{(K_{1,1,Q} - K_{1,2,Q})S_\perp^2 \sin 2\phi}{C_{66}}. \tag{10.6f}$$

Based on these results, for an arbitrary angle $\phi$, the shear deformation $e_6$ would drive the crystal symmetry into a monoclinic structure. However, as discussed in Section 10.1, one of the six domains for $CsNiCl_3$ corresponds to $\phi$ is zero. Therefore, for a mono-domain with $\phi = 0$, the above equations can be rewritten as

$$e_1 = \frac{2(K_{1,1,Q}C_{12} - K_{1,2,Q}C_{11})S_\perp^2}{C_{11}^2 - C_{12}^2} - \frac{2K_{1,3,Q}(S^2 - S_\perp^2) + K_{1,3,0}m_z^2}{C_{11} + C_{12}}, \tag{10.7a}$$

$$e_2 = \frac{2(K_{1,2,Q}C_{12} - K_{1,1,Q}C_{11})S_\perp^2}{C_{11}^2 - C_{12}^2} - \frac{2K_{1,3,Q}(S^2 - S_\perp^2) + K_{1,3,0}m_z^2}{C_{11} + C_{12}}, \tag{10.7b}$$

$$e_3 = -\frac{2K_{3,3,Q}(S^2 - S_\perp^2) + 2K_{3,1,Q}S_\perp^2 + K_{3,3,0}m_z^2}{C_{33}}; \tag{10.7c}$$

$$e_4 = 0, \tag{10.7d}$$

$$e_5 = 0, \tag{10.7e}$$

$$e_6 = 0. \tag{10.7f}$$

We notice that $e_1$ and $e_2$ are no longer equal to each other. This actually leads to a symmetry change, which will be discussed later in this chapter.

For the $120^\circ$ phase, where $S = \sqrt{2}S_\perp$ and $\zeta = 0$, the strains give

$$e_1 = -\frac{2(K_{1,1,Q} + K_{1,2,Q})S_\perp^2 + K_{1,3,0}m_z^2}{C_{11} + C_{12}}, \tag{10.8a}$$

$$e_2 = -\frac{2(K_{1,1,Q} + K_{1,2,Q})S_\perp^2 + K_{1,3,0}m_z^2}{C_{11} + C_{12}}, \tag{10.8b}$$

$$e_3 = -\frac{4K_{3,1,Q}S_\perp^2 + K_{3,3,0}m_z^2}{C_{33}}, \tag{10.8c}$$

$$e_4 = 0, \tag{10.8d}$$

$$e_5 = 0, \tag{10.8e}$$

$$e_6 = 0. \tag{10.8f}$$

In this phase, as in the linear phase, the strains are independent of $\phi$ and $e_1 = e_2$.

For each phase, the temperature and magnetic field dependence of order parameters $S$ and $S_\perp$ and magnetization $m_z$ are given in Section 8.1.3. Using these results, the temperature and field dependence of the strains in each phase can be calculated. Coefficients $a$, $A_z$, $T_Q$, $B$ and $B_2$ are given in Table 8.2 and Table 8.3 while the elastic constants $C_{11}$, $C_{12}$ and $C_{33}$ are given in Table 6.1. The coefficients $K_{i,j,Q}$, which are listed in Table 12.1 and Table A.1, can be determined by comparing the experimental data and the model predictions. Given the temperature dependence of $e_1$ and $e_3$, it is possible to calculate the thermal expansion coefficients $\alpha_1 = \frac{\partial e_1}{\partial T}$ and $\alpha_3 = \frac{\partial e_3}{\partial T}$. Our predictions are compared to the temperature dependence of the thermal expansion coefficients $\alpha_1 = \frac{\partial e_1}{\partial T}$ and $\alpha_3 = \frac{\partial e_3}{\partial T}$ obtained by Rayne *et al*[55]. To reproduce the experimental data, the non-mean-field order parameters, with $\beta \approx 0.35$, has been used. The comparison between the numerical and experimental data is shown in Fig. 10.2.

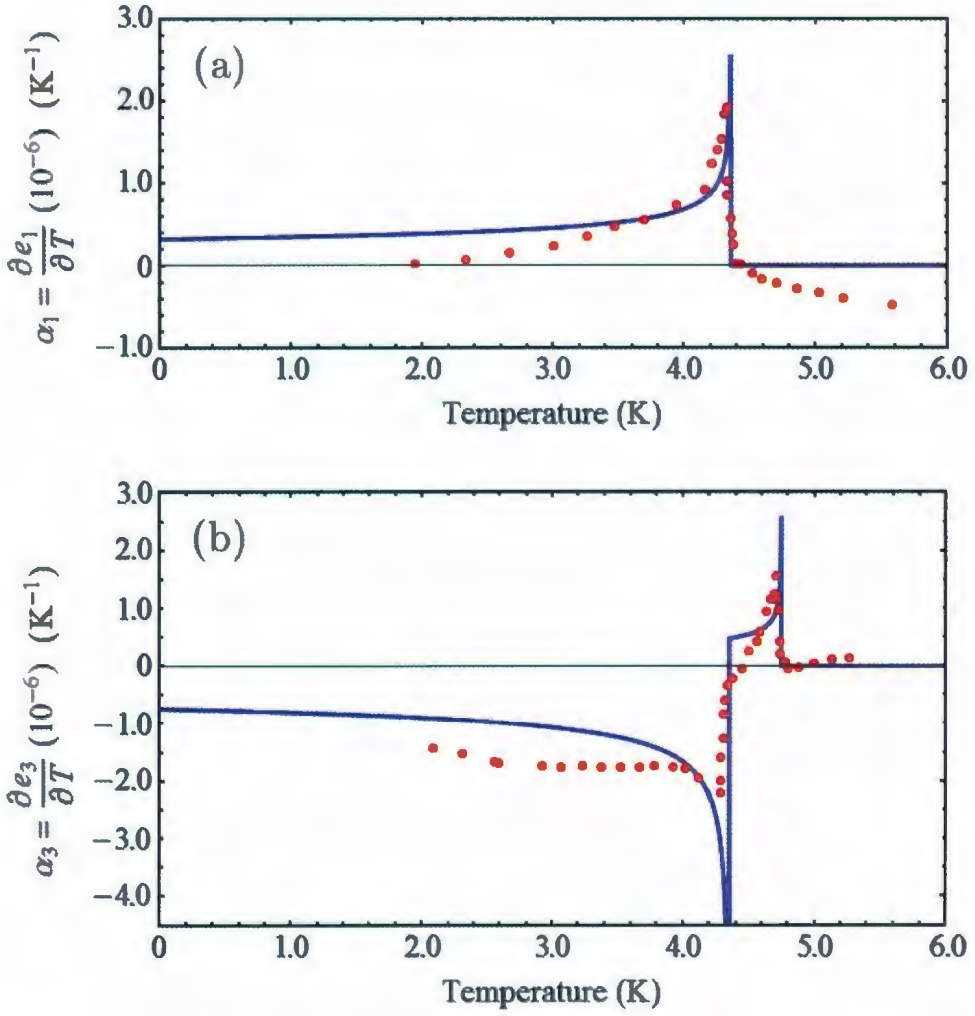


Figure 10.2: Temperature dependence of (a) $\alpha_1 = \frac{\partial e_1}{\partial T}$ (thermal expansion coefficient in basal plane) and (b) $\alpha_3 = \frac{\partial e_3}{\partial T}$ (thermal expansion coefficient along the c-axis) at zero field of $CsNiCl_3$. The solid lines and the dots are the model predictions and experimental data obtained by Rayne *et al*[55], respectively.

## 10.3 Temperature and magnetic field dependence of the elastic constants

The goal here is to obtain the temperature and magnetic field dependence of the elastic constants of $CsNiCl_3$ for the case of a magnetic field applied along the c-direction. Therefore, in this section, the 9 nonzero elastic constants are calculated based on the total free energy derived in Chapter 9.

As shown in Section 8.1.2 and Chapter 9, the total free energy is written in terms of the order parameters ($S$, $S_\perp$ and $\zeta$), magnetization ($m_z$), and strains ($e_m$). According to Table 8.1, $\eta$ stands for the order parameter in a specific phase. Therefore, the calculation of the elastic constants $C^*_{mn}$ is treated separately with respect to each phase. Furthermore, to address the magnetic field dependence of the elastic constants, we expand the general form of $C^*_{mn}$ as

$$C^*_{mn} = \frac{\partial^2 F_{total}}{\partial e_m \partial e_n} - \frac{\partial^2 F_{total}}{\partial \eta \partial e_m}\left(\frac{\partial^2 F_{total}}{\partial \eta^2}\right)^{-1}\frac{\partial^2 F_{total}}{\partial e_n \partial \eta} - \frac{\partial^2 F_{total}}{\partial m_z \partial e_m}\left(\frac{\partial^2 F_{total}}{\partial m_z^2}\right)^{-1}\frac{\partial^2 F_{total}}{\partial e_n \partial m_z}, \quad (10.9)$$

where $F_{total}$ is the total free energy derived in Chapter 9.

We notice that, after inspection of the linear-quadratic (l-q) magnetoelastic coupling terms derived in Chapter 9, only couplings with $e_1$, $e_2$ and $e_3$ are allowed. Therefore, in order to fully account for the temperature and field dependence of the elastic constants, in particularly for $C_{44}$ and $C_{66}$, quadratic-quadratic (q-q) coupling terms are also required.

Paramagnetic phase

In the paramagnetic phase, the order parameters $S$ and $S_\perp$ are both zero while $\zeta = 1$. In other words, the second part of Eq. 10.9 is irrelevant in this case. Therefore,

Eq. 10.9 can be simplified to the form of

$$C^*_{mn(p)} = \frac{\partial^2 F_{total(p)}}{\partial e_m \partial e_n} - \frac{\partial^2 F_{total(p)}}{\partial m_z \partial e_m}\left(\frac{\partial^2 F_{total(p)}}{\partial m_z^2}\right)^{-1}\frac{\partial^2 F_{total(p)}}{\partial e_n \partial m_z}. \tag{10.10}$$

The exact analytical solution is too complicated to write here. However, a good approximation can be obtained by treating the l-q and q-q contribution separately. Minimizing the free energy relative to the magnetization, we have

$$\frac{\partial F_{total(p)(l-q)}}{\partial m_z} = -H + A_0 m_z + B_3 m_z^3 + 2K_{1,3,0}(e_1+e_2)m_z + 2K_{3,3,0}e_3 m_z = 0, \tag{10.11}$$

where $F_{total(p)(l-q)}$ is the total free energy in the paramagnetic phase which only includes the l-q magnetoelastic coupling terms, and then $A_0$ can be rewritten as

$$A_{0(p)} = \frac{H}{m_z} - B_3 m_z^2 - 2K_{1,3,0}(e_1+e_2) - 2K_{3,3,0}e_3. \tag{10.12}$$

The second derivation of $F_{total(p)(l-q)}$ with respect to the magnetization in the second part of Eq. 10.10 is calculated as

$$\frac{\partial^2 F_{total(p)(l-q)}}{\partial m_z^2} = A_0 + 3B_3 m_z^3 + 2K_{1,3,0}(e_1+e_2) + 2K_{3,3,0}e_3. \tag{10.13}$$

Making use of the result from Eq. 10.12, $\frac{\partial^2 F_{total(p)(l-q)}}{\partial m_z^2}$ can be simplified as

$$\frac{\partial^2 F_{total(p)(l-q)}}{\partial m_z^2} = \frac{H}{m_z} + 2B_3 m_z^2. \tag{10.14}$$

Using the approach describe above, the nonzero elastic constants in the paramagnetic state are

$$C^*_{11(p)} = C_{11} + 2V_{1,1,3,0}m_z^2 - \frac{4K_{1,3,0}^2 m_z^3}{2B_3 m_z^3 + H}, \tag{10.15a}$$

$$C^*_{12(p)} = C_{12} + 2V_{1,2,3,0}m_z^2 - \frac{4K_{1,3,0}^2 m_z^3}{2B_3 m_z^3 + H}, \tag{10.15b}$$

$$C^*_{13(p)} = C_{13} + 2V_{1,3,3,0}m_z^2 - \frac{4K_{1,3,0}K_{3,3,0} m_z^3}{2B_3 m_z^3 + H}, \tag{10.15c}$$

$$C^*_{22(p)} = C_{11} + 2V_{1,1,3,0}m_z^2 - \frac{4K_{1,3,0}^2 m_z^3}{2B_3 m_z^3 + H}, \tag{10.15d}$$

$$C^*_{23(p)} = C_{13} + 2V_{1,3,3,3,0}m_z^2 - \frac{4K_{1,3,0}K_{3,3,0}m_z^3}{2B_3m_z^3 + H}, \tag{10.15e}$$

$$C^*_{33(p)} = C_{33} + 2V_{3,3,3,3,0}m_z^2 - \frac{4K_{3,3,0}^2m_z^3}{2B_3m_z^3 + H}, \tag{10.15f}$$

$$C^*_{44(p)} = C_{55} + 2V_{5,5,3,3,0}m_z^2, \tag{10.15g}$$

$$C^*_{55(p)} = C_{55} + 2V_{5,5,3,3,0}m_z^2, \tag{10.15h}$$

$$C^*_{66(p)} = C_{66} + (V_{1,1,3,3,0} - V_{1,2,3,3,0})m_z^2. \tag{10.15i}$$

Here, the results show that, in the paramagnetic phase, the change in the elastic constants is only due to the magnetic field.

Linear phase

Compared with the calculation in the paramagnetic phase, calculations in the linear phase also involve a contribution from the order parameter. In the linear phase, $S \neq 0$, $S_\perp = 0$ and $\zeta = 1$. Therefore, $\eta$ in Eq. 10.9 represents the order parameter $S$. According to Eq. 9.30 and Table 9.2, the elastic constants calculated in the linear phase correspond to

$$C^*_{11(l)} = C_{11} - \frac{4K_{1,3,Q}^2}{B} + 4V_{1,1,3,Q}S^2 + 2V_{1,1,3,3,0}m_z^2 + \frac{4(K_{1,3,0} - 2B_6K_{1,3,Q})^2m_z^3}{2(2BB_6^2 - B_3)m_z^3 - H}, \tag{10.16a}$$

$$C^*_{12(l)} = C_{12} - \frac{4K_{1,3,Q}^2}{B} + 4V_{1,2,3,Q}S^2 + 2V_{1,2,3,3,0}m_z^2 + \frac{4(K_{1,3,0} - 2B_6K_{1,3,Q})^2m_z^3}{2(2BB_6^2 - B_3)m_z^3 - H}, \tag{10.16b}$$

$$\begin{aligned} C^*_{13(l)} = {} & C_{13} - \frac{4K_{1,3,Q}K_{3,3,Q}}{B} + 4V_{1,3,3,Q}S^2 \\ & + 2V_{1,3,3,3,0}m_z^2 + \frac{4(K_{1,3,0} - 2B_6K_{1,3,Q})(K_{3,3,0} - 2B_6K_{3,3,Q})m_z^3}{2(2BB_6^2 - B_3)m_z^3 - H}, \end{aligned} \tag{10.16c}$$

$$C^*_{22(l)} = C_{11} - \frac{4K_{1,3,Q}^2}{B} + 4V_{1,1,3,Q}S^2 + 2V_{1,1,3,3,0}m_z^2 + \frac{4(K_{1,3,0} - 2B_6K_{1,3,Q})^2m_z^3}{2(2BB_6^2 - B_3)m_z^3 - H}, \tag{10.16d}$$

$$\begin{aligned} C^*_{23(l)} = {} & C_{13} - \frac{4K_{1,3,Q}K_{3,3,Q}}{B} + 4V_{1,3,3,Q}S^2 \\ & + 2V_{1,3,3,3,0}m_z^2 + \frac{4(K_{1,3,0} - 2B_6K_{1,3,Q})(K_{3,3,0} - 2B_6K_{3,3,Q})m_z^3}{2(2BB_6^2 - B_3)m_z^3 - H}, \end{aligned} \tag{10.16e}$$

$$C^*_{33(l)} = C_{33} - \frac{4K_{3,3,Q}^2}{B} + 4V_{3,3,3,Q}S^2 + 2V_{3,3,3,3,0}m_z^2 + \frac{4(K_{3,3,0} - 2B_6K_{3,3,Q})^2m_z^3}{2(2BB_6^2 - B_3)m_z^3 - H}, \tag{10.16f}$$

$$C^*_{44(l)} = C_{55} + 4V_{5,5,3,Q}S^2 + 2V_{5,5,3,3,0}m_z^2, \tag{10.16g}$$

$$C^*_{55(l)} = C_{55} + 4V_{5,5,3,Q}S^2 + 2V_{5,5,3,3,0}m_z^2, \tag{10.16h}$$

$$C^*_{66(l)} = C_{66} + 2(V_{1,1,3,Q} - V_{1,2,3,Q})S^2 + (V_{1,1,3,0} - V_{1,2,3,0})m_z^2, \tag{10.16i}$$

where $B_6 = \frac{2B_4+B_5}{B}$. We immediately notice that the q-q coupling terms between the strains and the order parameter lead to a $S^2$ dependence. Secondly, in comparison with results obtained in the paramagnetic phase, the magnetization dependence is in general more complex. However, for $C^*_{44(l)}$, $C^*_{55(l)}$, and $C^*_{66(l)}$, the magnetization dependence remains the same. As shown by Eq. 10.9, the calculations of $C^*_{44(l)}$, $C^*_{55(l)}$ and $C^*_{66(l)}$ are directly related with strains $e_4$, $e_5$, and $e_6$, which appear in the q-q coupling terms. Finally, we also notice that a constant term appears for the first 6 nonzero elastic constants. This is due to the l-q coupling term between the strains and the order parameter.

Elliptical phase

In the elliptical phase, both $S$ and $S_\perp$ are nonzero, $\zeta = 1$, and $\phi$ is set to zero in Eq. 9.30 and Table 9.2. Consequently, we obtain for the elliptical phase the results listed in Eq. 10.17.

$$\begin{aligned} C^*_{11(e)} = {} & C_{11} - \frac{(K_{1,2,Q} + B_7 K_{1,3,Q})^2}{B_8} \\ & + 4V_{1,1,3,Q}S^2 + 4(V_{1,1,2,Q} - V_{1,1,3,Q})S_\perp^2 \\ & + 2V_{1,1,3,0}m_z^2 + \frac{(B_9 K_{1,2,Q} + 2K_{1,3,0} + B_{10}K_{1,3,Q})^2 m_z^3}{(B_{11} - 2B_3)m_z^3 - H}, \end{aligned} \tag{10.17a}$$

$$\begin{aligned} C^*_{12(e)} = {} & C_{12} - \frac{(K_{1,1,Q} + B_7 K_{1,3,Q})(K_{1,2,Q} + B_7 K_{1,3,Q})}{B_8} \\ & + 4V_{1,2,3,Q}S^2 + \frac{2}{3}(2V_{1,1,1,Q} - 2V_{1,1,2,Q} + 6V_{1,2,1,Q} - 6V_{1,2,3,Q} - 8V_{1,6,6,Q})S_\perp^2 \\ & + 2V_{1,2,3,0}m_z^2 + \frac{(B_9 K_{1,1,Q} + 2K_{1,3,0} + B_{10}K_{1,3,Q})(B_9 K_{1,2,Q} + 2K_{1,3,0} + B_{10}K_{1,3,Q})m_z^3}{(B_{11} - 2B_3)m_z^3 - H}, \end{aligned} \tag{10.17b}$$

$$\begin{aligned} C^*_{13(e)} = {} & C_{13} - \frac{(K_{1,2,Q} + B_7 K_{1,3,Q})(K_{3,1,Q} + B_7 K_{3,3,Q})}{B_8} \\ & + 4V_{1,3,3,Q}S^2 + 4(V_{1,3,2,Q} - V_{1,3,3,Q})S_\perp^2 \\ & + 2V_{1,3,3,0}m_z^2 + \frac{(B_9 K_{1,2,Q} + 2K_{1,3,0} + B_{10}K_{1,3,Q})(B_9 K_{3,1,Q} + 2K_{3,3,0} + B_{10}K_{3,3,Q})m_z^3}{(B_{11} - 2B_3)m_z^3 - H}, \end{aligned} \tag{10.17c}$$

$$C^*_{22(e)} = C_{11} - \frac{(K_{1,1,Q} + B_7 K_{1,3,Q})^2}{B_8} + 4V_{1,1,3,Q}S^2 + \frac{2}{3}(4(V_{1,1,1,Q} + 2V_{1,1,2,Q} - 6V_{1,1,3,Q} + 8V_{1,6,6,Q})S_\perp^2 + 2V_{1,1,3,0}m_z^2 + \frac{(B_9 K_{1,1,Q} + 2K_{1,3,0} + B_{10}K_{1,3,Q})^2 m_z^3}{(B_{11} - 2B_3)m_z^3 - H}, \tag{10.17d}$$

$$C^*_{23(e)} = C_{13} - \frac{(K_{1,1,Q} + B_7 K_{1,3,Q})(K_{3,1,Q} + B_7 K_{3,3,Q})}{B_8} + 4V_{1,3,3,Q}S^2 + 4(V_{1,3,1,Q} - V_{1,3,3,Q})S_\perp^2 + 2V_{1,3,3,0}m_z^2 + \frac{(B_9 K_{1,1,Q} + 2K_{1,3,0} + B_{10}K_{1,3,Q})(B_9 K_{3,1,Q} + 2K_{3,3,0} + B_{10}K_{3,3,Q})m_z^3}{(B_{11} - 2B_3)m_z^3 - H}, \tag{10.17e}$$

$$C^*_{33(e)} = C_{33} - \frac{(K_{3,1,Q} + B_7 K_{3,3,Q})^2}{B_8} + 4V_{3,3,3,Q}S^2 + 4(V_{3,3,1,Q} - V_{3,3,3,Q})S_\perp^2 + 2V_{3,3,3,0}m_z^2 + \frac{(B_9 K_{3,1,Q} + 2K_{3,3,0} + B_{10}K_{3,3,Q})^2 m_z^3}{(B_{11} - 2B_3)m_z^3 - H}, \tag{10.17f}$$

$$C^*_{44(e)} = C_{55} + 4V_{5,5,3,Q}S^2 + 4(V_{5,5,1,Q} - V_{5,5,3,Q})S_\perp^2 + 2V_{5,5,3,0}m_z^2, \tag{10.17g}$$

$$C^*_{55(e)} = C_{55} + 4V_{5,5,3,Q}S^2 + 4(V_{5,5,2,Q} - V_{5,5,3,Q})S_\perp^2 + 2V_{5,5,3,0}m_z^2, \tag{10.17h}$$

$$C^*_{66(e)} = C_{66} + 2(V_{1,1,3,Q} - V_{1,2,3,Q})S^2 + \frac{1}{3}(4V_{1,1,1,Q} + 2V_{1,1,2,Q} - 6V_{1,1,3,Q} - 6V_{1,2,1,Q} + 6V_{1,2,3,Q} - 4V_{1,6,6,Q})S_\perp^2 + (V_{1,1,3,0} - V_{1,2,3,0})m_z^2, \tag{10.17i}$$

where

$$B_7 = \frac{2B_2 - B}{B}, \tag{10.18a}$$

$$B_8 = \frac{(B - B_2)B_2}{B}, \tag{10.18b}$$

$$B_9 = \frac{2(B_4 - B_2 B_6)}{B_8}, \tag{10.18c}$$

$$B_{10} = \frac{-2(BB_4 + B_2 B_5)}{BB_8}, \tag{10.18d}$$

$$B_{11} = \frac{4(B_4^2 + B_2 B_5 B_6)}{B_8}. \tag{10.18e}$$

120° phase

In the 120° phase, $S$ and $S_\perp$ are still nonzero, however, $\zeta$ becomes zero. This accounts for the first-order phase transition between the elliptical and the 120° phase. In this phase, we choose $S_\perp$ as the phase order parameter and use that

$$S = \sqrt{2}\, S_\perp. \tag{10.19}$$

The elastic constants in the 120° phase are listed in Eq. 10.20.

$$\begin{aligned} C^*_{11(120)} &= C_{11} - \frac{(K_{1,1,Q} + K_{1,2,Q})^2}{B - B_2} \\ &\quad + 4(V_{1,1,1,Q} + V_{1,1,2,Q})S_\perp^2 \\ &\quad + 2V_{1,1,3,0}m_z^2 + \frac{4(B_{12}(K_{1,1,Q} + K_{1,2,Q}) + K_{1,3,0})^2 m_z^3}{-2(2B_5B_{12} + B_3)m_z^3 - H}, \end{aligned} \tag{10.20a}$$

$$\begin{aligned} C^*_{12(120)} &= C_{12} - \frac{(K_{1,1,Q} + K_{1,2,Q})^2}{B - B_2} \\ &\quad + \frac{4}{3}(V_{1,1,1,Q} - V_{1,1,2,Q} + 6V_{1,2,1,Q} - 4V_{1,6,6,Q})S_\perp^2 \\ &\quad + 2V_{1,2,3,0}m_z^2 + \frac{4(B_{12}(K_{1,1,Q} + K_{1,2,Q}) + K_{1,3,0})^2 m_z^3}{-2(2B_5B_{12} + B_3)m_z^3 - H}, \end{aligned} \tag{10.20b}$$

$$\begin{aligned} C^*_{13(120)} &= C_{13} - \frac{2(K_{1,1,Q} + K_{1,2,Q})K_{3,1,Q}}{B - B_2} \\ &\quad + 4(V_{1,3,1,Q} + V_{1,3,2,Q})S_\perp^2 \\ &\quad + 2V_{1,3,3,0}m_z^2 + \frac{4(B_{12}(K_{1,1,Q} + K_{1,2,Q}) + K_{1,3,0})(2B_{12}K_{3,1,Q} + K_{3,3,0})m_z^3}{-2(2B_5B_{12} + B_3)m_z^3 - H}, \end{aligned} \tag{10.20c}$$

$$\begin{aligned} C^*_{22(120)} &= C_{11} - \frac{(K_{1,1,Q} + K_{1,2,Q})^2}{B - B_2} \\ &\quad + 4(V_{1,1,1,Q} + V_{1,1,2,Q})S_\perp^2 \\ &\quad + 2V_{1,1,3,0}m_z^2 + \frac{4(B_{12}(K_{1,1,Q} + K_{1,2,Q}) + K_{1,3,0})^2 m_z^3}{-2(2B_5B_{12} + B_3)m_z^3 - H}, \end{aligned} \tag{10.20d}$$

$$\begin{aligned} C^*_{23(120)} &= C_{13} - \frac{2(K_{1,1,Q} + K_{1,2,Q})K_{3,1,Q}}{B - B_2} \\ &\quad + 4(V_{1,3,1,Q} + V_{1,3,2,Q})S_\perp^2 \\ &\quad + 2V_{1,3,3,0}m_z^2 + \frac{4(B_{12}(K_{1,1,Q} + K_{1,2,Q}) + K_{1,3,0})(2B_{12}K_{3,1,Q} + K_{3,3,0})m_z^3}{-2(2B_5B_{12} + B_3)m_z^3 - H}, \end{aligned} \tag{10.20e}$$

$$\begin{aligned} C^*_{33(120)} &= C_{33} - \frac{4K_{3,1,Q}^2}{B - B_2} + 8V_{3,3,1,Q}S_\perp^2 \\ &\quad + 2V_{3,3,3,0}m_z^2 + \frac{4(2B_{12}K_{3,1,Q} + K_{3,3,0})^2 m_z^3}{-2(2B_5B_{12} + B_3)m_z^3 - H}, \end{aligned} \tag{10.20f}$$

$$C^*_{44(120)} = C_{55} + 4(V_{5,5,1,Q} + V_{5,5,2,Q})S_\perp^2 + 2V_{5,5,3,0}m_z^2, \tag{10.20g}$$

$$C^*_{55(120)} = C_{55} + 4(V_{5,5,1,Q} + V_{5,5,2,Q})S_\perp^2 + 2V_{5,5,3,0}m_z^2, \tag{10.20h}$$

$$C^*_{66(120)} = C_{66} + \frac{4}{3}(V_{1,1,1,Q} + 2V_{1,1,2,Q} - 3V_{1,2,1,Q} + 2V_{1,6,6,Q})S_\perp^2 + (V_{1,1,3,0} - V_{1,2,3,0})m_z^2, \tag{10.20i}$$

with $B_{12} = \frac{B_5}{B_2 - B}$.

## 10.4 Broken symmetry

According to Table 10.1[56], strains and elastic constants can be used to determine the symmetry of a crystal in different phases. As discussed in Section 10.1, we oriented the spins along the x-axis and therefore $\phi = 0$. This is used to determine the expressions of the strains and elastic constants of $CsNiCl_3$ in all the four phases.

According to Eq. 10.5 and Eq. 10.7, no shear deformation exists in the lower field ordered phases and the basal plane deformations $e_1$ and $e_2$ are equivalent in the linear phase. Hence, according to our calculation, the strain matrices for the linear and elliptical phases correspond to

$$e_{(l)} = \begin{pmatrix} e_1 & 0 & 0 \\ 0 & e_1 & 0 \\ 0 & 0 & e_3 \end{pmatrix}, \tag{10.21}$$

and

$$e_{(e)} = \begin{pmatrix} e_1 & 0 & 0 \\ 0 & e_2 & 0 \\ 0 & 0 & e_3 \end{pmatrix}. \tag{10.22}$$

Referring to Table 10.1, we notice that the symmetry of the strain tensor is still consistent with that of the hexagonal structure in the linear phase. In the elliptical

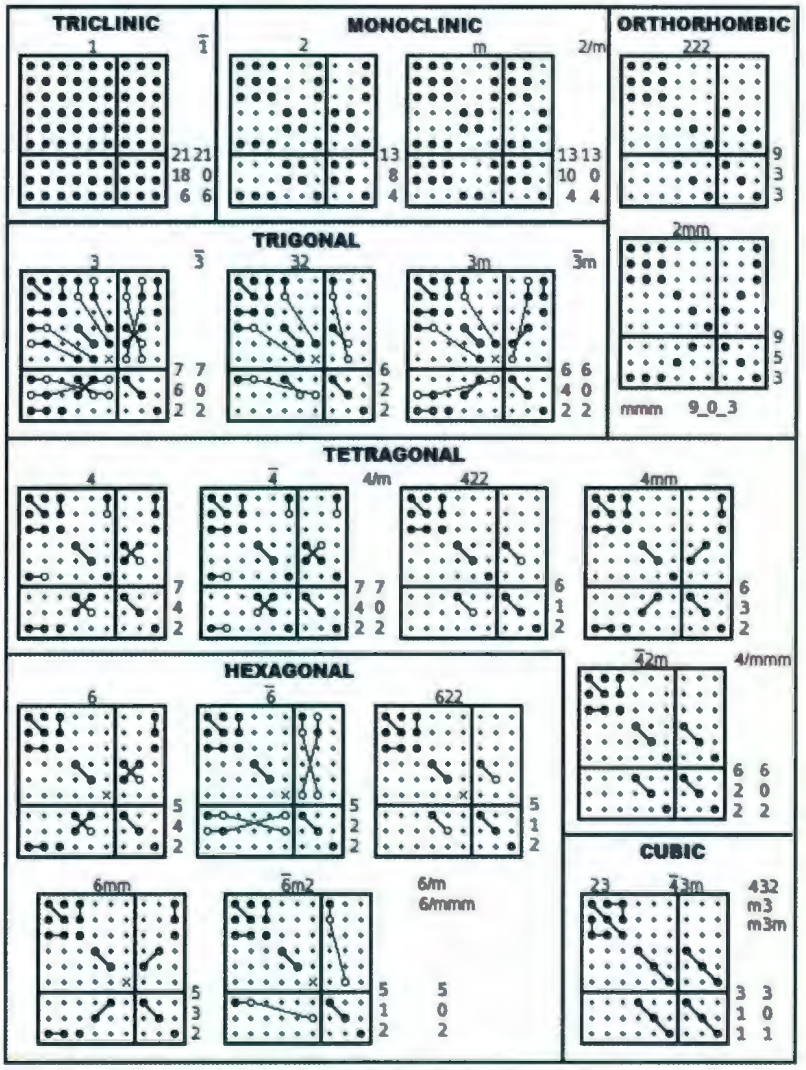


Table 10.1: Table of the matrices for elastic constants (the $6 \times 6$ tensor), piezoelectric constants (the $3 \times 6$ and $6 \times 3$ tensor) and dielectric constants (strains, the $3 \times 3$ tensor). The solid and empty circles represent the nonzero elements in these tensors. The solid circles joined by the lines are equal to each other while the empty circle has opposite sign with the solid circle on the other end of the line. The small cross appears at the $C_{66}$ position denotes the relation of $C_{66} = \frac{1}{2}(C_{11} - C_{12})$.

phase, the hexagonal symmetry, $c_1 = c_2$, is broken. This indicates, that from the linear phase to the elliptical phase, the spin structure of $CsNiCl_3$ reduces the symmetry to a lower space group. This is also supported by our elastic constant calculations. In the paramagnetic phase and the linear phase, as shown by Eq. 10.15 and Eq. 10.16, we obtain $C_{11} = C_{22}$, $C_{13} = C_{23}$, $C_{44} = C_{55}$, and $C_{66} = \frac{1}{2}(C_{11} - C_{12})$. This is in agreement with the features of the $P6_3/mmc$ hexagonal elastic constants tensor

$$C_{hexagonal} = \begin{pmatrix} C_{11} & C_{12} & C_{13} & 0 & 0 & 0 \\ C_{12} & C_{11} & C_{13} & 0 & 0 & 0 \\ C_{13} & C_{13} & C_{33} & 0 & 0 & 0 \\ 0 & 0 & 0 & C_{44} & 0 & 0 \\ 0 & 0 & 0 & 0 & C_{44} & 0 \\ 0 & 0 & 0 & 0 & 0 & C_{66} \end{pmatrix}, \tag{10.23}$$

where $C_{66} = \frac{1}{2}(C_{11} - C_{12})$. However, in the elliptical phase, according to Eq. 10.17, the number of independent elastic constants increases to 9 and the new symmetry corresponds to that of the orthorhombic structure with

$$C_{orthorhombic} = \begin{pmatrix} C_{11} & C_{12} & C_{13} & 0 & 0 & 0 \\ C_{12} & C_{22} & C_{23} & 0 & 0 & 0 \\ C_{13} & C_{23} & C_{33} & 0 & 0 & 0 \\ 0 & 0 & 0 & C_{44} & 0 & 0 \\ 0 & 0 & 0 & 0 & C_{55} & 0 \\ 0 & 0 & 0 & 0 & 0 & C_{66} \end{pmatrix}, \tag{10.24}$$

where $C_{66} = \frac{1}{2}(C_{11} - C_{12})$ is not required.

In the magnetic field induced $120^o$ phase, according to Eq. 10.8, the strain tensor

can be expressed by

$$e_{(120)} = \begin{pmatrix} e_1 & 0 & 0 \\ 0 & e_1 & 0 \\ 0 & 0 & e_3 \end{pmatrix}. \tag{10.25}$$

Compared with the strain tensors in the linear and elliptical phases, here given $e_1 = e_2$, we may suppose that the symmetry changes back to hexagonal when crossing the first-order phase boundary between the elliptical and the $120^{\circ}$ phase. This is again confirmed by the elastic constants calculation. As shown by Eq. 10.20, in the $120^{\circ}$ phase, all the features, $C_{11} = C_{22}$, $C_{13} = C_{23}$, $C_{44} = C_{55}$, and $C_{66} = \frac{1}{2}(C_{11} - C_{12})$, appear again indicating a hexagonal symmetry property which is the same as that in the linear phase.

In summary, based on the symmetry properties of both strains and elastic constants matrices in the three ordered phases, the hexagonal symmetry is broken only in the elliptical phase.

# Chapter 11

# Critical behavior of $CsNiCl_3$ near phase transitions

As a frustrated Heisenberg antiferromagnet $CsNiCl_3$ shows a novel type of multicritical behavior. As shown in Fig. 11.1, according to Kawamura[4], the criticality of both phase transitions at lower magnetic fields ($H < H_m$) belong to the $XY$ type with a predicted order parameter exponent $\beta \approx 0.35$. These two second-order phase transition lines merge at the multicritical point ($T_m \approx 4.50$ K, $H_m \approx 2.29$ T), which is described by Kawamura as a new chiral Heisenberg fixed point with $\beta \approx 0.28$. These predictions are supported by some experimental results shown in Table 11.1.

The criticality along the high magnetic field critical line, which is associated with the field-induced 120° spin structure, is predicted by Kawamura to belong to a new $XY(n = 2)$ chirality class with $\beta \approx 0.25$. However, claims[20]–[26] have also been made recently pointing out that the character of this phase transition should rather be weakly first-order. In order to resolve this controversy, the data presented in this section focus on the evolution of the critical behavior as a function of the magnetic field.

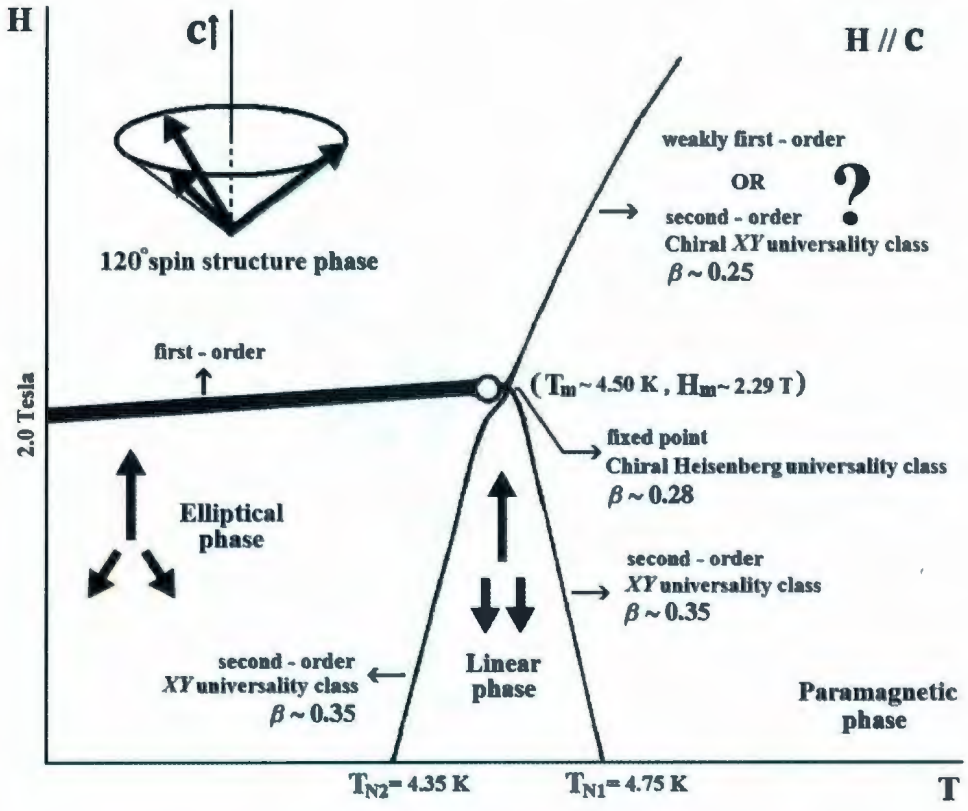


Figure 11.1: Magnetic phase diagram of $CsNiCl_3$ for field oriented along the c-direction.

| Exponent | Experimental value | Theoretical value[18] | | | |
|---|---|---|---|---|---|
| | | Chiral $XY$ | Chiral Heisenberg | $XY$ | Heisenberg |
| $\beta_1$ | $0.32_{\pm 0.03}$[29] | $0.25_{\pm 0.01}$ | $0.30_{\pm 0.02}$ | $0.346_{\pm 0.001}$ | $0.365_{\pm 0.001}$ |
| | $0.30_{\pm 0.02}$[66] | | | | |
| | $0.35_{\pm 0.02}$[59] | | | | |
| $\beta_2$ | $0.32_{\pm 0.03}$[29] | $0.25_{\pm 0.01}$ | $0.30_{\pm 0.02}$ | $0.346_{\pm 0.001}$ | $0.365_{\pm 0.001}$ |
| | $0.30_{\pm 0.02}$[66] | | | | |
| | $0.35_{\pm 0.02}$[59] | | | | |
| $\beta_M$ | $0.28_{\pm 0.03}$[67] | $0.25_{\pm 0.01}$ | $0.30_{\pm 0.02}$ | $0.346_{\pm 0.001}$ | $0.365_{\pm 0.001}$ |
| | $0.25_{\pm 0.02}$[59] | | | | |
| $\beta_F$ | $0.243_{\pm 0.005}$[67] | $0.25_{\pm 0.01}$ | $0.30_{\pm 0.02}$ | $0.346_{\pm 0.001}$ | $0.365_{\pm 0.001}$ |

Table 11.1: Comparison of experimental critical exponents $\beta$ for $CsNiCl_3$ (NMR measurement[29], neutron measurement[66],[67], and ultrasonic velocity measurement[59]) and the predicted values of $\beta$ for various universality classes[18], where $\beta_1$, $\beta_2$, $\beta_M$, and $\beta_F$ represent the critical exponents at $T_{N1}$, $T_{N2}$, the multicritical point ($T_m$, $H_m$), and between the paramagnetic phase and 120° phase, respectively.

As mentioned in Chapter 9, according to the non-mean-field theory, the temperature dependence of the spin order parameter can be expressed as

$$S = S_0(1 - \frac{T}{T_N})^{\beta}, \tag{11.1}$$

where $T_N$ is the critical temperature, and $\beta$ is the critical exponent associated with a phase transition. Together with the relations between the elastic constants and the order parameters obtained in Chapter 10, the value of critical exponent $\beta$ can be determined.

In Section 11.1, the critical behavior observed on $\frac{\Delta C_{66}}{C_{66}}$ is analyzed near different phase transitions. The results are compared with theoretical predictions. Based on these results, the nature of the high-field phase transition is discussed. A series of experimental results for $\frac{\Delta C_{44}}{C_{44}}$ are also presented in order to confirm our findings.

## 11.1 Field dependence of the critical exponent $\beta$

As shown in Chapter 10, the value of the critical exponent $\beta$ can be extracted by fitting the temperature dependence of the elastic constants measured in this work. In this section the behavior of $\frac{\Delta C_{66}}{C_{66}}$ near the high-field phase boundary is studied at different fields. From the paramagnetic phase to the 120° phase, with the decreasing of the temperature, the relative variation of $C_{66}$ can be calculated according to Relation 10.15 and 10.20 as

$$\frac{\Delta C_{66}}{C_{66}}_{p-120} = \frac{C^*_{66(120)} - C^*_{66(p)}}{C^*_{66(p)}} = V_{66S_\perp} S_\perp^2. \tag{11.2}$$

Eq. 11.2 shows that the relative variation of the elastic constant at constant field is proportional to the square of the order parameter. Hence, the temperature dependence of the order parameter can be obtained from the experimental results presented

in Chapter 6. According to the definition given by Eq. 11.1, the critical exponent near the high-field phase boundary can be extracted by fitting the temperature dependence of the order parameter $S_\perp$ using a power law close to the transition temperature.

In Fig. 11.2 we present a log-log plot of $S_\perp^2$ as function of the reduced temperature $\tau = 1 - \frac{T}{T_N}$ obtained using the experimental data of $\frac{\Delta C_{66}}{C_{66}}$ presented in Fig. 6.4. We

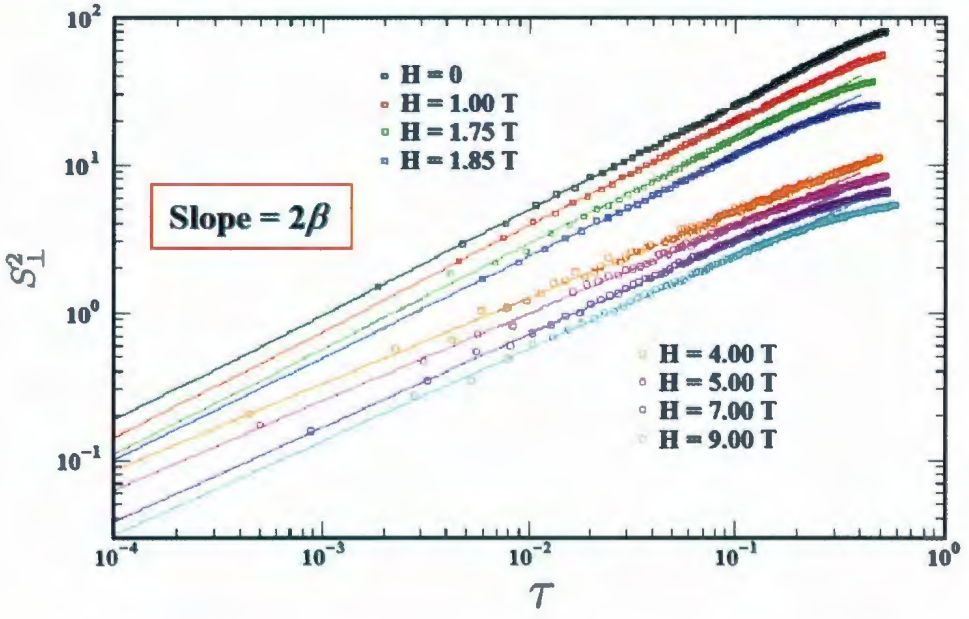


Figure 11.2: Square of the order parameter $S_\perp^2$ as a function of the reduced temperature $\tau = 1 - \frac{T}{T_N}$ on a log-log plot extrapolated from experimental data $\frac{\Delta C_{66}}{C_{66}}$ for fields applied along the c-direction.

notice that, for fields lower than $H_m = 2.29$ T (near the L-E phase boundary), the slopes are almost the same. This indicates that the value of $\beta_2$ (the value of $\beta$ near the L-E phase boundary) is constant within the uncertainties. However, at higher field (near the P-120 phase boundary), a change in the value of the slope is obvious. This is the evidence that $\beta_F$ is field dependent.

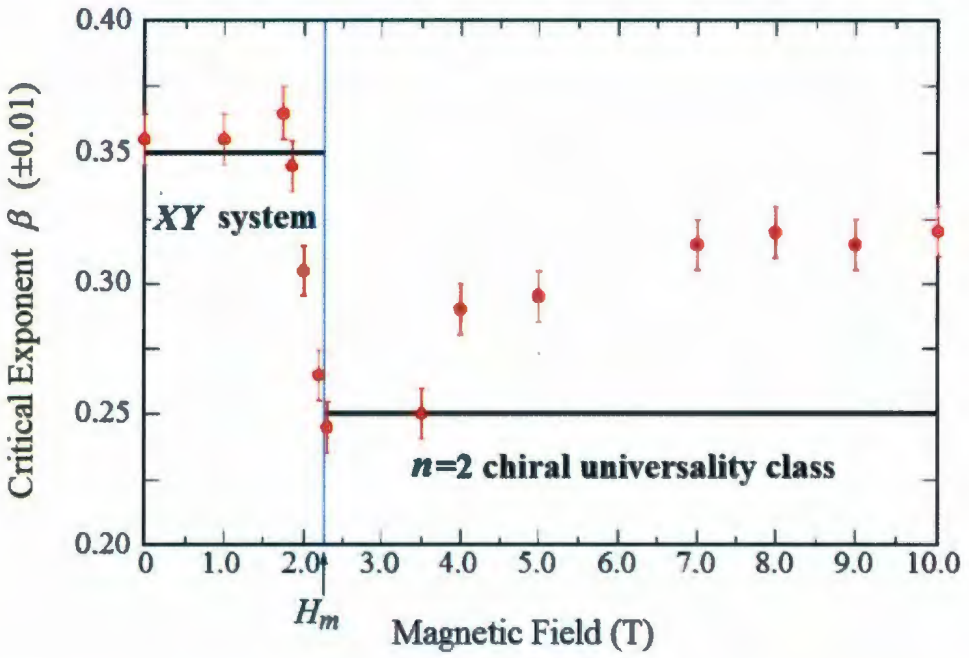


Figure 11.3: Magnetic field dependence of the critical exponents $\beta$ extrapolated from the temperature dependence of $\frac{\Delta C_{66}}{C_{66}}$ at different magnetic fields. Theoretical prediction of $\beta$ for both $XY$ type and $n = 2$ chirality models[16] are illustrated with solid lines for a comparison.

The magnetic field dependence of $\beta$ is summarized in Fig. 11.3. For $H < H_m$, we obtain $\beta = 0.35 \pm 0.02$, which is consistent with the prediction for the $XY$ class. This close agreement indicates that we can trust the data obtained using ultrasonic velocity measurements. At field close to $H_m$, $\beta$ suddenly decreases to a minimum value of $0.25 \pm 0.02$. This value agrees with Kawamura's prediction[16] for the $n = 2$ chiral universality class associated with the $120^\circ$ spin configuration. However, at high fields, the value of $\beta$ increases and deviates significantly from Kawamura's prediction. As discussed above, the inconsistency between Kawamura's prediction and our data

at high fields cannot be attributed to the experimental approach. The fact that the value of $\beta$ is field dependent indicates that the phase transition associated with the 120° spin configuration does not belong to the new chirality class proposed by Kawamura[16]. The field dependence of the order parameter rather suggests that the transition is weakly first-order.

## 11.2 Discontinuities in the temperature dependence of $\frac{\Delta C_{44}}{C_{44}}$

To confirm the nature of the phase transition at high field, we also investigate the temperature dependence of $\frac{\Delta C_{44}}{C_{44}}$ at different fields. For $H < H_m$, as shown in Fig. 6.3, a unique scaling is observed and a critical exponent with value $\beta = 0.35 \pm 0.02$ can be extracted. This validates the second-order nature of the phase transition between the linear and elliptical phases. However, at high fields where $H > H_m$, no well defined power law near the phase boundary is observed. Again this contradicts Kawamura's prediction for the 120° phase. Moreover, in Fig. 6.3 we observe step-like anomalies which are not predicted by Eq. 10.20g. These discontinuities in the temperature dependence of $\frac{\Delta C_{44}}{C_{44}}$ provide further evidences for a weakly first-order phase transition.

## 11.3 Thermal hysteresis

Another feature associated with discontinuous phase transition is the observation of thermal hysteresis phenomena. By performing a cooling-heating thermal cycle, we explore the possibility of thermal hysteresis. As shown in Fig. 11.4, at $T =$ 5.00 K, which is higher than $T_m$, obvious differences between the heating and cooling curves are observed. In other words, the phase transition is discontinuous on the

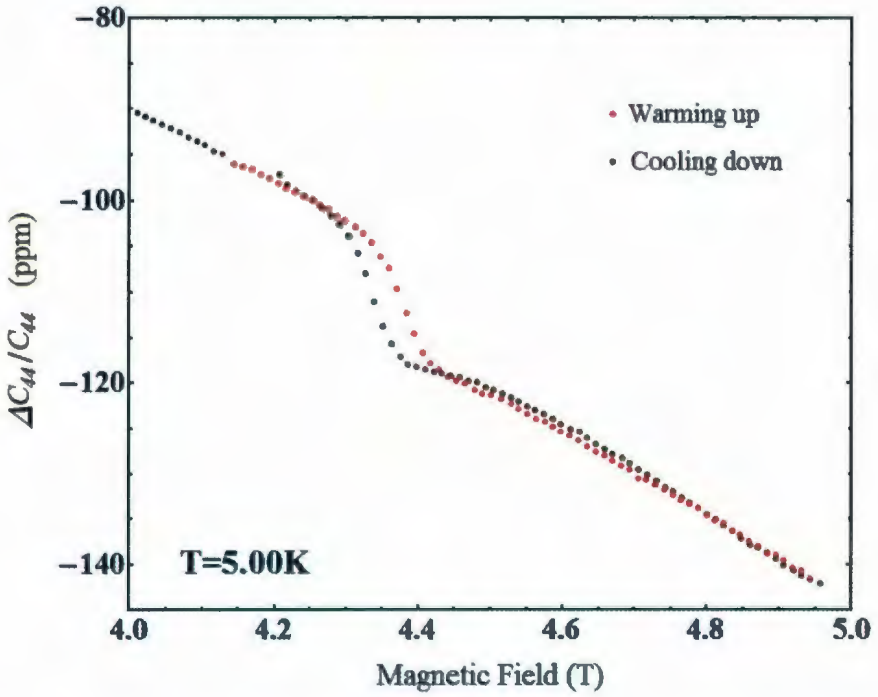


Figure 11.4: The behaviors of $\frac{\Delta C_{44}}{C_{44}}$ as function of magnetic field at $T = 5.00$ K in both warming up and cooling down processes are compared to show the possibility of thermal hysteresis.

phase boundary between the paramagnetic and 120° spin structure phase. This again confirms our conclusion that the phase transition at higher magnetic fields is weakly first-order.

In summary, based on the low fields data from $\frac{\Delta C_{44}}{C_{44}}$ and $\frac{\Delta C_{66}}{C_{66}}$, the value of the critical exponent is $\beta = 0.35 \pm 0.02$. This is consistent with the prediction for a $XY$ system and confirm that the phase transition is second-order. For the phase transition between the paramagnetic and the 120° phase above $H = 2.00$ T in $CsNiCl_3$, we observe step-like anomalies, thermal hysteresis, and no well defined single critical exponent. All these results show the evidence of a weakly first-order phase transition between the paramagnetic and the 120° phases. This agrees with the recent discussion presented by Thanh Ngo and Diep[26] that phase transition associated with frustrated spin systems should be first-order.

# Chapter 12

# Numerical predictions of the elastic constants

The goal here is to present sufficient experimental data to test the model described in Chapter 8 and Chapter 9. In this work, the experimental results obtained by ultrasonic measurements for a magnetic field applied along the c-direction are analyzed. As shown in Section 8.2, many of the model coefficients can be determined from the magnetic phase diagram (see Table 8.2 and Table 8.3). The remaining coefficients can be adjusted using the temperature and field dependence of a few elastic constants. In this chapter, some of the experimental results presented in Section 6.2 are compared to the predictions based on the model derived in Section 10.3. In order to reproduce the experimental results, a non-mean-field temperature dependence has been used for the order parameters. The values of the critical exponent $\beta$ used in this chapter correspond to those determined in Section 11.1. In particular, the relative variation of elastic constants $\frac{\Delta C_{33}}{C_{33}}$ and $\frac{\Delta C_{66}}{C_{66}}$, as function of temperature or magnetic field, are presented separately in Section 12.1 and Section 12.2.

## 12.1 Temperature and magnetic field dependence of $\frac{\Delta C_{33}}{C_{33}}$

For clarity, we list the theoretical results for $C^*_{33}$ in the different ordered phases:

$$C^*_{33(p)} = C_{33} + 2V_{3,3,3,3,0}m_z^2 - \frac{4K^2_{3,3,0}m_z^3}{2B_3m_z^3 + H}, \tag{12.1a}$$

$$C^*_{33(l)} = C_{33} - \frac{4K^2_{3,3,Q}}{B} + 4V_{3,3,3,3,Q}S^2 + 2V_{3,3,3,3,0}m_z^2 + \frac{4(K_{3,3,0} - 2B_6K_{3,3,Q})^2m_z^3}{2(2BB_6^2 - B_3)m_z^3 - H}, \tag{12.1b}$$

$$\begin{aligned} C^*_{33(e)} = C_{33} &- \frac{(K_{3,1,Q} + B_7K_{3,3,Q})^2}{B_8} + 4V_{3,3,3,3,Q}S^2 + 4(V_{3,3,1,Q} - V_{3,3,3,Q})S_\perp^2 \\ &+ 2V_{3,3,3,3,0}m_z^2 + \frac{(B_9K_{3,1,Q} + 2K_{3,3,0} + B_{10}K_{3,3,Q})^2m_z^3}{(B_{11} - 2B_3)m_z^3 - H}, \end{aligned} \tag{12.1c}$$

$$C^*_{33(120)} = C_{33} - \frac{4K^2_{3,1,Q}}{B - B_2} + 8V_{3,3,1,Q}S_\perp^2 + 2V_{3,3,3,3,0}m_z^2 - \frac{4(2B_{12}K_{3,1,Q} + K_{3,3,0})^2m_z^3}{2(2B_5B_{12} + B_3)m_z^3 + H}. \tag{12.1d}$$

According to these results, 6 coefficients remain to be fixed. We notice that $K_{3,3,0}$ and $V_{3,3,3,3,0}$ are coupling coefficients associated with magnetization and need to be solved by analyzing the field dependence of $\frac{\Delta C_{33}}{C_{33}}$ at different temperatures in the paramagnetic phase. The other coefficients can be adjusted using data obtained at zero field. For the case of $H = 0$, according to Eq. 12.1a and 12.1b, the change of $\frac{\Delta C_{33}}{C_{33}}$ from the paramagnetic state to linear phase is $-\frac{4K^2_{3,3,Q}}{B\,C_{33}} + \frac{4V_{3,3,3,3,Q}S^2}{C_{33}}$. Here $K_{3,3,Q}$ determines the sudden decrease in $C_{33}$ at $T_{N1}$ (see Fig. 12.1). Also seen in Fig. 12.1 is that the experimental data barely depends on $S^2$ in the linear phase; therefore $V_{3,3,3,Q}$ is set to 0. The coefficients $K_{3,1,Q}$ and $V_{3,3,1,Q}$ can be adjusted using the data obtained in the elliptical phase. The remaining coefficients necessary for our analysis of $C_{33}$ are given in Table 12.1.

We notice that, in the elliptical phase, the temperature dependence of $\frac{\Delta C_{33}}{C_{33}}$ is mostly accounted for by $V_{3,3,1,Q}$, which comes from the q-q magnetoelastic coupling term. This indicates that q-q coupling terms are necessary in describing the behavior of elastic constants at lower temperatures. The theoretical predictions based on the free energy with and without the q-q coupling terms are both plotted in Fig. 12.1.

| | |
|---|---|
| $K_{3,1,Q}$ | $-1.1952 \times 10^5$ |
| $K_{3,3,Q}$ | $4.1306 \times 10^4$ |
| $K_{3,3,0}$ | $4.7297 \times 10^4$ |
| $V_{3,3,1,Q}$ | $8.1810 \times 10^6$ |
| $V_{3,3,3,Q}$ | 0 |
| $V_{3,3,3,0}$ | $-3.1621 \times 10^6$ |

Table 12.1: Coefficients extrapolated from experimental data for $\frac{\Delta C_{33}}{C_{33}}$ of $CsNiCl_3$.

Furthermore, we also present the prediction obtained using a non-mean-field temperature dependence for the order parameter. As shown by the solid lines in Fig. 12.1, a mean-field critical exponent $\beta = 0.5$ leads to a linearly temperature dependence below $T_{N2}$. This fails to reproduce the behavior of $\frac{\Delta C_{33}}{C_{33}}$ in the elliptical phase. However, with a non-mean-field critical exponent $\beta \approx 0.35$, the theoretical prediction for $\frac{\Delta C_{33}}{C_{33}}$ reproduces the experimental data successfully in the small temperature range close to $T_{N2}$.

Using the analytical solution of the magnetization, the temperature dependence of $\frac{\Delta C_{33}}{C_{33}}$, measured at different magnetic fields, can also be reproduced. The comparison between the experimental data and the numerical predictions are shown in Fig. 12.2 (for $H < H_m$) and Fig. 12.3 (for $H > H_m$). For the higher fields, as shown by Fig. 12.3, the numerical predicted variation on the phase boundary is approximately twice that of the experimental data. However, in general, by employing a non-mean-field temperature dependence for the order parameters, the agreement between the numerical predictions with the experimental data is improved, except for $H = 2.00$ T. According to the phase diagram, the temperature scan at $H = 2.00$ T is likely accom-

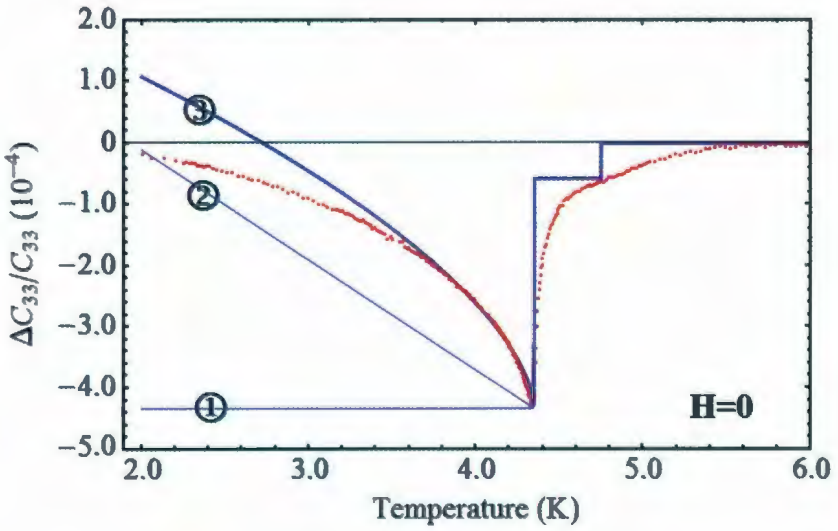


Figure 12.1: Temperature dependence of $\frac{\Delta C_{33}}{C_{33}}$ of $CsNiCl_3$ at $H = 0$. The numbered blue solid lines are the model predictions corresponding to: ① without q-q magnetoelastic coupling, ② with q-q magnetoelastic coupling and mean-field critical exponent $\beta = 0.5$, ③ with q-q magnetoelastic coupling and non-mean-field critical exponent $\beta = 0.35$.

panied by first-order contribution, not taken into account in the present model. This explains the significant disagreement between the data and the theoretical prediction for field ranging from 1 T to 3 T.

In Fig. 12.4, we present the numerical predictions for the magnetic field dependence of $\frac{\Delta C_{33}}{C_{33}}$ at $T = 5.60$ K. Our theoretical results successfully predict the step-like anomaly on the phase boundary and the behavior of $\frac{\Delta C_{33}}{C_{33}}$ at lower fields. However, our model fails to reproduce the amplitude of the steps. Given that the phase boundary has been proved to be of weakly first-order, it's difficult to predict the behavior of the elastic constants right on this boundary.

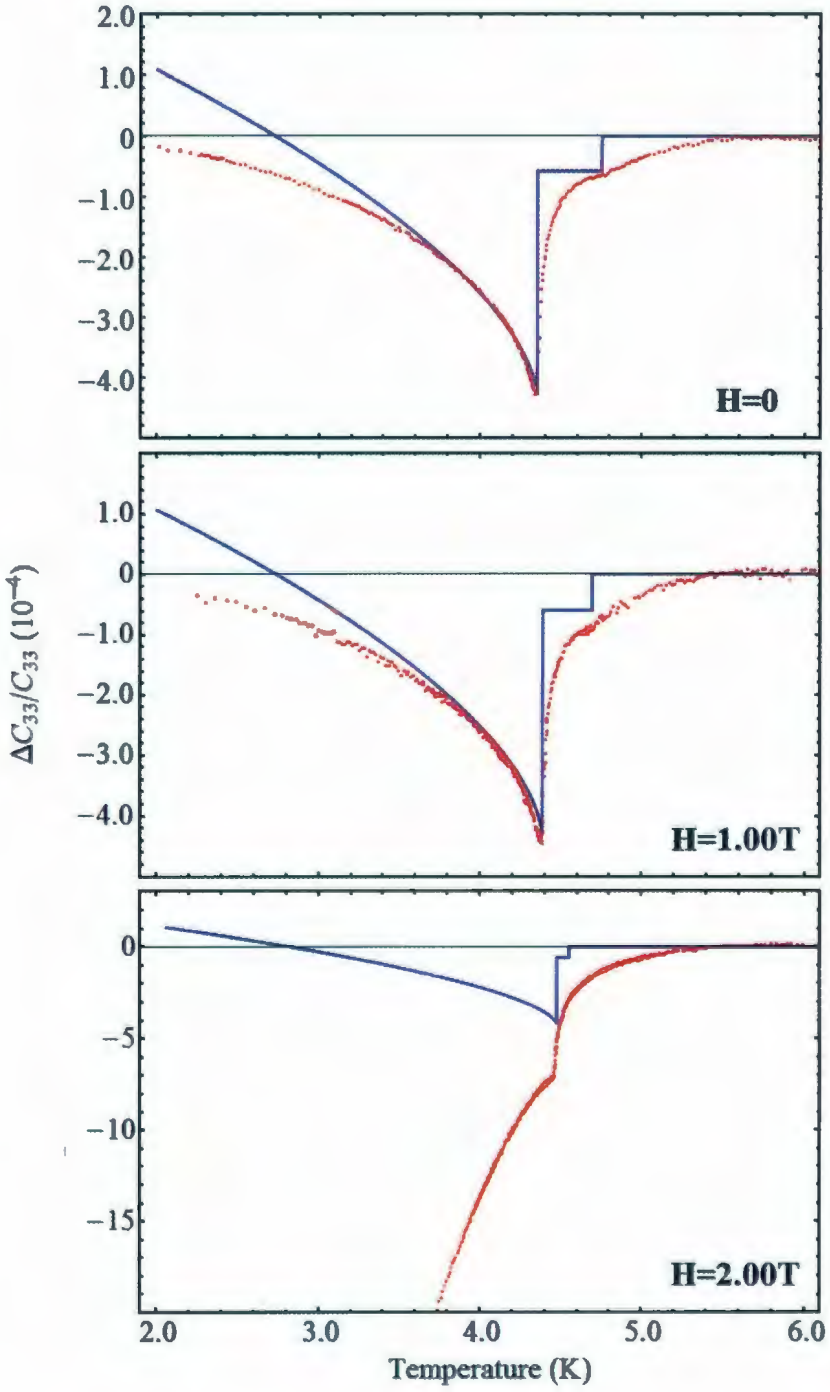


Figure 12.2: Temperature dependence of $\frac{\Delta C_{33}}{C_{33}}$ of $CsNiCl_3$ at $H < H_m$ for the case of H//c. The blue solid line and the red points are the model prediction and experimental data, respectively.

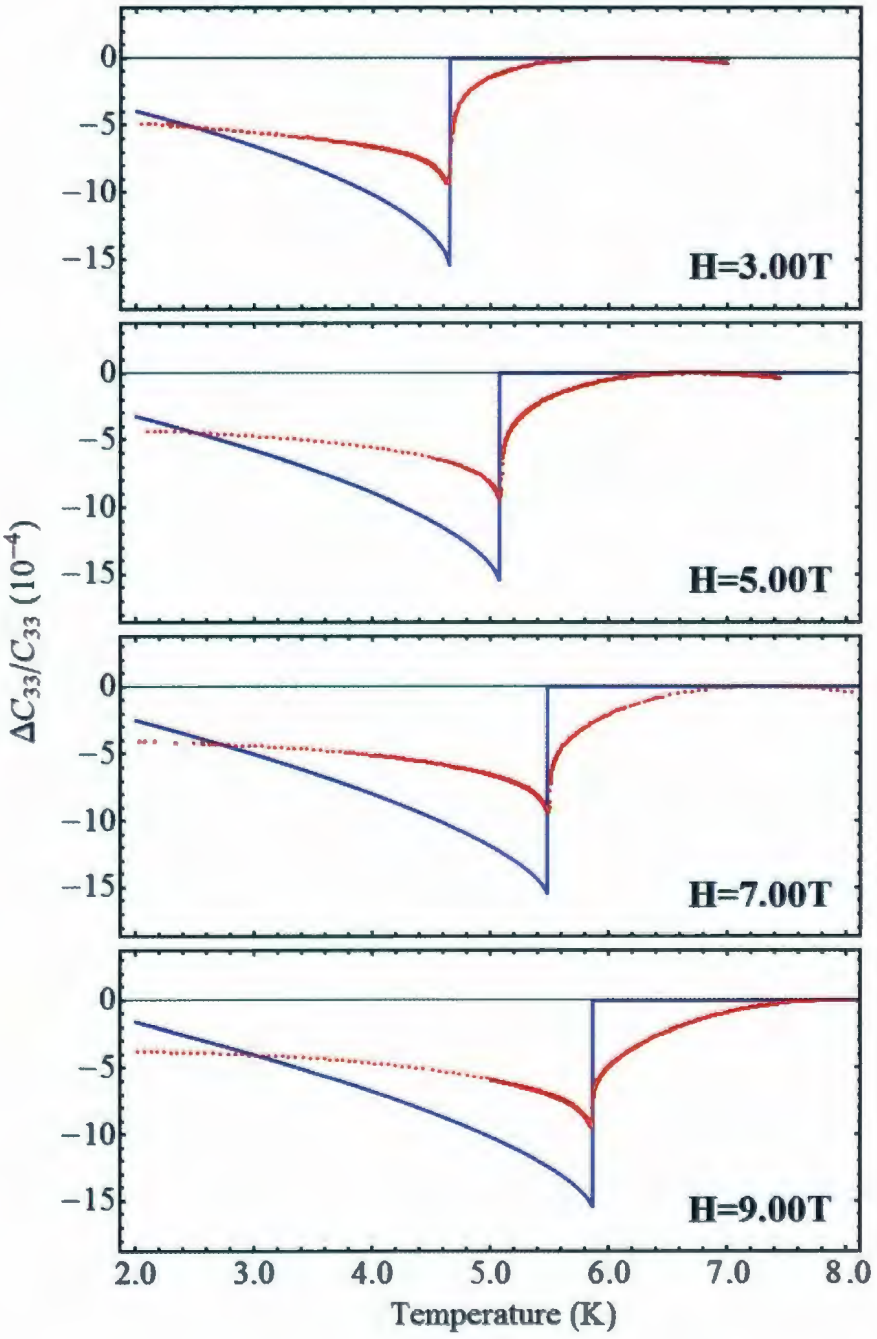


Figure 12.3: Temperature dependence of $\frac{\Delta C_{33}}{C_{33}}$ of $CsNiCl_3$ at $H > H_m$ for the case of H//c. The blue solid line and the red points are the model prediction and experimental data, respectively.

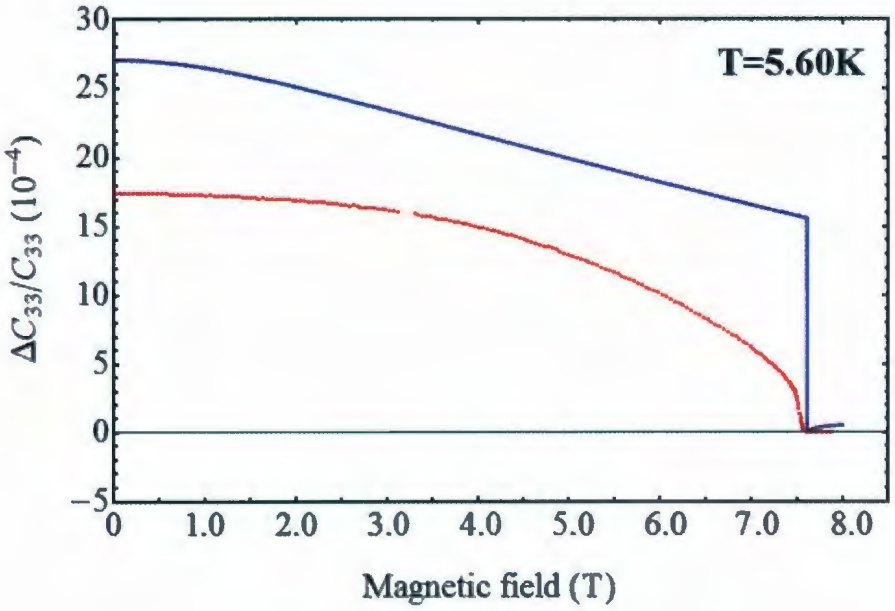


Figure 12.4: Magnetic field dependence of $\frac{\Delta C_{33}}{C_{33}}$ of $CsNiCl_3$ at $T = 5.60$ K for the case of H//c. The blue solid line and the red points are the model prediction and experimental data, respectively.

## 12.2 Temperature and magnetic field dependence of $\frac{\Delta C_{66}}{C_{66}}$

The behavior of the relative variation of elastic constant $C_{66}$ is presented in this section. Based on the calculation in Section 10.3, we have:

$$C^*_{66(p)} = C_{66} + V_{1,3,0} m_z^2, \tag{12.2a}$$

$$C^*_{66(l)} = C_{66} + V_{1,3,Q} S^2 + V_{1,3,0} m_z^2, \tag{12.2b}$$

$$C^*_{66(e)} = C_{66} + V_{1,3,Q} S^2 + V_{1,6,Q} S_\perp^2 + V_{1,3,0} m_z^2, \tag{12.2c}$$

$$C^*_{66(120)} = C_{66} + V_{2,6,Q} S_\perp^2 + V_{1,3,0} m_z^2. \tag{12.2d}$$

We notice that the field and temperature dependence of $C_{66}$ are exclusively associated with q-q magnetoelastic coupling terms. This again shows the necessity to consider the q-q terms in the model. Here $V_{1,3,0}$ determines the field dependence while the others are associated with the order parameters. According to Fig. 6.1, at $H = 0$, we barely observed any change on $\frac{\Delta C_{66}}{C_{66}}$ at $T_{N1}$, therefore, $V_{1,3,Q}$ can be set to 0. Moreover, based on the experimental data presented in Fig. 6.4, we notice that the temperature dependence of $\frac{\Delta C_{66}}{C_{66}}$ in the 120° phase (for $H > H_m$) has the opposite tendency as that observed in the elliptical phase (for $H < H_m$). Hence, $V_{1,6,Q}$ and $V_{2,6,Q}$ must have opposite signs. The coefficients used for our numerical predictions are listed in Table 12.2.

| | |
|---|---|
| $V_{1,3,0}$ | $-1.9334 \times 10^7$ |
| $V_{1,3,Q}$ | 0 |
| $V_{1,6,Q}$ | $-8.7075 \times 10^8$ |
| $V_{2,6,Q}$ | $2.2690 \times 10^8$ |

Table 12.2: Coefficients extrapolated from experimental data for $\frac{\Delta C_{66}}{C_{66}}$ of $CsNiCl_3$.

The numerical predictions for the temperature dependence are presented in Fig. 12.5 (for $H < H_m$) and Fig. 12.6 (for $H > H_m$). Experimental results are also presented for comparison. At lower magnetic fields, numerical results agree well with the experimental data, except for $H = 2.00$ T due to the first-order phase transition. At higher magnetic fields, the theoretical and experimental results overlap with each other well close to the critical temperature. Thus, the change of $\frac{\Delta C_{66}}{C_{66}}$ with temperature, for fields of $H > H_m$ and $H < H_m$, are reproduced successfully.

The magnetic field dependence of $\frac{\Delta C_{66}}{C_{66}}$ at different temperatures are shown in Fig. 12.7. For $T < T_m$, for example, at $T = 2.50$ K, the behavior of $\frac{\Delta C_{66}}{C_{66}}$ in the elliptical phase is well reproduced, however, due to the first-order phase transition, we failed to predict the magnitude of the sudden decrease on the phase boundary. For $T > T_m$, for example, at $T = 5.60$ K, it's hard to reproduce the critical behavior of $\frac{\Delta C_{66}}{C_{66}}$ close to the phase boundary. However, the magnitude of the decrease from zero field is predictable. This might due to the weakly first-order nature of the high field phase boundary.

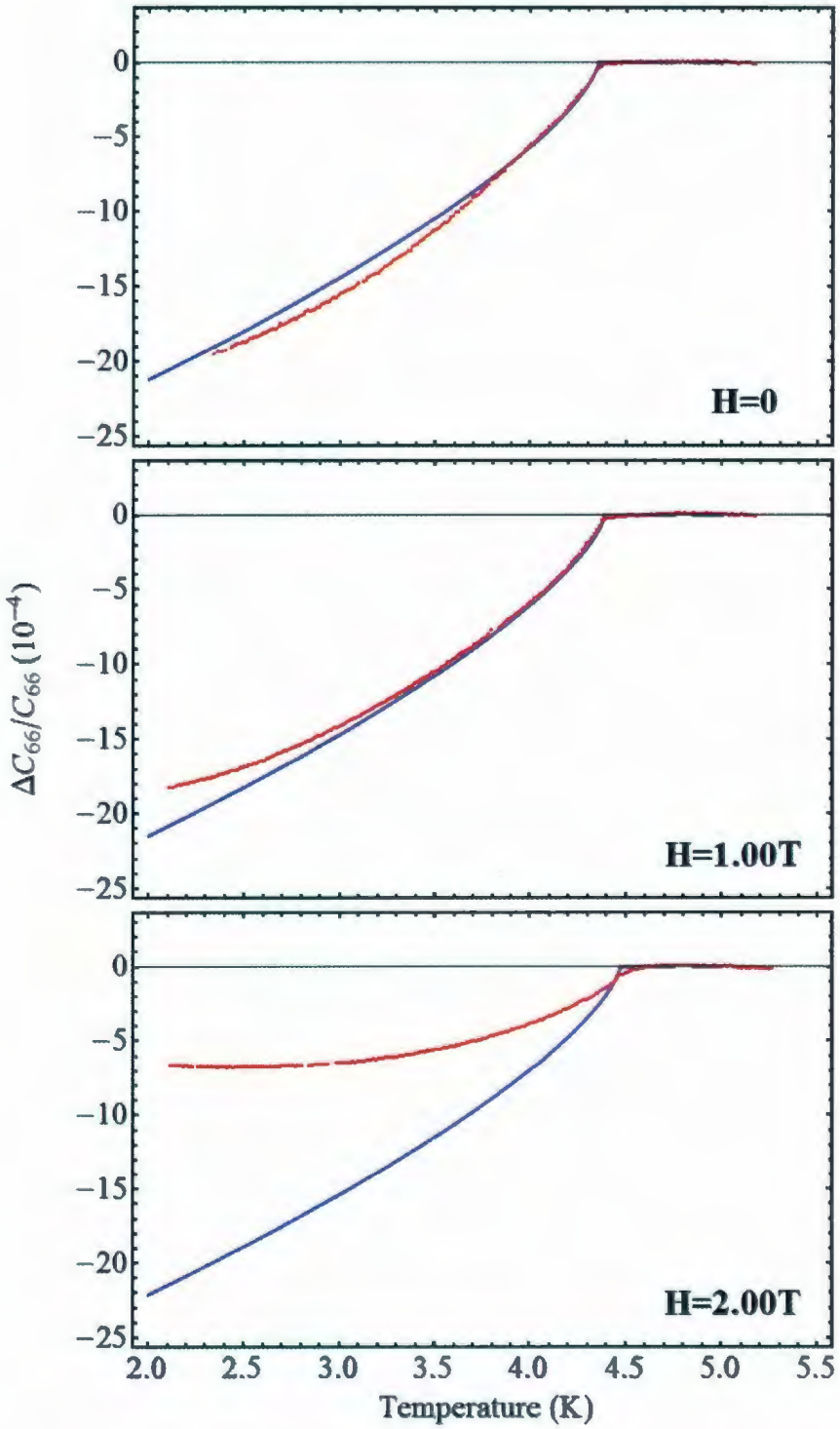


Figure 12.5: Temperature dependence of $\frac{\Delta C_{66}}{C_{66}}$ of $CsNiCl_3$ at $H < H_m$ for the case of H//c. The blue solid line and the red points are the model prediction and experimental data, respectively.

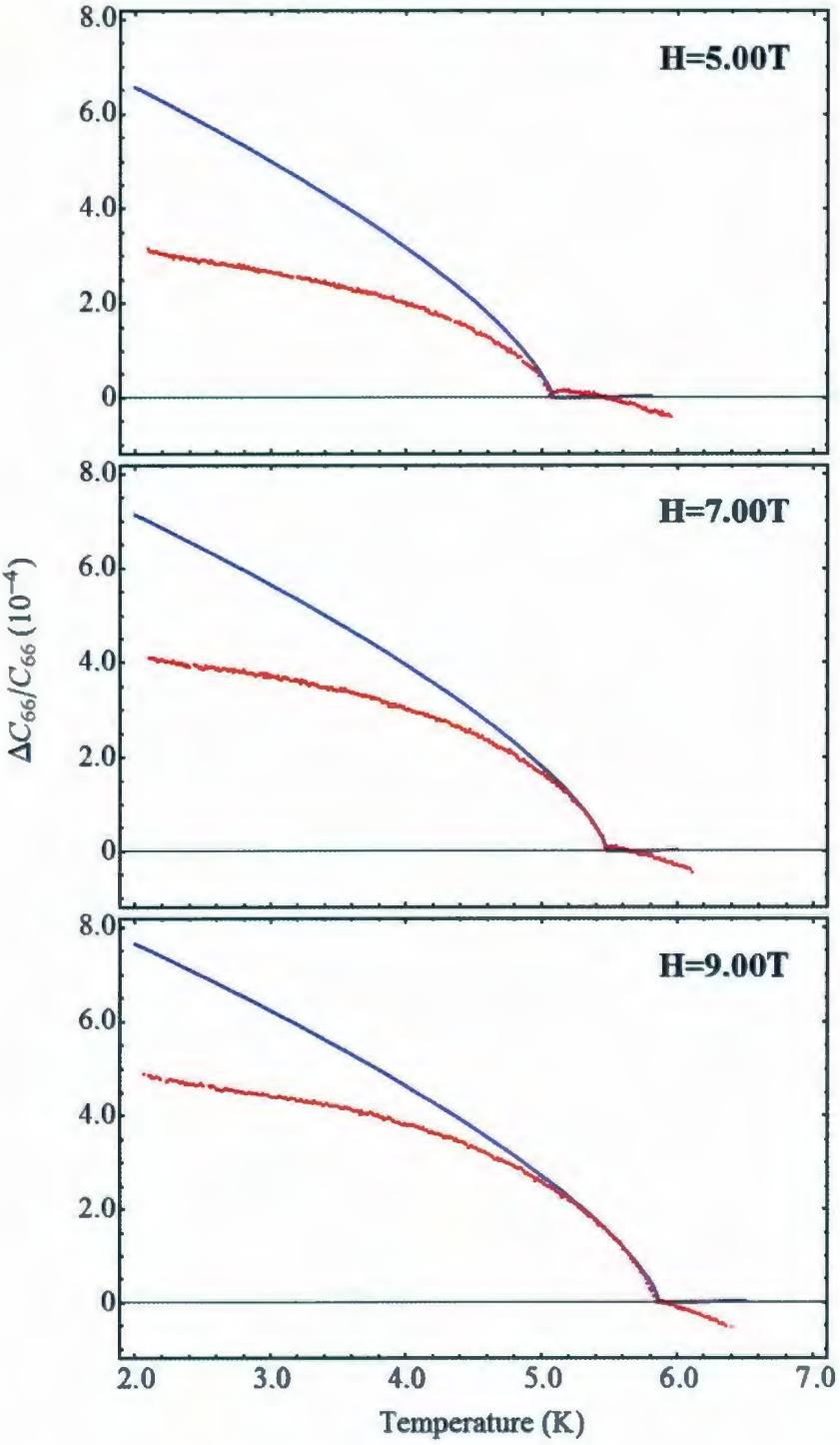


Figure 12.6: Temperature dependence of $\frac{\Delta C_{66}}{C_{66}}$ of $CsNiCl_3$ at $H > H_m$ for the case of H//c. The blue solid line and the red points are the model prediction and experimental data, respectively.

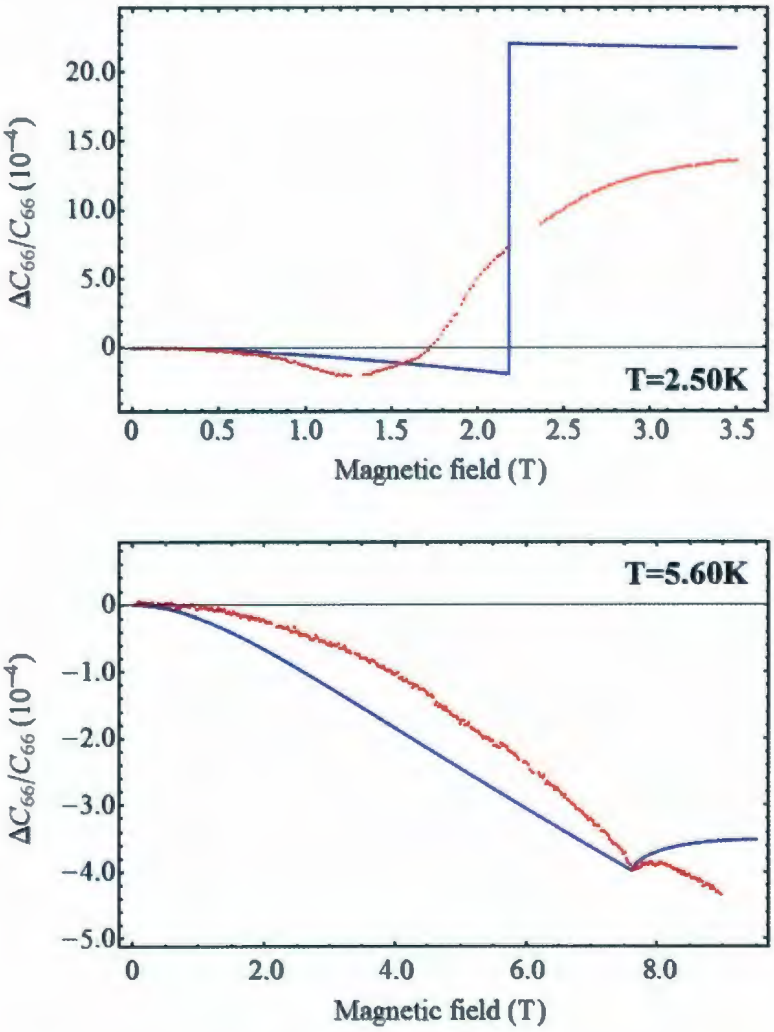


Figure 12.7: Magnetic field dependence of $\frac{\Delta C_{66}}{C_{66}}$ of $CsNiCl_3$ at different temperatures for the case of H//c. The blue solid line and the red points are the model prediction and experimental data, respectively.

# Chapter 13

# Conclusions

Due to its interesting magnetic properties, the frustrated easy-axis antiferromagnet $CsNiCl_3$ has been studied in our work. As a quasi-one-dimensional hexagonal compound, $CsNiCl_3$ has a geometrically frustrated spin configuration on the triangular lattice. This leads to the novel magnetic properties in the field induced $120^{\circ}$ spin structure. Our ultrasonic measurements reveal the features of the phase transition associated with this special phase. Moreover, to explain the critical behavior near the phase transitions, a Landau model for $CsNiCl_3$ is tested using experimental data.

For our investigation, high-resolution ultrasonic velocity measurements have been used to examine the temperature and magnetic field dependence of the elastic constants of $CsNiCl_3$. A low-temperature and high magnetic field system has been used in order to obtain the variation of longitudinal ($C_{33}$) and transverse ($C_{44}$ and $C_{66}$) elastic constants for a magnetic field applied along the c-direction of the crystal. As presented in Chapter 6, at $H = 0$ (see Fig. 6.1) the temperature dependence of $C_{33}$, $C_{44}$, and $C_{66}$ all show a clear anomaly at $T \approx 4.35$ K indicating the onset of the linear to elliptical phase transition. At $T \approx 4.75$ K, the phase transition between the paramagnetic and the linear phase can be easily observed on $C_{33}$ and $C_{44}$, how-

ever, the anomaly on $C_{66}$ is barely noticeable. Similar anomalies are also observed on the temperature dependence of these elastic constants at different magnetic fields (see Fig. 6.2 - Fig. 6.4). Meanwhile, anomalies observed at fields larger than the tetracritical field ($H_m \approx 2.29$ T) are associated with the phase transition between the paramagnetic phase and the 120° spin configuration phase. The phase boundaries are clearly illustrated by the shifting of the critical temperature with the increasing of the magnetic field. Furthermore, our data for the magnetic field dependence of $C_{33}$, $C_{44}$, and $C_{66}$ (see Fig. 6.5 - Fig. 6.7) present evidence of critical behavior. The observed critical temperatures and magnetic fields are summarized in the experimental phase diagram shown in Fig. 6.8, which is in good agreement with the phase diagram presented in previous publications[16].

A detailed study of the critical behavior of $CsNiCl_3$ has also been realized especially for the 120° phase. Data of the temperature dependence of $\frac{\Delta C_{66}}{C_{66}}$ has been used to obtain the value of the critical exponent $\beta$, as shown in Fig. 11.2. Our results show that the critical exponent $\beta$ is constant for $H < H_m$, however, it is field dependent above $H_m$. As presented in Fig. 11.3, near the phase boundary between the linear and the elliptical phase $\beta = 0.35 \pm 0.02$, which is consistent with the prediction for a $XY$ class[4]. Near the multicritical point, $\beta$ suddenly decreases to $0.25 \pm 0.02$. However, with increasing field, the value of $\beta$ increases significantly. The field dependence of $\beta$ indicates that the phase transition associated with the 120° phase doesn't belong to the new chirality class proposed by Kawamura[16]. To verify our conclusion, we also investigated the behavior of $\frac{\Delta C_{44}}{C_{44}}$ near the high field phase boundary. Step-like anomalies are clearly observed and no well defined power law can be determined. This confirms that the phase transition at higher field is discontinuous. Furthermore, by performing a cooling-heating thermal cycle, we observed thermal hysteresis (see Fig. 11.4), confirming that the phase transition between the paramagnetic and the

120° phase is weakly first-order. Our data supports the results obtained by Delamotte et al.[23] and Ngo et al.[26] and solve the controversy about the true nature of the phase transition at high field.

The elastic constants of $CsNiCl_3$ have also been analyzed using a Landau model, which has been successfully used to describe the magnetic properties of $ABX_3$ systems. Based on the Landau free-energy derived by Plumer et al.[11], invariant terms, under the main symmetry operations for hexagonal compounds ($C_{6z}$, $C_{2y}$, and $I$) have been identified. The Landau free-energy for a magnetic field applied along the c-direction are presented in Eq. 8.17. Based on this Landau free-energy, the phase diagram is obtained using the temperature dependence of the magnetization. As shown in Fig. 8.1, this Landau model reproduces successfully all four phases and agrees with our experimental phase diagram. The Landau free-energy is also modified to account for the relations among strains, order parameters, and elastic constants of $CsNiCl_3$. For the magnetoelastic couplings, only linear-quadratic (l-q) and quadratic-quadratic (q-q) couplings have been considered. The elastic constants and strains are calculated using the total free energy according to Eq. 10.1 and Eq. 10.4 with $\phi = 0$. As shown by Eq. 10.8, we notice that in the elliptical phase, $e_1 \neq e_2$. This indicates that in the elliptical phase the spin structure reduces the symmetry from hexagonal to orthorhombic. This reduction in the symmetry can also be observed from the calculated elastic constants. In the elliptical phase, the number of independent elastic constants increases to 9, which corresponds to an orthorhombic structure.

The temperature and magnetic field dependence of the elastic constants $C_{33}$ and $C_{66}$, obtained using the calculated results based on the Landau model, are compared to the experimental results. As shown in Fig. 12.1, a non-mean-field order parameter and q-q magnetoelastic couplings are necessary in order to obtain a good agreement. Even so, the critical behavior can only be reproduced in a small temperature range

close to the phase boundary. For $\frac{\Delta C_{33}}{C_{33}}$, as shown in Fig. 12.2, for $H < H_m$ the variations at $T_{N1}$ and $T_{N2}$ are well reproduced. However, with increasing field, it becomes harder to reproduce the magnitude of the variation in the linear phase. This is due to the the first-order boundary close to $H = 2.00$ T, which is not considered in our Landau model. For $H > H_m$, as presented in Fig. 12.3 the critical behavior of $\frac{\Delta C_{33}}{C_{33}}$ close to the phase boundary is well reproduced using a field dependent critical exponent $\beta$. This is also observed on the temperature dependence of $\frac{\Delta C_{66}}{C_{66}}$ as shown in Fig. 12.5 and Fig. 12.6.

The agreement between our experimental data and the model prediction shown in this work is a powerful confirmation that high-resolution ultrasonic velocity measurements are effective tools for studying the nature of $CsNiCl_3$. Therefore, further investigation of the low-temperature behaviors with respect to other frustrated quasi-one-dimensional antiferromagnets are desirable.

# Appendix A

# Temperature dependence of $\frac{\Delta C_{11}}{C_{11}}$ at $H = 0$

Based on the calculation in Section 10.3, the temperature dependence of $C_{11}$ of $CsNiCl_3$ in different phases at $H = 0$ corresponds to

$$C^*_{11(p)} = C_{11}, \tag{A.1a}$$

$$C^*_{11(l)} = C_{11} - \frac{4K^2_{1,3,Q}}{B} + 4V_{1,1,3,Q}S^2, \tag{A.1b}$$

$$C^*_{11(e)} = C_{11} - \frac{(K_{1,2,Q} + B_7 K_{1,3,Q})^2}{B_8} + 4V_{1,1,3,Q}S^2 + 4(V_{1,1,2,Q} - V_{1,1,3,Q})S^2_{\perp}. \tag{A.1c}$$

According to the experimental data presented in Fig. A.1, no obvious variation is observed at $T_{N1}$, hence, $K_{1,3,Q}$ can be set to 0. Meanwhile, $K_{1,2,Q}$ and $V_{1,1,3,Q}$ can be determined using the behavior of $\frac{\Delta C_{11}}{C_{11}}$ in the elliptical phase. The fixed coefficients are listed in Table A.1, where $K_{1,1,Q}$ is extrapolated from the experimental data of the thermal expansion coefficient along the c-axis[55]. The numerical prediction of the temperature dependence of $\frac{\Delta C_{11}}{C_{11}}$ at $H = 0$ are presented in Fig. A.1 together with the experimental results. By using a non-mean-field order parameter, our model agrees with the experimental result well.

| | |
|---|---|
| $K_{1,1,Q}$ | $-4.8246 \times 10^5$ |
| $K_{1,2,Q}$ | $1.2895 \times 10^5$ |
| $K_{1,3,Q}$ | 0 |
| $V_{1,1,2,Q}$ | $4.6838 \times 10^7$ |
| $V_{1,1,3,Q}$ | $-5.1783 \times 10^6$ |

Table A.1: Coefficients extrapolated from experimental data for $\frac{\Delta C_{11}}{C_{11}}$ of $CsNiCl_3$.

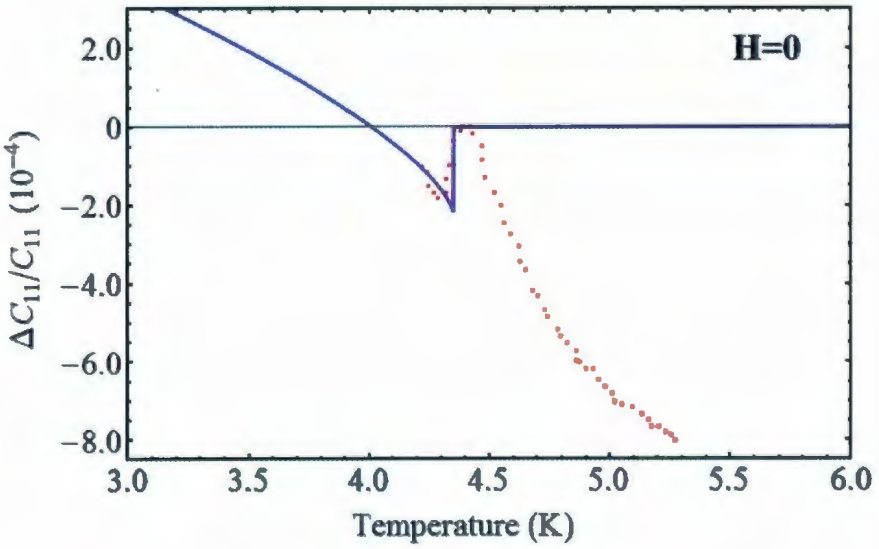


Figure A.1: Temperature dependence of $\frac{\Delta C_{11}}{C_{11}}$ of $CsNiCl_3$ at $H = 0$ for the case of H//c. The blue solid line and the red points are the model prediction and experimental data, respectively.

# Bibliography


[1] M. F. Collins and O. A. Petrenko, Triangular Antiferromagnets, review article, Can J. Phys. **75**, 605 (1997).

[2] N. Achiwa, J. Phys. Soc. Jpn. **27**, 561 (1969).

[3] M. Eibshüta, R. C. Sherwood, F. C. L. Hsu and D. E. Cox in Magnetism and Magnetic Materials (Denver.1972) Proc. 18th Annual Conf. on Magnetism and Magnetic Materials, AIP Conf. Proc. No. 10, eds. C. D. Graham Jr. and J. J. Rhyne (AIP, New York,1973) p684.

[4] P. B. Johnson, J. A. Rayne, and S. A. Friedberg, J. Appl. Phys. **50**, 1853 (1979).

[5] F. Matsubara, J. Phys. Soc. Jpn. **51**, 2424 (1982).

[6] J. A. Rayne, J. G. Collins, and G. K. White, J. Appl. Phys. **55**, 2404 (1984).

[7] S. Miyashita, J. Phys. Soc. Jpn. **55**, 227 (1986).

[8] H. Kadawaki, K. Ubukoshi, and K. Hirakawa, J. Phys. Soc. Jpn. **56**, 751 (1987).

[9] X. Zhu and M. B. Walker, Phys. Rev. B **36**, 3830 (1987).

[10] R. H. Clark and W. G. Moulton, Phys. Rev. B **5**, 788 (1972).

[11] M. L. Plumer, Kevin Hood, and A. Caillé, Phys. Rev. Lett. **60**, 45 (1988).

[12] R. Moessner and A. P. Ramirez, Physics Today, **59**, issue 2, 24 (2006).

[13] H. Kawamura, J. Phys. Soc. Jpn. **54**, 3220 (1985).

[14] H. Kawamura, J. Phys. Soc. Jpn. **55**, 2095 (1986).

[15] H. Kawamura, J. Phys. Soc. Jpn. **56**, 474 (1987).

[16] H. Kawamura, A. Caillé and M. L. Plumer , Phys. Rev. B **41**, 4416 (1990).

[17] H. Kawamura, J. Phys. Soc. Jpn. **61**, 1299 (1992).

[18] J. C. Le Guillou and J. Zinn-Justin, Phys. Rev. Lett. **39**, 95 (1977).

[19] P. Azarai, B. Delamotte, and T. Jolicoeur, Phys. Rev. Lett. **64**, 3175 (1990).

[20] M. L. Plumer and A. Mailhot, J. Phys.: Condens. Matt. **9**, L165 (1997).

[21] D. Loison and K. D. Schotte, Eur. Phys. J. B **5**, 735 (1998).

[22] H. T. Diep, ed., Frustrated Spin Systems (World Scientific, 2004).

[23] B. Delamotte, D. Mouhanna, and M. Tissier, Phys. Rev. B **69**, 134413 (2004).

[24] A. Peles, B. W. Southern, B. Delamotte, D. Mouhanna, and M. Tissier, Phys. Rev. B **69**, 220408(R) (2004).

[25] K. Kanki, D. Loison, and K. D. Schotte, J. Phys. Soc. Jpn. **75**, 015001 (2006).

[26] V. Thanh Ngo and H. T. Diep, J. Appl. Phys. **103** 07C712 (2008).

[27] D. A. Tindall, M. O. Steinita, and M. L. Plumer, J. Phys. F **7**, L263 (1977).

[28] T. E. Mason, M. F. Collins, and B. D. Gaulin, J. Phys. C **20**, L945 (1987).

[29] R. H. Clark and W. G. Moulton, Phys. Rev. B **5** , 788 (1972).

[30] M. L. Plumer and A. Caillé, Phys. Rev. B **41**, 2543 (1990).

[31] A. Caillé, M. L. Plumer, M. Poirier, and B. D. Gaulin, Physica B **165-166**, 169 (1990).

[32] M. Poirier, M. Castonguay, A. Caillé, M. L. Plumer, and B. D. Gaulin, Physica B **165-166**, 171 (1990).

[33] Y. Trudeau, M. Poirier, and A. Caillé, Phys. Rev. B **48**, 12805 (1993).

[34] Y. Trudeau, M. Poirier, and A. Caillé, Phys. Rev. B **46**, 169 (1992).

[35] M. Poirier, A. Caillé, and M. L. Plumer, Phys. Rev. B **41**, 4869 (1990).

[36] J. Kocinskj, Theory of Symmetry Changes at Continuous Phase Transitions, (Poland : D. R. P., 1983).

[37] S. Blundell, Magetism in Condensed Matter, (Oxford University Press Inc., New York, 2001).

[38] É. du Trémolet de Lacheisserie, D. Gigoux, M. Schlenker, eds., Magetism: Fundamentals, (First Springer Science + Business Media, Inc., New York, 2005).

[39] C. Kittel, Introduction to Solid State Physics - 8th ed., (John Wiley & Sons, Inc., Hoboken, 2005).

[40] P. Hofman, Solid State Physics: An Introduction, (WILEY-VCH verlag GmbH & Co. KGaA, Weinheim, 2008).

[41] I. A. Zaliznyak, L. P. Regnault, and D. Petitgrand, Phys. Rev. B **50**, 15824 (1994).

[42] K. Kakurai, M. Steiner, R. Pynn, and J. K. Kjems, J. Phys.: Condens. Matter **3**, 715 (1991).

[43] W. Achiwa, J. Phys. Soc. Jpn. **27** 561 (1969).

[44] A. Sorgen, E, Cohen, and J, Makovsky, Phys. Rev. B **10**, 4643 (1974).

[45] W. B. Yelon, and D. E. Cox, Phys. Rev. B **7**, 2024 (1973).

[46] K. Kakurai, M. Steiner, J. K. Kjems, D. Petitgrand, R. Pynn, and K. Hirakawa, J. Physique Coll. **49**, C8, 1433 (1988).

[47] H. Tanaka, J. Magn. Magn. Mater. **90-91**, 251 (1990).

[48] H. Tanaka, S. Teraoka, E. Kakenhashi, K. Iio, and K, Nagata, J. Phys. Soc. Jpn. **57**, 3979 (1988).

[49] M. Chiba, Y. Ajiro, H. Kikuchi, S. Maegawa, and T. Morimoto, J. Phys. Soc. Jpn. **61**, 1758 (1992).

[50] A. Harrison, M. F. Collins, J. Abu-Dayyeh, and C. V. Stager, Phys. Rev. B **43**, 679 (1991).

[51] Y. Ajiro, T. Inami, and H. Kadowaki, J. Phys. Soc. Jpn. **59**, 4142 (1990).

[52] H. Kadowaki, T. Inami, Y. Ajiro, K. Nakajima, and Y. Endoh, J. Phys. Soc. Jpn. **60**, 1708 (1991).

[53] B. Lüthi, Physical Acoustics in the Solid State, Series: Springer Series in Solid-State Sciences, **148**, (2007).

[54] N. H. Balshaw, Practical Cryogenics: An Introduction to Laboratory Cryogenics (Oxford instruments superconductivity limited, Oxon, England, 1996).

[55] J. A. Rayne, J. G. Collins, and G. K. White, J. Appl. Phys. **52** 1977 (1981).

[56] E. Dieulesaint, D. Royer, Elastic Waves in Solids (John Wiley and Sons Ltd., Chichester, 1980).

[57] G. Quirion, T. Taylor, and M. Poirier, Phys. Rev. B **72** 094403 (2005).

[58] J. C. Tolédano, P. Tolédano, Landau Theory of Phase Transition, (World Scienrific Publishing Co. Pte. Ltd., 1987).

[59] G. Quirion, X. Han, M. L. Plumer, and M. Poirier, Phys. Rev. Lett. **97**, 077202 (2006).

[60] M. L. Plumer, A. Caillé, and K. Hood, Phys. Rev. B **39** 4489 (1989).

[61] M. L. Plumer, A. Caillé, and K. Hood, Phys. Rev. B **40** 4958 (1989).

[62] M. L. Plumer and A. Caillé, Phys. Rev. B **37** 7712 (1988).

[63] Theo. Hahn, International tables for crystallography, (U.S.A. : D. Reidel Pub. Co., 1984).

[64] W. Rehwald, Adv. Phys. B **22** 721(1973).

[65] D. E. Cox and V. J. Minkiewicz, Phys. Rev. B **4** 2209 (1971).

[66] H. Kadowaki, K. Ubukoshi, and K.Hirakawa, J. Phys. Soc. Jpn. **56** 751 (1987).

[67] M. Enderle, R. Schneider, Y. Matsuoke, and K. Kakurai, Physica B **234-236**, 554 (1997).